UNIVERSITY OF TWENTE.

Faculty of Engineering Technology

Durability of co-bonded stiffened CFRP panels subjected to post-buckling fatigue

Bart Paulus Henricus van den Akker

M.Sc. Thesis

08 August 2018

Document number: ET.18/TM-5825

Supervisors:
dr. ir. R. Loendersloot
prof. dr. ir. M.V. Donadon

Applied Mechanics
Faculty of Engineering Technology,
University of Twente
P.O. Box 217
7500 AE Enschede
The Netherlands

Dissertation presented to the Instituto Tecnológico de Aeronáutica, in partial fulfillment of the requirements for the degree of Master of Science in the Graduate Program of Mechanical and Aeronautical Engineering, Field of Aeronautical Structures.

Bart Paulus Henricus van den Akker

DURABILITY OF CO-BONDED STIFFENED CFRP PANELS SUBJECTED TO POST-BUCKLING FATIGUE

Dissertation approved in its final version by signatories below:

Prof. Dr. Mauricio Vicente Donadon
Advisor

Dr. ir. Richard Loendersloot
Co-advisor

Prof. Dr. Pedro Teixeira Lacava
Dean for Graduate Education and Research

Campo Montenegro
São José dos Campos, SP - Brazil
2018

Cataloging-in Publication Data
Documentation and Information Division

Akker, Bart Paulus Henricus van den
Durability of co-bonded stiffened CFRP panels subjected to post-buckling fatigue / Bart Paulus Henricus van den Akker.
So Jos dos Campos, 2018.
122f.

Dissertation of Master of Science – Course of Mechanical and Aeronautical Engineering. Area of Aeronautical Structures – Instituto Tecnológico de Aeronáutica, 2018. Advisor: Prof. Dr. Mauricio Vicente Donadon. Co-advisor: Dr. ir. Richard Loendersloot.

1. Fatigue. 2. Post buckling. 3. Carbon Fiber Reinforced Polymers. I. Instituto Tecnológico de Aeronáutica. II. Title.

BIBLIOGRAPHIC REFERENCE

AKKER, Bart Paulus Henricus van den. **Durability of co-bonded stiffened CFRP panels subjected to post-buckling fatigue**. 2018. 122f. Dissertation of Master of Science – Instituto Tecnológico de Aeronáutica, São José dos Campos.

CESSION OF RIGHTS

Bart Paulus Henricus van den Akker
Alameda dos Kings, 134
12246-370 – São josé dos Campos, SP

DURABILITY OF CO-BONDED STIFFENED CFRP PANELS SUBJECTED TO POST-BUCKLING FATIGUE

Bart Paulus Henricus van den Akker

Thesis Committee Composition:

Prof. Dr. Mariano Andrés Marbelo	President -	ITA
Prof. Dr. Mauricio Vicente Donadon	Advisor -	ITA
Dr. ir. Richard Loendersloot	Co-advisor -	University of Twente
Prof. Dr. André de Boer	-	University of Twente
Prof. Dr. Alfredo R. de Faria	-	ITA

ITA

Acknowledgments

First and foremost I would like to thank my supervisors Richard Loendersloot from the University of Twente and Mauricio Donadon from Instituto Tecnológico de Aeronática for their continuous support and being always available for questions and feedback. Richard Loendersloot, I am specifically grateful to you for always making me think twice about why I was taking a certain approach during the research. Moreover, your supportive criticism and attention for detail have really helped in sharpening the research. Mauricio Donadon, to you I am grateful for giving me the opportunity to come to Brazil. It has been an inspiring year that would not have been possible without you. Moreover, without your vast knowledge on composite testing and modelling I would likely still be working in the lab right now. Lastly, thank you for the Friday afternoons with beer & music in the lab.

I also want to express my gratitude towards Ricardo Gouvéa for helping me everyday during my experiments. It not only speeded up the process, but also made the countless hours spend performing the c-scans much more bearable. Additionally, Mariano Marbelo thank you for aiding me in the build up of my numerical model. After being stuck for days sometimes you always managed to give just enough clues to figure out how to solve the problem.

Finally, I would like to express my appreciation to all my family and friends. Mom and dad, thank you for the continuous support. Even when my enthusiasm to do everything and go everywhere made me stay away from home for long periods of time, you have always stood by my side. To my brother and sister you have always inspired me to go the extra mile during my studies, for which I am very grateful. To all my friends from ITA and the University of Twente, thank you for making sure I did not forget about other things in life besides studying. You guys have made my student time a period in which I have gained so much more than just theoretical knowledge. I will never forget these experiences.

For now, I hope you will enjoy reading this master thesis report.

Bart van den Akker

July 2018, São José dos Campos, Brazil

"We cannot direct the wind, but we can adjust the sails"
— Bertha Calloway

Management summary

To better understand and predict the behavior of composite bonded structures over an aircraft's life cycle the INOVA project was set up by Embraer and Instituto Tecnológico de Aeronáutica. As part of this project, the goal of the research described in this work is to determine the post-buckling fatigue behavior of co-bonded composite stiffened panels with an initial disbond before and after hygrothermal aging. Moreover, a numerical simulation of the post-buckling fatigue was created to aid in the actual implementation of the gained insights in the industry. This was summarized in the following research question:

What is the influence of hygrothermal aging on the post-buckling fatigue behavior of co-bonded composite stiffened panels and how can this cyclic loading be simulated efficiently and accurately?

To be able to answer this question stiffened CFRP panels with an artificial disbond were subjected to 300,000 compression load cycles between -4.7 and -47.5 kN and subsequently tested for their residual strength. During the cyclic loading the disbond size was monitored using a c-scan device. The influence of hygrothermal aging was investigated by comparing panels under room temperature ambient (RTA) and room temperature wet (RTW) conditions. The RTW panels had been aged for 280-396 days at 80°C and 90% humidity.

As figure 1a shows, the disbond of the RTW panels grew less during the cyclic loading than the disbond of the RTA panels. Three factors were identified that potentially contributed to this phenomenon. Firstly, the fracture toughness may have increased due to stress relaxation caused by the presence of moisture. Secondly, the moisture in the adhesive may have also lead to crack blunting. A more blunt crack in turn leads to lower stress concentrations at the crack tip and therefore less growth in fatigue. The last identified factor that may have contributed to the decrease in disbond growth is the fact that the RTW panels had a larger disbond after pre-cracking than the RTA panels. Numerical simulations showed that by itself this could have caused a decrease in disbond growth of roughly 15%.

The residual strength tests demonstrated that the cyclic loading and related disbond growth did not cause a significant loss in strength or overall stiffness in the panels. Similarly, the hygrothermal aging had no significant influence on either parameter. This is demonstrated in figure 1b, which displays the load-shortening curves of two non cyclic loaded reference panels and two post-cyclic loading panels up to failure.

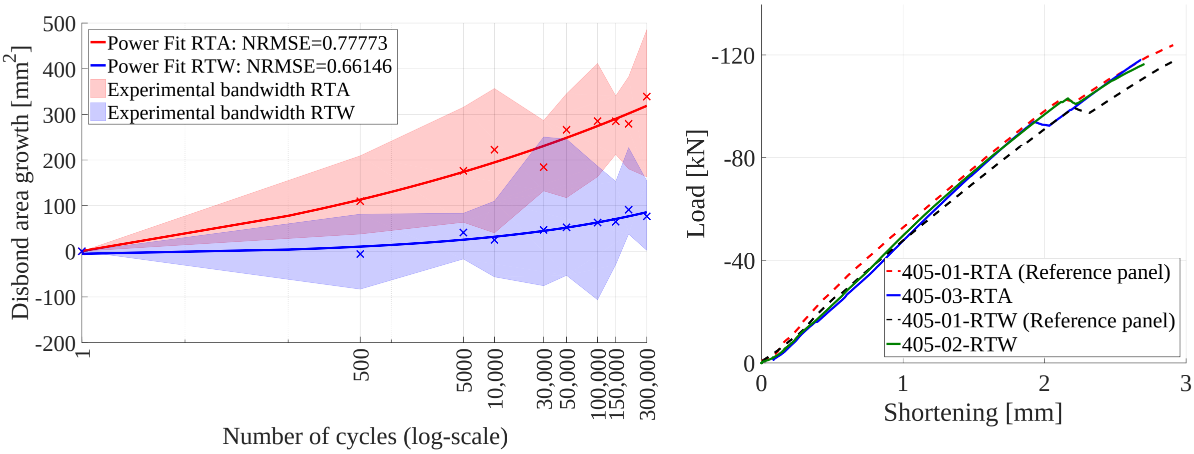

(a) Growth disbonded area during cyclic loading (b) Quasi-static compression until failure

FIGURE 1 – Results of the cyclic and quasi-static compression experiments

The cohesive zone model developed by Oliveira (2018) was used to simulate the damage in the adhesive during the post-buckling cyclic loading of the RTA panels. Figure 2a shows that the growth of the disbonded area predicted by the numerical simulation underestimates the experimental growth by roughly 25%. The two main factors that might have caused the discrepancy in growth are the fact that the Paris law parameters and static strength of the interface layer were not available for the correct material combination and thus had to be taken from similar materials and the relatively low accuracy of the c-scan.

The residual strength of the panels was modelled with the same cohesive zone model as for the fatigue damage, extended with damage in the CFRP using Hashin's damage model. From figure 2b it can be seen that the simulation overestimates the residual strength by 14%. This may again be caused by the inaccurate strength of the interface layer, or because the numerical simulation assumed perfectly clamped ends, whereas the experimental boundary conditions were not clamped perfectly.

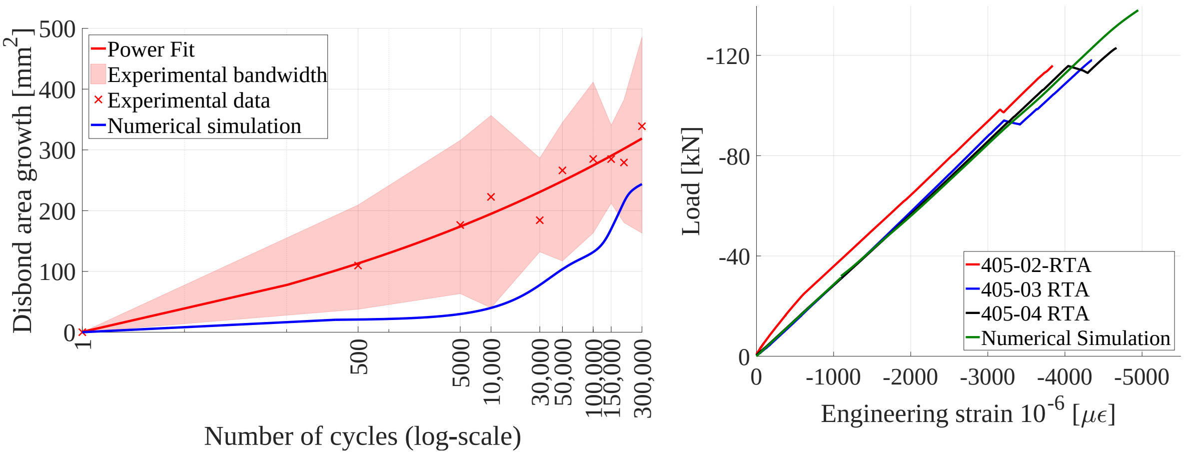

(a) Growth disbonded area during cyclic loading (b) Membrane strain in the stiffener

FIGURE 2 – Results of the cyclic and residual strength numerical simulations

As this study showed that the influence of hygrothermal aging on the post-buckling fatigue behavior of composite stiffened panels is limited, it is recommended to further investigate what the influence would be of cold temperature environments. The moisture in hygrothermally aged specimens causes the adhesive to plasticize, whereas in cold temperatures they become more brittle. Potentially leading to reversed results. Another interesting field for future research could be the joining techniques of thermoplastic composites. The use of thermoplastics in aircraft is on the rise, with two obvious advantages being their increased fracture toughness and recyclability. As of currently no large scale research comparing different joining techniques over the course of an aircraft's life exists for thermoplastic parts.

List of Figures

List of Tables

List of Abbreviations and Acronyms

4-ENF	Four end notch flexure
CFRP	Carbon fiber reinforced polymer
CZM	Cohesive zone model
DIC	Digital image correlation
DCB	Double cantilever beam
FAA	Federal Aviation Administration
FEM	Finite element model
FRP	Fiber reinforced polymer
ITA	Instituto Tecnológico de Aeronáutica (Technological Institute of Aeronautics)
LVDT	Linear variable differential transformer
MMB	Mixed mode bending
NRMSE	Normalized root mean square error
RG	Relative humidity
RTA	Room temperature ambient
RTW	Room temperature wet
SERR	Strain energy release rate
SG	Strain gauge
SIF	Stress intensity factor
VCCT	Virtual crack closure technique
XFEM	Extended finite element method

List of Symbols

Symbol	Description	Unit
a	Crack/disbond length	[mm]
A	Crack/disbond area	[mm]
B	Specimen thickness	[mm]
C	Fitting parameter	[-]
D	Damage parameter CZM	[-]
E	Young's modulus	[MPa]
G	Strain energy release rate	[N/mm]
$\bar{G}$	Mixed mode equivalent G	[N/mm]
G_c	Fracture toughness	[N/mm]
h	Element thickness	[mm]
k	Stiffness	[N/mm]
K	Stress intensity factor	[MPa $\sqrt{\text{mm}}$]
l_e	Element length	[mm]
m	Fitting parameter	[-]
n	Fitting parameter	[-]
N	Number of cycles	[-]
P	Load	[N]
R	Load or stress ratio	[-]
S	Strength	[MPa]
T_g	Glass transition temperature	°C
u	Displacement in x-direction [mm]	
U	Energy released upon crack extension	[j]
v	Displacement in y-direction	[mm]
w	Displacement in z-direction	[mm]
W	Specimen width	[mm]
W_t	Panel weight at time t	[kg]
W_0	Initial weight of the panel	[kg]
X_i	Load at node i in x-direction	[N]
Y_i	Load at node i in y-direction	[N]

Greek symbols

γ	Shear strain	[-]
δ	Relative displacement of element faces	[mm]
$\bar{\delta}$	Mixed mode equivalent relative displacement	[mm]
$\triangle$	Amplitude	[-]
ϵ	Normal strain	[-]

η	B-K interpolation coefficient	[-]
μ	Shear modulus	[MPa]
ν	Poisson's ratio	[-]
Π	Potential energy	[J]
ρ	Density	[ton/mm^3]
σ	Stress	[MPa]
$\bar{\sigma}$	Mixed mode equivalent stress	[MPa]
$\hat{\sigma}$	Effective stress	[MPa]
σ_y	Yield stress	[MPa]
τ	Shear stress	[MPa]
ϕ	Measure of mixed mode ratio	[-]

Subscripts

0	Onset of softening	[-]
1	Fiber direction	[-]
2	In plane transverse to fiber direction	[-]
3	Out of plane transverse to fiber direction	[-]
b	Element bottom face	[-]
f	Failure	[-]
fi	Fiber	[-]
I	Mode I fracture	[-]
II	Mode II fracture	[-]
III	Mode III fracture	[-]
m	Matrix	[-]
max	Maximum value within a load cycle	[-]
min	Minimum value within a load cycle	[-]
t	Element top face	[-]
th	Threshold below which no fatigue damage occurs	[-]

Superscripts

C	Compression	[-]
f	Fatigue	[-]
s	Static	[-]
T	Tensile	[-]

Contents

1 Introduction

In this chapter an introduction to the executed research is presented. To create a better understanding of the larger scope of this research, section 1.1 presents a general background on the use of adhesive bonding in the aircraft industry. Subsequently, section 1.2 treats the scientific context in which the research can be placed. Based on the scientific context, gaps in the knowledge on adhesive bonding in aircraft are identified. Based on this a research objective is derived in section 1.3. The research questions are treated in section 1.4 and finally the research methodology can be found in section 1.5.

1.1 General background

As part of a global effort to reduce climate change, the aviation industry, in the form of the Air Transport Action Group, has set forward a goal of 1.5% annual fuel reduction until 2020, carbon neutral growth from 2020 onwards and a 50% net decrease in carbon emissions by 2050 [ATAG 2010]. This goal is supported by over 1600 airports, 230 airlines and over 8500 companies operating in the global business aviation community. Among these companies are major aircraft builders such as Boeing, Airbus and Embraer.

Weight reduction plays an important role in increasing the fuel efficiency per aircraft seat. This has turned the attention of researchers and companies alike towards the use of lightweight materials such as composites [Holmes 2017]. This is evident in the growth of composite use in aircraft over the past 50 years, as can be seen in figure 1.1. Especially fiber reinforced plastics (FRPs) have gained momentum because their mechanical properties suit the aerospace industry well. They are lightweight, while possessing high specific stiffness and strength, are damage tolerant and perform well in cyclic loading over a wide range of temperatures [Rana *et al.* 2016, Davim e Reis 2003, Pramanik *et al.* 2017].

Currently, both mechanical fastening and adhesive bonding are used to join composite components. The appeal of adhesive bonding lies in the fact that, unlike with mechanical fasteners such as rivets and bolts, it does not require drilling. Holes cause stress concentrations which can be associated with crack initiation [Mouritz 2012, Olgin *et al.* 2015, Davim e Reis 2003, Pramanik *et al.* 2017]. Additionally, the uniform stress distribution of adhesive bonds leads to higher stiffness [Silva *et al.* 2011, Olgin *et al.* 2015]. Other advantages of adhesive bonding include liquid and air tight sealing and more cost effective manufacturing [Olgin *et al.* 2015, Davim e Reis 2003].

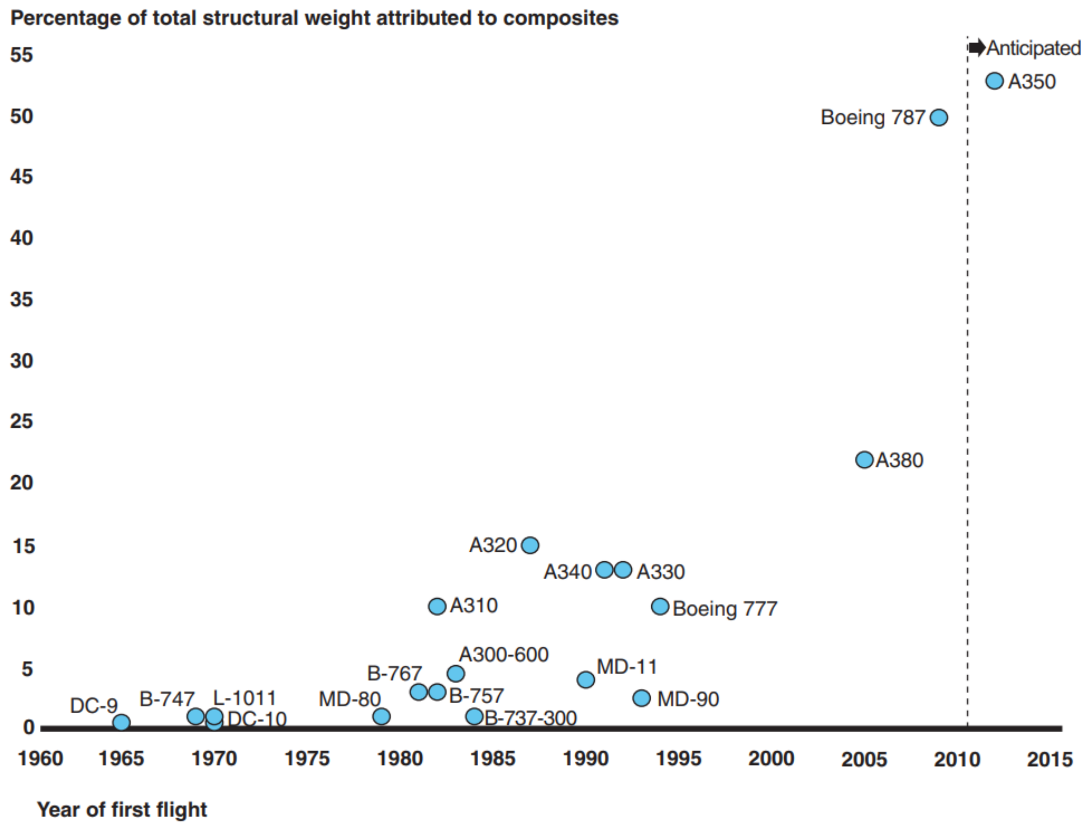

FIGURE 1.1 – Percentage of composite weight in aircraft over the years [Dillingham 2011]

One of the disadvantages associated with adhesive bonding in aircraft structures is the lack of reversibility of the bonding process. This can lead to unnecessarily damaged materials upon disassembling and increased difficulties for inspection and maintenance [Pramanik *et al.* 2017, Song *et al.* 2010]. To solve this problem reversible bonding processes, using for example pressure sensitive adhesives, are currently an active field of research [Sun *et al.* 2013]. They have already successfully been applied in for example the automotive, packaging and architectural industries. An additional problem associated with bonded joints is their susceptibility to environmental factors such as UV, humidity and temperature fluctuations [Song *et al.* 2010, Budhe *et al.* 2017].

Despite having been used in aircraft structures for over 60 years, the fatigue behavior of bonded joints is not yet fully understood [Higgins 2000, Molent e Forrester 2017]. In 2009 a slow crack growth approach for certification on composite and adhesively bonded structures was introduced by the US Federal Aviation Administration (FAA) (2010). This allows damage tolerant design of adhesively bonded structures with predictable crack growth and a reasonable lifetime between crack detection and tolerable crack size. Damage tolerant designed structures can withstand design loads and function properly even in the presence of these cracks and other forms of damage [Mouritz 2012]. However, due to the aforementioned lack of knowledge on fatigue life behavior of bonded structures the actual application of this approach has not yet reached its full potential [Molent e Forrester 2017]. This can potentially lead to the over design of structures.

1.2 Context

In the past extensive research has been performed towards the use of adhesive bonding in aircraft structures. This section aims to create an overview of several areas that have already been studied extensively and in which areas knowledge can and should still be gained. In this regard subsection 1.2.1 focuses on the post-buckling of bonded composite panels and subsection 1.2.2 treats the hygrothermal aging of these panels.

1.2.1 Post-buckling of bonded composite stiffened panels

The majority of an aircraft's structure consists of sheet material, referred to as the skin, with attached stiffeners [Stevens *et al.* 1994]. The skin is efficient for in-plane loading, whereas the stiffeners improve the buckling behavior. This combination leads to a more efficient design compared to increasing the skin thickness [Yap *et al.* 2002]. To optimize the weight of the structure, the skin can be allowed to buckle below the ultimate load [Niu 1995, Lynch *et al.* 2004, Yap *et al.* 2002].

In the past research has been performed towards the behavior of bonded composite stiffened structures. Especially the static buckling [Zhao e Kapania 2016, Stevens *et al.* 1994, Aslan e Sahin 2009] and post-buckling behavior [Wang *et al.* 2015, Stevens *et al.* 1994, Kong *et al.* 1998, Falzon *et al.* 2000, Aslan e Sahin 2009, Meeks *et al.* 2005, Bisagni e Davila 2014, Orifici *et al.* 2008, Bisagni *et al.* 2011, Bisagni 2006, Vescovini *et al.* 2013, Yap *et al.* 2002] of bonded composite stiffened panels have been well defined in the literature. These studies have demonstrated that panels are capable of taking loads far beyond the initial buckling load, even when a disbond between skin and stiffener is present. Although care has to be taken with the growth of this delamination, as this can occur at loads below the ultimate load of a pristine panel [Yap *et al.* 2002].

Delamination can potentially become an even bigger problem when the panel is subjected to cyclic loading. Three studies available in the open literature have been dedicated to the investigation of the influence of post-buckling fatigue on bonded composite stiffened panel-like structures with an initial delamination [Cordisco e Bisagni 2011, Davila e Bisagni 2017, Abramovich e Weller 2010]. Cordisco and Bisagni (2011) have shown that closed box structures with an initial disbond are capable of taking significant cyclic shear loads (275% of the original buckling load) without observable disbond growth for thousands of cycles. However, they did mention that they expect cyclic compression to be more critical than cyclic shear loading.

Davila and Bisagni (2017) and Abramovich and Weller (2010) did investigate the influence of cyclic post-buckling loading on bonded composite panels with an initial disbond under pure compression. Both concluded that stiffened bonded composite panels can safely be taken into the post-buckling compression regime for many load cycles. The panels of Davila and Bisagni (2017) failed after a maximum of 25,521 cycles at a combination of 80 and 85% of the static ultimate load, whereas the panel of Abramovich and Weller (2010) managed to withstand 63,281 cycles at 2.5 up to 3.3 times the local buckling load.

An interesting difference between the studies by Davila and Bisagni (2017) and Abramovich and Weller (2010) is the fact that the former measured significant disbond growth during the cyclic loading, whereas the latter did not. This disparity is likely caused by differences in the experimental set-up. However, due to the low amount of studies in this field, the exact causes are hard to determine. Unfortunately, neither study used finite element modelling to simulate the cyclic loading of the panels in the post-buckling regime. This makes it more difficult for aircraft manufacturers to extrapolate the gained insights into the aforementioned slow crack growth approach for composite bonded joints as proposed by the FAA (2010).

1.2.2 Effects of hygrothermal aging on the post-buckling behavior of bonded composite stiffened panels

In addition to the above described research with respect to the post-buckling of stiffened panels, environmental aging of bonded composite joints is another active field of research. During the lifetime of an aircraft it is exposed to environmental factors such as UV, moisture, temperature cycling and sometimes even fire [Pantelakis e Tserpes 2014, Budhe *et al.* 2017, Feng *et al.* 2015]. Budhe et al. (2017) state that of these factors moisture and temperature effects are currently considered to be the most important. However, their combined effects are not yet fully understood [Song *et al.* 2010, Budhe *et al.* 2017].

In line with this is the statement made by Feng et al. (2015) that the influence of hygrothermal aging, a combination of temperature and moisture, on the buckling and post-buckling behavior of composite stiffened panels has so far been treated insufficiently in the literature. Feng et al. (2015) investigated the influence of hygrothermal aging in 70°C water while performing quasi-static experiments at the same elevated temperature and at 95% moisture conditions. It was concluded that in a fully saturated panel the buckling patterns and failure modes did not change compared to the non aged panels tested at room temperature conditions. However, the ultimate load did decrease by 22.2%, as did the buckling load by 3.1%.

Even though the combination of thermal expansion and swelling due to moisture uptake may especially lead to problems in adhesively bonded joints in cyclic loading, no relevant studies were found in the open literature on the influence of hygrothermal aging on bonded composite panels subjected to post-buckling fatigue [Costa *et al.* 2017].

1.3 Research objective

With the above described gaps in the literature in mind, the INOVA project was initiated by Embraer and Instituto Tecnológico de Aeronáutica (ITA). For clarity purposes the main identified gaps are repeated here:

- Numerical simulation of post-buckling fatigue damage in bonded composite stiffened panels to increase the use of the slow crack growth approach proposed by the FAA
- Consequences of hygrothermal aging on post-buckling fatigue damage in bonded composite stiffened panels

In the subsections below first an introduction of the INOVA project is given and the role of this thesis in the project is discussed. Based on this a research objective is formulated. Subsequently, the conditions imposed by the INOVA project are treated.

1.3.1 Project introduction

The research proposed in this work is part of the INOVA project. INOVA is a collaboration between ITA and Embraer aiming to get a more thorough understanding of the behavior of bonded composite structures over the course of an aircraft's life cycle. It is the first in its kind by comparing the different bonding techniques of carbon fiber reinforced polymer (CFRP) currently applied in the aircraft industry. These bonding techniques include co-bonding, secondary bonding and co-curing.

During the INOVA project coupon level experiments were carried out to determine the fracture toughness and the fatigue threshold of each bonding technique. Half of these coupons were subjected to hygrothermal aging and subsequently tested at elevated temperature to determine the influence of hot-wet conditions on the mechanical properties of a bonded structure. Additionally, all bonding techniques were (or are going to be) tested on sub-component level in the form of stiffened bonded panels with an initial disbond subjected to cyclic post-buckling loading. Again, half of these panels were hygrothermally aged. Testing of these panels however takes place at room temperature conditions due to equipment restrictions. By performing these experiments the INOVA projects aids aircraft manufacturers in choosing the right bonding type for each application, as well as define robust design methodologies.

The scope of this thesis is limited to co-bonded panels. Both non-aged panels, called room temperature ambient (RTA), and hygrothermally aged, called room temperature wet (RTW), panels will be tested experimentally. By doing so it will be the first work available in the open literature investigating the influence of hygrothermal aging on bonded composite panels over the course of an aircraft's life cycle. Additionally, a numerical simulation of the consequences of the cyclic post-buckling loading will be carried out. At the start of this thesis no report of such a work was available in the open literature. Performing this feat will aid aircraft manufacturers in using a damage tolerant design approach for bonded composite parts.

It has to be noted that the numerical simulations will only be carried out for the RTA panels, as no coupon level experiments were carried out for the RTW conditions. Therefore insufficient information is available on the mechanical properties of the RTW material for successful numerical simulation.

The above described scope can be summarized in the following research objective:

To numerically simulate the behavior of co-bonded composite stiffened panels loaded cyclically in compression and to analyze the influence of hygrothermal aging on the post-buckling fatigue damage of these panels experimentally.

1.3.2 INOVA project conditions

To create uniformity throughout the project all panels are of the same dimensions. These dimensions are depicted in figures 1.2 and 1.3. To investigate the disbond growth during the post-buckling fatigue an artificial disbond of 100 mm was created using a Teflon^{TM} tape.

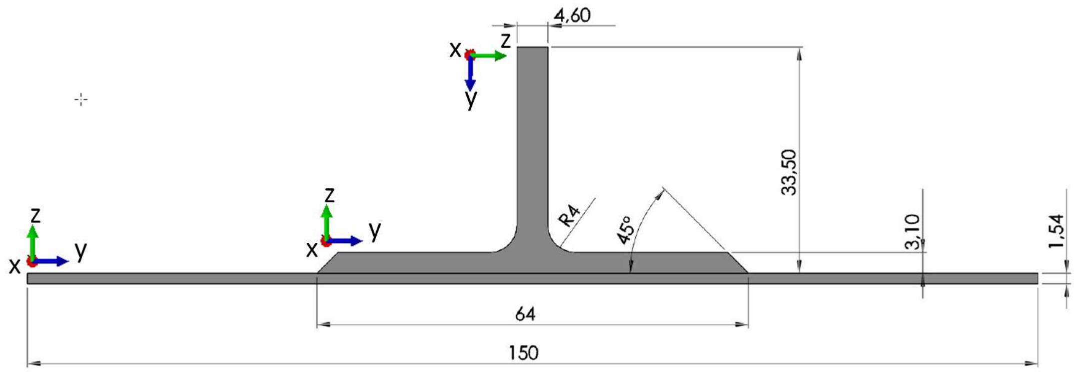

FIGURE 1.2 – Front view of the panels (dimensions in mm)
Local axes are used to indicate lay-up direction in section 3.1

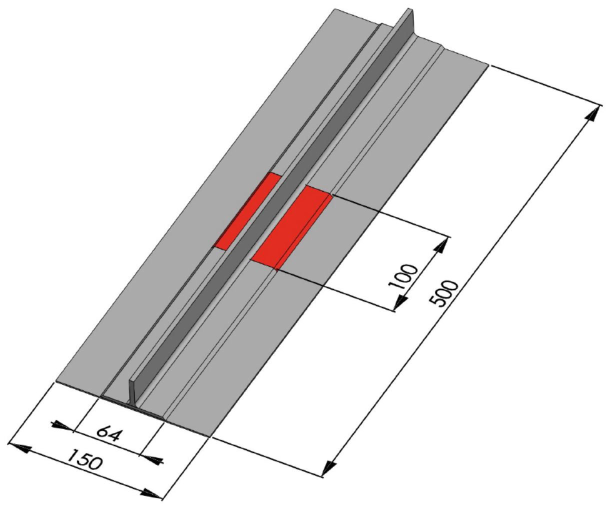

FIGURE 1.3 – Isometric view of the panels, Teflon insert depicted in red (dimensions in mm)

The conditions for hygrothermal aging were also pre-determined by the agreements in the INOVA project. The panels were kept in an environmental chamber at 80°C and 90% humidity until the start of the experiments. Total aging time varied due to the moment of testing, but was between 280 and 396 days. The aging temperature remained below the glass transition temperature (T_g) of both the CFRP adherent (166-204°C) and the adhesive (95-150°C) [Toray 2017, Henkel Adhesives]. The aging conditions, materials and composite lay-up will be treated more thoroughly in chapter 3.

1.4 Research questions

Based on the research objective described in section 1.3, the following research question is formulated:

What is the influence of hygrothermal aging on the post-buckling fatigue behavior of co-bonded composite stiffened panels and how can this cyclic loading be simulated efficiently and accurately?

This research question covers the entire scope of the research. However, to get a clearer overview of the steps required to answer this question it is divided in two sub-questions. The first sub-question is related to the experimental part of this research and investigates the post-buckling compression fatigue behavior of bonded composite stiffened panels, before and after hygrothermal aging:

1. <u>What is the influence of cyclic post-buckling loading on co-bonded composite stiffened panels with a disbond and how does hygrothermal aging affect this?</u>

   Before this question can be investigated it is important to gain more background knowledge on the effects of hygrothermal aging on co-bonded joints and the post-buckling behavior of composite stiffened panels in general. Therefore, first the following tertiary questions have to be answered through a literature review:

   a) What are the effects of hygrothermal aging on the mechanical behavior of co-bonded CFRP joints?

   b) How does disbond size affect the quasi-static buckling and post-buckling behavior of bonded composite stiffened panels?

   c) What is the state of the art knowledge on the effects of cyclic post-buckling loading on composite stiffened panels?

The second sub-question is concerned with the numerical part of this research. It will investigate how the post-buckling fatigue damage can best be simulated:

2. <u>How can post-buckling fatigue damage in a composite stiffened panel be numerically modeled both efficiently and accurately?</u>

   To answer this question, it is essential to first know what type of damage the model actually needs to be able to simulate and which techniques are available to do so. Therefore, a literature review will be conducted to investigate the following tertiary questions:

   a) What type(s) of damage does a numerical model of cyclic post-buckling loading of bonded composite panels need to be able to simulate?

   b) Which numerical techniques are currently available to model this damage?

   c) Which of these techniques is most suitable for the current application?

1.5 Research method

To answer the research question proposed in section 1.4 the research is divided in four phases. The first phase consists of a literature review and answers the tertiary questions proposed in section 1.4. Its focus lies on the influence of hygrothermal aging on bonded parts, the post-buckling of bonded CFRP panels and on the numerical techniques currently available to model post-buckling fatigue damage in bonded composite panels. The literature review can be found in chapter 2.

The second phase of the research is the experimental part, which is further divided in three steps. Step I consists of quasi-static compression tests until failure with one RTA and one RTW panel. These serve as a reference for the cyclically loaded panels. Moreover, these reference panels are used to:

- Make sure the panel buckles at the intended cyclic load
- Get an initial grasp of the influence of the hygrothermal aging on the panels
- Benchmark the numerical model in a quasi-static fashion

Step II handles the fatigue experiments. Both the RTA and RTW panels will be loaded for a total of 300,000 cycles between -4.7 and -47.5 kN. During these cycles the disbond growth and stiffness of the panel are monitored.

Step III consists of residual strength tests. During this step similar quasi-static compression tests are performed as during step I, only now with panels that have previously been loaded cyclically in step II. Step II and III will directly contribute to answer research sub-question 1. The methodology behind these experiments is treated more thoroughly in chapter 3. Their results are discussed in chapter 4.

The third phase of the research treats the numerical part, related to research sub-question 2. It focuses on constructing a numerical model capable of simulating the post-buckling fatigue experiments. Similarly to the experimental phase, it is divided in three steps, with each step corresponding to one of the experimental steps. The numerical models, their validations and results are treated in chapter 5.

During the final phase of the research the answer to the research question is formulated. Moreover, recommendations for further research are made. Both topics can be found in chapter 6.

2 Literature Study

The literature study aims to create a thorough overview of the state-of-the-art knowledge relevant to this research. It is divided in four sections, three of which can be directly related to the tertiary questions posed in section 1.4. Section 2.1 is not related to these tertiary questions as it discusses the bonding techniques currently applied in the aircraft industry and the possible failure modes of co-bonded joints. This is considered essential background knowledge for readers due to the broader scope of the INOVA project.

Section 2.2 discusses the influence of hygrothermal aging on bonded joints, corresponding to the tertiary research question 1a). Section 2.3 presents the influence of the size of the debonded area on the static buckling and post-buckling behavior of bonded composite stiffened panels, as well as the influence of cyclic compression loading on bonded composite stiffened panels. In doing so it aims to answer the tertiary research questions 1b) and 1c). Finally, section 2.4 is related to the tertiary research questions 2a), 2b) and 2c). It elaborates on what the numerical model needs to be able to simulate and which types of numerical models currently exist that are capable of doing so. It concludes by choosing a specific model type to simulate the post-buckling fatigue damage.

2.1 Co-Bonding

To create a better understanding of co-bonding in composite structures this section starts of by treating the different bonding techniques available for composite structures in subsection 2.1.1. Subsequently, subsection 2.1.2 discusses the different failure modes that can occur in co-bonded structures.

2.1.1 Different bonding techniques

Budhe et al. (2017) state that three different bonding processes are used for composite joining: co-bonding, co-curing and secondary bonding. Additionally, it is also possible to bond other materials, such as metals, to composites. All four methods can be seen in figure 2.1. In a co-curing manufacturing process both laminates are cured simultaneously [Budhe *et al.* 2017]. This can be done both with and without an adhesive in between the parts [Song *et al.* 2010]. Co-bonded joints are created by using one cured and one un-cured part and subsequently curing the adhesive and un-cured part simultaneously [Budhe *et al.* 2017,Song *et al.* 2010]. Finally, secondary bonding is achieved by curing an adhesive in between two pre-cured composite parts [Budhe *et al.* 2017,Song *et al.* 2010].

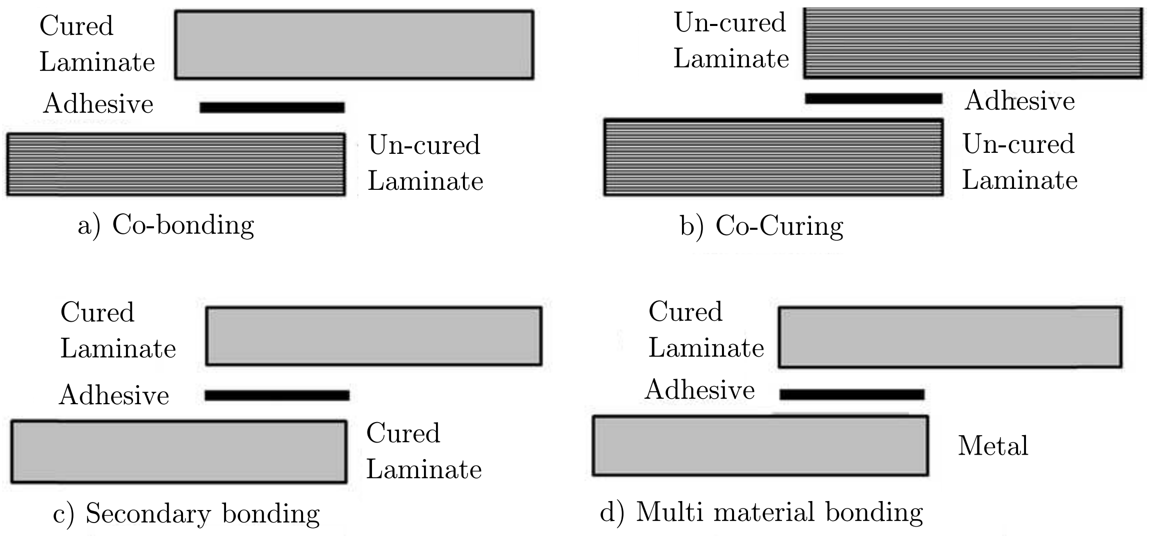

FIGURE 2.1 – Different bonding techniques [Budhe *et al.* 2017]

The type of bonding method chosen can greatly influence the mechanical properties of a bonded structure [Kim *et al.* 2006,Song *et al.* 2010,Mohan *et al.* 2014]. To demonstrate this influence this subsection treats the bond strength and fracture toughness for various bonding techniques. Bond strength can be defined as the average stress in the bond at which failure occurs [Kim *et al.* 2006]. Fracture toughness is defined as a material's resistance to crack growth [Anderson 2005]. These two mechanical properties were chosen because they are considered vital for both the fatigue induced crack growth and the strength of the panel. It has to be noted that mechanical properties of bonded composite joints are also dependent on many other factors, such as bond moisture, temperature, adhesive material, adherent material and surface preparation. This means that trends visible in one study can not be directly extrapolated to other studies.

Bond strength

Several researchers have compared the bond strength of different bonding techniques. Kim et al. (2006) compared co-cured bonds with and without adhesive to secondary bonds. They used unidirectional carbon epoxy prepreg laminates with two different types of epoxy adhesive: FM73 (co-cured) and Hysol EA9309NA (secondary bonded). The highest shear strength was achieved in the co-cured bond without any adhesive, followed by the secondary bonded and co-cured specimens. The co-cured specimen ended up being the weakest despite the FM73 adhesive having superior mechanical properties to the Hysol EA9309NA. Kim et al. (2006) attributed this to the fact that the failure mode of the co-cured specimens with adhesive was delamination, which reduces the joint strength. Whereas failure in the adhesive layer, as occurred in the secondary bonded specimen, tends to delays crack growth.

Song et al. (2010) also tested the shear strength of different bonding techniques on coupon level. In addition to the bonding techniques tested by Kim et al. (2006) they also tested co-bonded specimens. Carbon-epoxy laminates were used in combination with the epoxy adhesive FM300 K. Their results confirm the order of bond strength as described by Kim et al. (2006). Furthermore, in their tests co-bonded specimens possessed the lowest strength of all four manufacturing methods. However, from these results it can not simply be concluded that one bonding method is stronger than another, as the performance of bonds is also dependent on many other factors such as bond moisture, temperature, adhesive material, adherent material, surface preparation, ply orientation, overlap length etc. [Budhe *et al.* 2017, Song *et al.* 2010].

Fracture toughness

According to Anderson (2005) a crack can endure three types of loading. In mode I the load is normal to the crack plane and therefore opens the crack. In mode II in-plane shear loading is present and the crack faces slide with respect to each other. Mode III corresponds to out-of-plane shear loading. Additionally, a crack can endure any combination of the three above described phenomena. All three modes can be seen in figure 2.2.

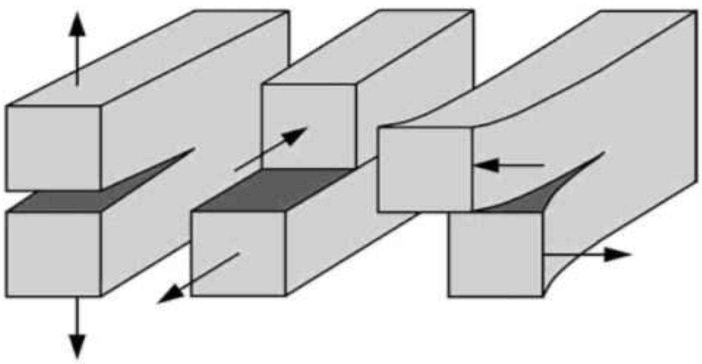

FIGURE 2.2 – Fracture modes of a crack [Anderson 2005]

The fracture toughness of a material is often denoted as the mode I (G_{Ic}) and mode II (G_{IIc}) fracture toughnesses in combination with an interpolation function to determine the intermediate mixed mode values. The mode III fracture toughness (G_{IIIc}) is generally assumed equal to the mode II fracture toughness because no standardized tests are available to determine it. In this research this same approach will be followed.

Mohan et al. (2014) compared the mode I fracture toughness of a co-cured specimen with adhesive to one that was secondary bonded. They used carbon fibre epoxy laminates in combination with FM300-2M adhesive. It was shown that the mode I fracture toughness of the secondary bonded specimen was higher than for the co-cured specimen. In a related research Mohan et al. (2015) concluded that the mode II fracture toughness of both bonding techniques was 5-6 times higher than their corresponding mode I fracture toughness.

As part of the INOVA project, Brito (2017) and Brito et al. (2017) performed a comparative study towards the fracture toughness of co-cured, co-bonded and secondary bonded specimens on coupon level. The same materials were used as in this research: epoxy carbon fiber composite with an epoxy adhesive. More information on the materials and curing cycle will be presented in chapter 3. Per mode mixture two types of fracture toughnesses were reported: fracture initiation and propagation. Fracture initiation is interesting when no pre-crack is used. Since in this research pre-cracked specimens will be used only the propagation values will be reported.

The obtained fracture toughness for both mode I and mode II can be seen in table 2.1. At first the mode II fracture toughness of the co-cured specimens seems to stand out, but actually it is more in line with the results obtained by for example Mohan et al. (2015) than the spread in values obtained for co-bonded and secondary bonded joints. The mode II fracture toughness of the material combination used in this research is very high in compared to for example the work of Mohan et al. (2015) and Floros et al. (2015).

TABLE 2.1 – Mode I and mode II fracture toughness as obtained by Brito (2017) and Brito et al. (2017)

Bending technology	G_{Ic} [N/mm]	G_{IIc} [N/mm]
Co-cured	0.23	0.816
Co-bonded	0.235	6.961
Secondary bonded	0.22	6.383

It has to be noted that although the studies performed by Brito (2017) and Mohan et al. (2014) and (2015) reported a mode I fracture toughness lower than the mode II fracture toughness, this is not necessarily the case for all materials, as was demonstrated by Floros et al. (2015).

2.1.2 Failure modes for co-bonded structures

According to the ASTM-D5573-99 (1999) standard six different failure modes exist for composite bonded structures, all of which are depicted in figure 2.3. Adhesive failure consists of separation at the adhesive-adherent interface and is therefore also referred to as interface failure (figure 2.3 a). Cohesive failure occurs when the failure is inside the adhesive (figure 2.3 b). Thin-layer cohesive failure takes place, similarly to cohesive failure, inside the adhesive but much closer to the adhesive-adherent interface (figure 2.3 c). Fiber-tear failure occurs in the adherent with fibers present on both sides of the crack (figure 2.3 d). Similarly, light-fiber-tear takes place in the adherent, but much closer to the interface. Although matrix resin is visible on the adhesive, typically no or few fibers are observable (figure 2.3 e). Lastly, stock-break failure is when the bonded specimen fails outside the bonded region. Often the failure occurs in the proximity of the bonded region (figure 2.3 f). Final failure of a specimen can occur as any combination of the above described failure modes.

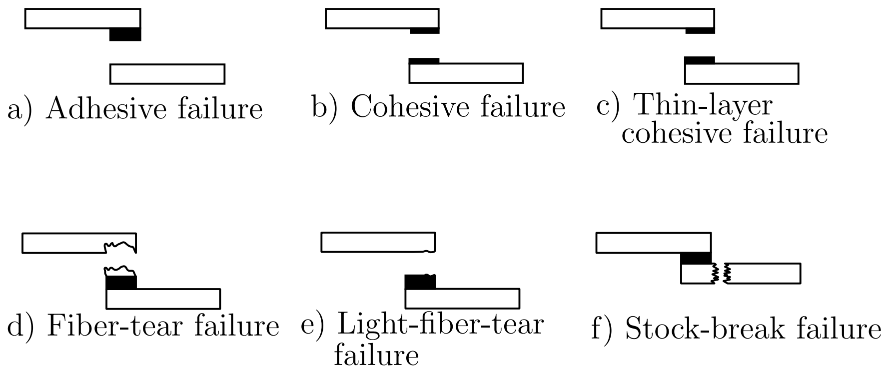

FIGURE 2.3 – Failure modes according to ASTM D5573-99 (1999)

Typically these failure modes are used to examine the reason behind failure of a specimen afterwards, not as a prediction tool beforehand. This is because many parameters such as moisture, loading type and specimen configuration all influence which failure mode occurs [Budhe *et al.* 2017].

2.1.3 Concluding remarks

The most important conclusion is that the mechanical properties of bonded composite joints are dependent on many factors such as bonding technique, bond moisture, temperature, adhesive material, adherent material and surface preparation. The fact that the mechanical properties of the bonds are based on these factors means that trends visible in one study, or more specifically for one material combination, can sometimes be completely reversed in another study.

For the material set-up used in this study the fracture toughness of all three bonding techniques in mode I is similar. In mode II however the co-cured specimens were outperformed by the co-bonded and secondary bonded specimens. The mode I and mode II fracture toughness of the co-bonded panels used in this panel can be found in table 2.1.

2.2 The influence of hygrothermal aging on bonded joints

To get a clear grasp of what hygrothermal aging does to bonded structures the separate effects of moisture in bonded joints and the aging of these bonds in thermal environments are discussed in subsections 2.2.1 and 2.2.2. Subsequently, subsection 2.2.3 elaborates on the effects of hygrothermal aging on the strength and fracture toughness of bonded composite joints. Finally, subsection 2.2.4 extrapolates these gained insights to how the hygrothermal aging is expected to influence the panels in this research.

2.2.1 Influence of post-bond moisture on bonded joints

This subsection elaborates on the effects of post bond moisture on bonded joints. The total moisture absorption and the effect of the moisture absorption on the mechanical properties of the bond are dependent on various factors such as the used material, curing cycle, bonding method and exposure conditions [Budhe *et al.* 2017]. To get a clear understanding of the influence of post-bond moisture on bonded CFRP joints, first a general introduction of its effects on the adhesive, the adherent and the adhesive-adherent interface is given. Subsequently, the consequences of post-bond moisture on the bond strength and fracture toughness of bonded structures are treated.

Influence of moisture on the adhesive

The presence of moisture affects adhesives in several ways. Firstly, it can cause them to plasticize [Budhe *et al.* 2017, McBrierty *et al.* 1999, Sciolti *et al.* 2010, Viana *et al.* 2016, LaPlante e Lee-Sullivan 2005]. Plasticizing subsequently leads to a decrease in glass transition temperature, yield stress (σ_y) and Young's modulus (E), while increasing the strain to failure (ϵ_f) [McBrierty *et al.* 1999, LaPlante e Lee-Sullivan 2005, Viana *et al.* 2016]. A small amount of plasticization can also lead to a decrease of stress concentrations in highly stressed areas [Hutchinson e Hollaway 1999].

Abdelkader and White (2005) state that the plasticization of epoxies is caused by the bonding of water molecules and hydrogen bonds present in the polymer. In doing so they interrupt the interchain bonding of the epoxy, causing the swelling and plasticization. They state that water uptake can also take place without bonding to the polymer. In this case the water gets absorbed by the free volume and has little influence on the overall properties. In addition to plasticizing and swelling, moisture uptake can also lead to hydrolysis and the growth of existing cracks [Budhe *et al.* 2017, LaPlante e Lee-Sullivan 2005, Sciolti *et al.* 2010].

Influence of moisture on the adherent

The effect of moisture on fiber reinforced polymers has been widely researched [Sciolti *et al.* 2010, Cervenka *et al.* 1998, Karbhari e Ghosh 2009, Pickering *et al.* 2016, Abanilla *et al.* 2005, Abanilla *et al.* 2006]. The matrix resin in a CFRP tends to be affected more severely than the carbon fibers [Hutchinson e Hollaway 1999, Fernandes *et al.* 2016]. Glass fibers on the other hand can corrode and aramid fibers can absorb water, leading to a decrease in their mechanical properties as well [Hutchinson e Hollaway 1999].

Epoxy matrices are particularly capable of absorbing large amounts of water [Sciolti *et al.* 2010]. The effects of moisture on epoxy resins is very similar to those described for (epoxy) adhesives. Relative to the total mass, adhesives can absorb more water than the adherents however [Fernandes *et al.* 2016]. Sciolti et al. (2010) mentioned that in addition to the problems occurring in the adhesive, problems in the adherent can be related to the fiber-matrix interface. Internal stresses can arise due to the fact that the fibers limit the swelling of the matrix. Additionally the moisture can penetrate in the fiber-matrix interface and deteriorate the bonding.

The fact that fibers are only margianally effected by moisture has the consequence that mechanical properties dependend mostly on the fibers, such as tensile strength, remain relatively unchanged [Sciolti *et al.* 2010]. However, a decrease in tensile strength for thicker specimens was reported by Abanilla et al. (2005). But this was caused by a decrease in interlaminar strength, which is actually a matrix dominated property. Other mechanical properties related to the matrix, such as shear strength, generally decrease due to the absorption of moisture [Budhe *et al.* 2017, Sciolti *et al.* 2010]. It is reported by Abanilla et al. (2006) that the interlaminar fracture toughness on the other hand increases due to water absorption. This can be explained by the increased flexibility and plasticity of the resin, which results in a more blunt crack.

Influence of moisture on the adherent-adhesive interface

Budhe et al. (2017) state that the adherent-adhesive interface in the presence of moisture is one of the most important factors influencing the long term durability of bonded joints. However, to validate this point they refer to a study investigating the influence of pre-bond moisture [Budhe *et al.* 2014] and an article which actually states that interfacial effects can be minimized by using high quality surface treatments [Mubashar *et al.* 2011]. In the study performed by Mubashar et al. (2011) anodising was used as a surface treatment, resulting in mechanical locking at the interface. According to the authors this makes it highly unlikely that the interface can be replaced by a layer of water. Consequently, they state that with the right surface treatment the adherent-adhesive interface is affected less than the bulk adhesive material.

Influence of moisture on bond strength

Karbhari and Ghosh (2009) compared the durability of CFRP specimens adhesively bonded to concrete using three different bond set-ups and four different environments in which they were exposed to water. Each specimen set-up used an epoxy based adhesive with different additives. It has to be noted that the usage of porous concrete on one side will not give the same results as a fully bonded CFRP structure. However, it can still give a good indication of the effect of moisture on the durability of bonds.

The pull-of strength of all bonded structures after prolonged immersion in deionized water or salt water, ponding in both water types, or a combination of high humidity and ponding in both water types, decreased. Additionally, the bond strengths displayed a strong time-dependency, as the deterioration continued until the last moment of measuring, which was after 24 months. The severity of the strength loss was different for each set-up and environmental condition and are not considered relevant for this research due to the differences in test set-up.

Influence of moisture on bond fracture toughness

Fernandes et al. (2016a) compared the influence of different humidity levels on the mode I and mode II fracture toughness of secondary bonded specimens. They used epoxy-carbon prepreg plies in combination with the epoxy adhesive Araldite 2015. The degradation scenarios were four months at 55% relative humidity (RH), 75% RH at 50 °C and immersion in 50°C distilled water. Unfortunately, the increased temperatures of these last two made their results not solely moisture dependent. An average decrease of 22% was observed for the mode I fracture toughness of the samples kept at 75% RH and 48% for the immersed samples. The mode II fracture toughness of the immersed sample decreased 37% and remained constant for the humid environments.

The above is an indication of the negative influence of moisture on the fracture toughness of bonded structures. Exposure to higher moisture contents lead to more severe degradation both in mode I and mode II. For the specimen set-up presented above, mode I was affected stronger by the moisture than mode II. It has to be noted that Hutchinson and Hollaway (1999) state that a small amount of moisture, and thus plastization, can also lead to an increase of fracture toughness. Another remark has to be made about the reversibility of the moisture effects by drying. As several studies have shown that drying of a specimen after exposure to post-bond moisture can, at least partially, restore the lost fracture toughness and bond strength [Hutchinson e Hollaway 1999, Budhe *et al.* 2014, Mubashar *et al.* 2011]

2.2.2 Influence of temperature on bonded joints

In this subsection the residual effects of thermal degradation are discussed. The instant effects of temperature on the bond are out of the scope of this research, as all tests are performed at room temperature. The focus lies on specimens aged at elevated temperatures, not cryogenic temperatures.

Similar to the set-up used to discuss the influence of post-bond moisture, first a general introduction on the effect of aging at elevated temperatures on the adhesive, adherent and adhesive-adherent interface is be given. Subsequently, the consequences for the bond strength and fracture toughness are discussed.

Influence of temperature on the adhesive

Exposure to cyclic temperatures below T_g is considered advantageous to both the adhesive and CFRPs due to post-curing of the resin [Hutchinson e Hollaway 1999]. Post-curing results in an increase of the Young's modulus, tensile strength and ultimate strain of the adhesive [Garden e Hollaway 1997, Hutchinson e Hollaway 1999]. However, as the temperature gets closer to the glass transition temperature adhesives tend to soften, which in turn can increase their moisture uptake [Heshmati *et al.* 2015, Karbhari *et al.* 2003].

Influence of temperature on the adherent

Hutchinson and Hollaway (1999) state that the positive effect of post-curing below T_g is viable for CFRPs, but not for GFRPs. Exposure to cyclic temperatures is also associated with progressive fiber-matrix debonding due to the difference in thermal expansion coefficient between matrix and fiber, especially as the matrix becomes more viscous at higher temperatures [Karbhari *et al.* 2003]. Hutchinson and Hollaway (1999) however state that this should not be a problem for well prepared composites.

Foster and Bisby (2005) reported that elevated temperatures in normal use should not have a significant effect on the fibers, as their allowable temperature range is typically significantly larger than that of the matrix. They stated that the tensile strength and stiffness of the CFRPs tested in their experiments did not decrease until close to 400 °C. In the same study Foster and Bisby (2005) showed that epoxy based matrices already experience decomposition at temperatures slightly above T_g (100°C vs T_g=78°C). Additionally, permanent deformations occurred once the specimens were heated above T_g due to the differences in thermal expansion coefficients.

Influence of temperature on the bond strength

In a different study by Foster and Bisby (2008) the residual shear strength of bonded FRPs after thermal degradation was tested. The CFRP bonded specimens retained more than 80% of their shear strength up to an exposure temperature of 250°C for 3 hours. This was surprising because the epoxy itself had already lost 90% of its tensile strength at this point. This indicates that the shear properties of epoxies are affected differently than the tensile properties. Above 250°C all specimens showed rapid decrease in shear strength.

Influence of temperature on the bond fracture toughness

The influence of short term aging at elevated temperatures on the mode I fracture toughness of bonded CFRP specimens was studied by Markatos et al. (2013). They reported that exposure of one hour resulted in a 62% decrease of the mode I fracture toughness. Fernandes et al. (2016b) investigated the effect of long term exposure to different temperatures on the mode I and mode II fracture toughness of bonded specimens. They stored bonded CFRP specimens at 0°C, 25 °C and 50°C for 3 months. The mode I fracture toughness of the specimens stored at 0 and 25 °C was similar. However, the G_{Ic} of the samples stored at 50°C was roughly one third lower than those stored at lower temperatures. This was attributed to the proximity of the glass transition temperature of the used adhesive (Araldite 2015 with a $T_g \approx 75$°C). The mode II fracture toughness was seemingly uninfluenced by the change in storage temperature. Indicating that G_{Ic} is more susceptible to aging by temperature than G_{IIc}.

2.2.3 Influence of hygrothermal aging on bonded joints

Exposure to a hygrothermal environment is expected to lead to a more severe degradation of the bond's properties than when exposed to a humid or hot environment alone [Budhe *et al.* 2017]. The effects of hygrothermal aging on adherents, adhesives and their interface are a combination of the effects of moisture and temperature treated in subsections 2.2.1 and 2.2.2. Therefore, these are not repeated here. Rather, only the influence of hygrothermal aging on the mechanical properties bond strength and fracture toughness is treated below.

The influence of hygrothermal aging on the bond strength

In a study by Halliday et al. (2000) secondary bonded CFRP coupons were immersed in 70°C water for 0-423 days. Throughout the entire aging period water uptake took place, though faster in the beginning than at the end. Similarly, the shear strength decreased faster in the beginning than at the end. An exception being the measurement point after 128 days, at which moment, as can be seen in figure 2.4, the shear strength had actually increased 2.3% compared to day 0. This was explained by relaxation of the internal stress in the CFRP adherents.

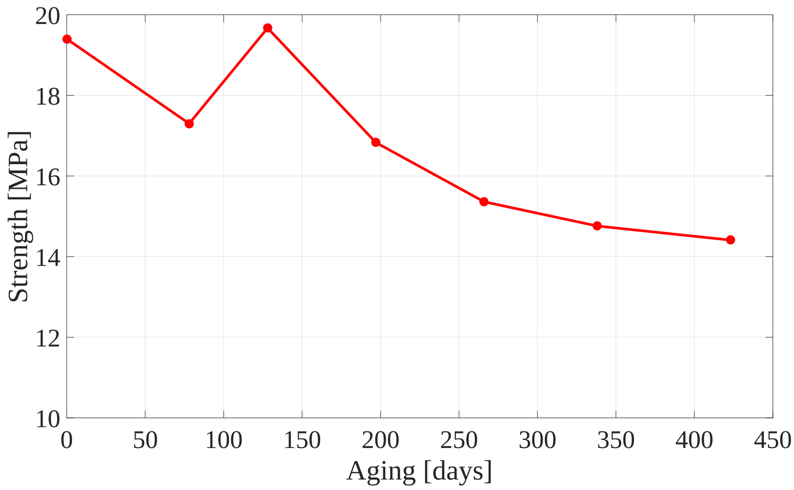

FIGURE 2.4 – Influence of hygrothermal aging on the shear strength of secondary bonded specimens [Halliday *et al.* 2000]

The influence of hygrothermal aging on the fracture toughness

The previously mentioned study performed by Halliday et al. (2000) also investigated the consequences of environmental aging on the mode I fracture toughness of the bond. All specimens were pre-cracked 60 mm before immersion into the water. In figure 2.5 the evolution of the fracture toughness at the crack initiation point for different immersion times is shown.

Whereas the bond strength showed an improvement after 128 days, the fracture toughness at the initial crack tip already increased after 78 days. The total increase with respect to day 0 at this point was 24.3%. Halliday et al. (2000) also dedicate this increase to stress relaxation. They state that this effect is reached faster for the initiation fracture toughness than the bond strength because the crack tip is exposed to 4 edges, compared to 2 for the rest of the bond. This increased the water penetration. After 423 days the fracture initiation toughness is only 33.3% of the day 0 G_{Ic}, compared to the 74.7% which remained for the shear strength. Also interesting to note is that the failure mode changed from interlaminar for the original specimens to a combination of cohesive and adhesive failure after aging. Indicating degradation in the adhesive and adhesive-adherent interface.

Figure 2.5 also shows the fracture toughness of the specimens after a growth of 25 mm. It can be seen that the overall degradation is less severe than at the crack initiation point. Additionally, it is interesting to note that the sharp increase in fracture toughness after 78 days is replaced by 2 smaller increases after 128 and 423 days, indicating a more stable overall response. This results in a 15% decrease of the mode I fracture toughness after 423 days of immersion, compared to 66.7% at the original crack tip. Based on the fracture toughness of the specimens at crack lengths between 0 and 50 mm growth the authors conclude that the initial fracture toughness is influenced significantly by the aging, whereas the bulk fracture toughness only shows minor reductions. The reason why the propagation fracture toughness shows different behavior than the crack initiation fracture toughness after aging has to do with the direct exposure of the original crack tip to the hot and humid environment and the aforementioned exposure to 4 edges instead of 2.

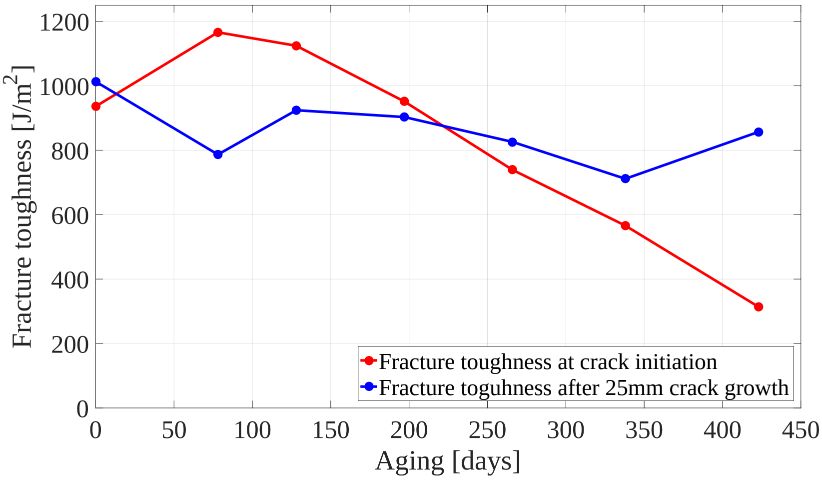

FIGURE 2.5 – Comparison of fracture toughnesses of hygrothermally aged specimens at crack initiation and after 20mm of crack growth [Halliday *et al.* 2000]

LaPlante and Lee-Sullivan (2005) looked specifically at the influence of hygrothermal aging on the fracture toughness of the adhesive. In this research the epoxy adhesive FM300 was used. The adhesive was subjected to 3 different hygrothermal conditions: 60% relative humidity at room temperature (RH condition), 60% relative humidity at 60°C (HH) and immersed in 70°C water (HW). The moisture uptake of the HH and HW conditions can be seen in figure 2.6. After over 1000 hours of aging both the HH and HW condition had not reached their equilibrium moisture content yet.

Interestingly, the average mode I fracture toughness of both the HW and HH conditions were respectively 20 and 15 percent higher after aging than before. Once again, this positive result is attributed to stress relaxation. This is in agreement with the results obtained by [Halliday *et al.* 2000] for shorter aging periods.

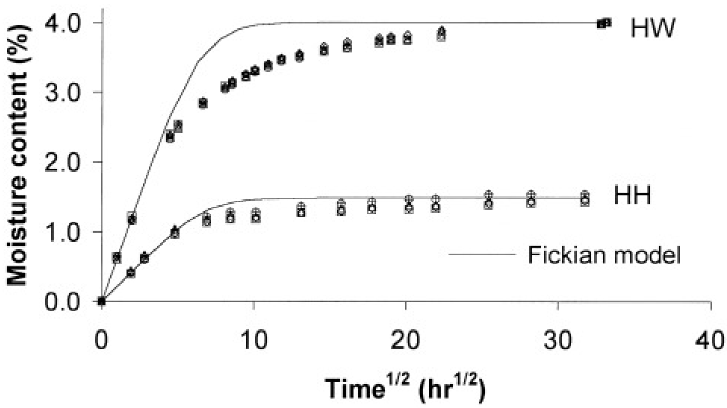

FIGURE 2.6 – Moisture absorption of an FM300 adhesive [LaPlante e Lee-Sullivan 2005]

2.2.4 Expected consequences of the hygrothermal aging used in this research

The goal of this section was to answer the first tertiary research question:

1a) What are the effects of hygrothermal aging on the mechanical behavior of co-bonded CFRP joints?

The answer to this question is summarized in tables 2.2 and 2.3.

TABLE 2.2 – Possible effects of moisture and elevated temperature on the mechanical properties of CFRP bonded structures.

Moisture	**Temperature**
*Unless stated otherwise, the effects below are related to the epoxy resin in the adhesive and matrix	
+ Increase of ϵ_f	
+ Stress relaxation	+ Post-curing (below T_g)
± Fibers remain unaffected	± Little effect on G_{IIc} at temperatures near T_g
− Lower T_g	− Decrease of bond strength (shear and tensile) at temperatures above T_g
− Lower σ_y	− Decrease of G_{Ic} after prolonged exposure near T_g
− Lower E	− Rapid decrease of G_{Ic} at temperatures above T_g
− Degradation of the fiber-matrix interface	
− Swelling induced stresses	
− Decrease in bond strength (shear and tensile)	
− Deacrease of G_{Ic} and G_{IIc}	

TABLE 2.3 – Possible effects of hygrothermal aging on the mechanical properties of CFRP bonded structures.

Effected area	**Effect**
Bond strength	+ Possible initial increase of shear strength − Prolonged exposure results in a decrease in shear strength
Fracture toughness	+ Possible initial increase of G_{Ic} ± G_{Ic} is influenced mostly at the crack initiation point − Prolonged exposure results in a decrease in G_{Ic}

These tables are quite generalistic. However, they help in extrapolating the gained insights towards how hygrothermal aging is expected to affect the panels specifically in this study.

The fiber related mechanical properties are expected to remain unaffected by the hygrothermal aging. This is due to the fact that moisture has little influence on the fibers and the temperature remains far below the 300-400°C for which Foster and Bisby (2005) reported fiber degradation. The matrix and adhesive are more likely to show signs of degradation, as they are more sensitive to moisture and tend to degrade at lower temperatures. Moisture can lower their stiffness, yield stress, strength and mode I and II fracture toughness. For the adhesive this effect might be enlarged by the fact that the temperature during aging (80°C) is close to its glass transition temperature (95°C when wet).

Halliday et al. (2000) performed a study on the influence of hygrothermal aging on the shear strength and mode I fracture toughness of bonded CFRP with somewhat similar aging conditions (70°C immersion in water) as used in this study (80°C 90% humidity). They noted a decrease in shear strength of the bond of roughly 20%. The mode I fracture in this same study mainly decreased at the fracture initiation point. Only a small amount of degradation could be distinguished after 2 mm of crack growth. This indicates that the mode I disbond growth in the fatigue experiments of this study might not be effected a lot by the hygrothermal aging. However, as the aging temperature of Halliday et al. (2000) was 10°C lower, and as was pointed out above the temperature is close to T_g, this effect could be more severe in this study. Unfortunately no study was found on the influence of hygrothermal aging on the mode II fracture toughness at RTW conditions.

Overall the decreased strength of the epoxy matrix and adhesive can cause the strength of the panels to decrease. The stiffness is not expected to change as this property is dominated by the fibers. Whether or not the disbond growth during the cyclic loading will be significantly different is not entirely clear due to the limited amount of information available on this subject.

2.3 Buckling and post-buckling of bonded composite stiffened panels

As stated in the introductory section 1.2, buckling and post-buckling of bonded composite structures is a well researched topic. This section aims to create an overview of the relevant parts of these studies. In subsection 2.3.1 an introduction is given on buckling in stiffened panels. Thereafter, the influence of the disbond size on the buckling and post-buckling behavior of composite stiffened panels is treated in subsection 2.3.2. This is relevant to determine the influence of the expected delamination growth during the cyclic loading. Finally, subsection 2.3.3 discusses the influence of cyclic post-buckling loading on the mechanical behavior of the panel.

2.3.1 Background

Buckling can occur in panels due to loading in compression, shear or a combination of both. Stiffeners are attached to the panels to improve their resistance against buckling. They do so, from a weight perspective point of view, in a more efficient way than increasing the skin thickness [Yap *et al.* 2002]. To allow further weight savings the stiffened panels are often designed to take significant loads beyond the initial buckling load [Niu 1995, Lynch *et al.* 2004, Yap *et al.* 2002].

Initially the response of an ideal stiffened panel under compression is linear. The point where it starts deviate from linearity is also referred to as the bifurcation point [Yap *et al.* 2004]. In figure 2.7 this is referred to as the point of local buckling. From a mathematical point of view two equilibrium solutions are possible for every loading scenario beyond the bifurcation point: one solution with purely compressed linear behavior and one non-linear solution with out of plane deformation [Yap *et al.* 2004]. Yap et al. (2004) state that in practice structures will always follow the non-linear path up to the ultimate load. From the ultimate load onward the stiffness drops and a structure is considered failed.

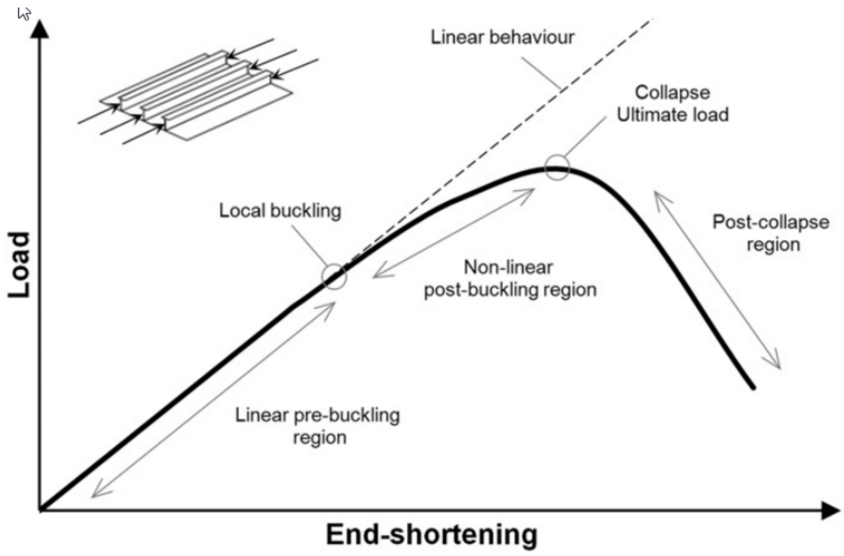

FIGURE 2.7 – Typical load vs. in plane displacement curve of a stiffened panel [Paulo *et al.* 2013]

Two types of buckling exist for stiffened panels: global buckling and local buckling. Global buckling modes deform both the stiffeners and the skin, whereas local buckling modes only deform one of the two [Lamberti *et al.* 2003]. Local buckling modes arise due to defects, such as delaminations, and can influence the global buckling behavior. They lower the overall buckling load and ultimate load and can lead to disbonding [Yap *et al.* 2004, Orifici *et al.* 2008, Yap *et al.* 2002]. Figure 2.8 shows examples of both global and local buckling modes for the skin and stiffener.

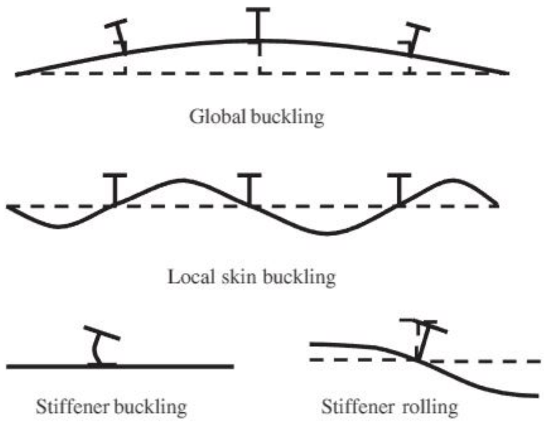

FIGURE 2.8 – Different buckling modes of stiffened panels [Lamberti *et al.* 2003]

2.3.2 The influence of disbond size on the buckling and post-buckling behavior

Yap et al. (2002) performed a numerical study towards the influence of a disbond's size, width and location on the stability of stiffened panels. The model was based on a curved panel with 4 pre-cured stiffeners co-bonded to the skin. Before discussing the results of this study it has to be noted that the buckling loads and mode shapes of curved panels are different than those of their flat counterparts [Tran *et al.* 2014].

According to Yap et al. (2002) the disbond size of panels can be divided into three categories:

- Small disbond: < 10% of the panel's length
- Medium disbond: 10-24% of the panel's length
- Large disbond: > 24% of the panel's length

This distinction is based on the fact that in the numerical model of Yap et al. (2002) small disbonds buckle globally before they buckle locally, whereas medium and large disbonds buckle locally first. The difference between medium and large disbonds is that medium sized disbonds have a single half wave buckling shape and large disbonds three half-waves. The influence of the disbond size on several mechanical aspects of the panels can be seen in figure 2.9. According to Yap et al. (2002), the disbond size barely influences the global buckling load, whereas the local buckling load is mainly influenced up to a disbond size of 18%.

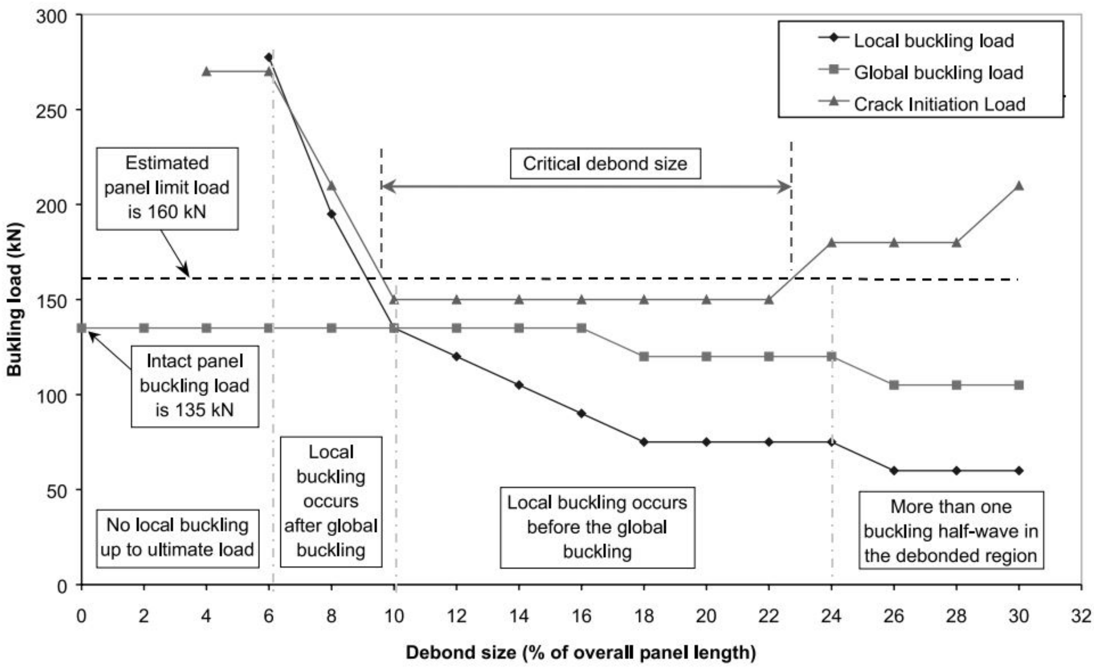

FIGURE 2.9 – Influence of debond size on local buckling load, global buckling load and crack initiation load [Yap *et al.* 2002]

Based on the information provided through the numerical study of Yap et al. (2002) below the influence of the disbond size on the buckling mode, stiffness and strength of stiffened CFRP panels will be treated

Buckling mode

Yap et al. (2002) suggest that a medium sized disbond results in the most critical buckling mode: a single half wave. This buckling mode promotes mode I crack opening, whereas larger disbonds result in a mode II dominant buckling shape with three single half waves. They state that this causes medium sized disbonds to have more crack growth than large disbonds because the mode I fracture toughness of bonded composite panels is generally lower than the mode II fracture toughness.

These results from Yap et al. (2002) can not be extrapolated to any other study however, as buckling modes depend on more than just the disbond size. Factors such as boundary conditions and the location of the disbond also play a major role. For example in a study by Bisagni and Davila (2014), in which a hat stringer was used with a medium sized disbond (13.3% of the panel's length) underneath only one flange, three half waves were observed and no noticeable delamination growth took place before the collapse load. Similarly, the results obtained by Orifici et al. (2008) suggest that the buckling mode can't be related to just the disbond size of a panel. They tested a panel with a large sized disbond (26.67%) and registered a single half wave buckling mode. This single half wave was however accompanied by disbond growth below the ultimate load of the panel.

Although the buckling mode and disbond size can not be related directly, the above described information strengthens the statement from Yap et al. (2002) that the buckling mode and the occurrence of delamination growth are related. All single half wave buckling shapes are accompanied by significant delamination growth before or near final collapse, whereas the buckling mode containing three half waves observed by Bisagni and Davila (2014) is not accompanied by disbond growth. Moreover, Orifici et al. (2008) tested a second panel with the same boundary conditions and a slightly different design. Although the disbond length was similar, the buckling shape of the panels with this design consisted of several half waves. Figure 2.10 displays the consequences of this mode shape change for the SERR along the width of the crack. The second design, with the several half waves buckling mode, resulted in significantly less delamination before final failure than the first design.

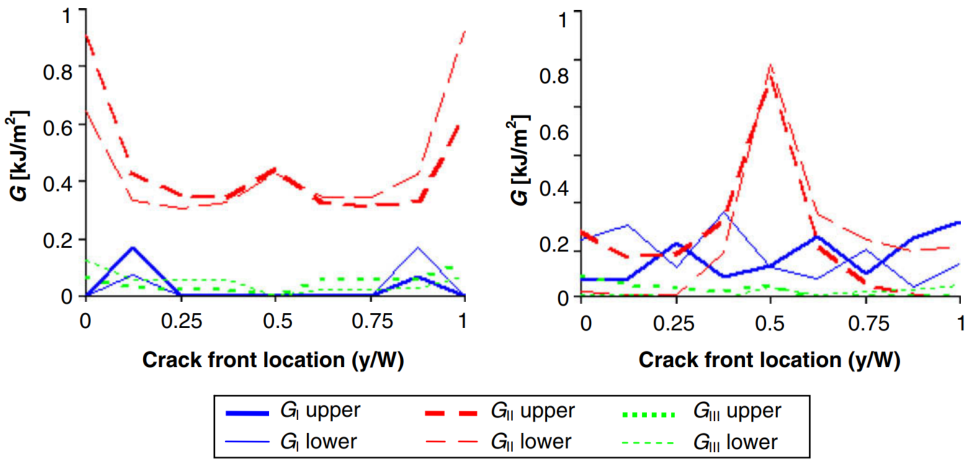

FIGURE 2.10 – Strain energy release rate along the width of the stiffener for design 1 (single half wave buckling mode) and design 2 (several half waves) [Orifici *et al.* 2008]

Stiffness

The presence of a delamination generally has little on influence the initial linear stiffness of the panel [Yap *et al.* 2002, Bisagni e Davila 2014, Abramovich e Weller 2010, Orifici *et al.* 2008]. It is expected that this is due to the dominant behavior stiffeners have on the stiffness of panels. The load displacement curves provided by Bisagni and Davila (2014), shown in figure 2.11, confirm this statement: no influence of the debonds on the initial stiffness and additionally no significant stiffness losses upon delamination growth during the test. The delamination growth can be recognized by a sudden drop in load in the load-displacement curve.

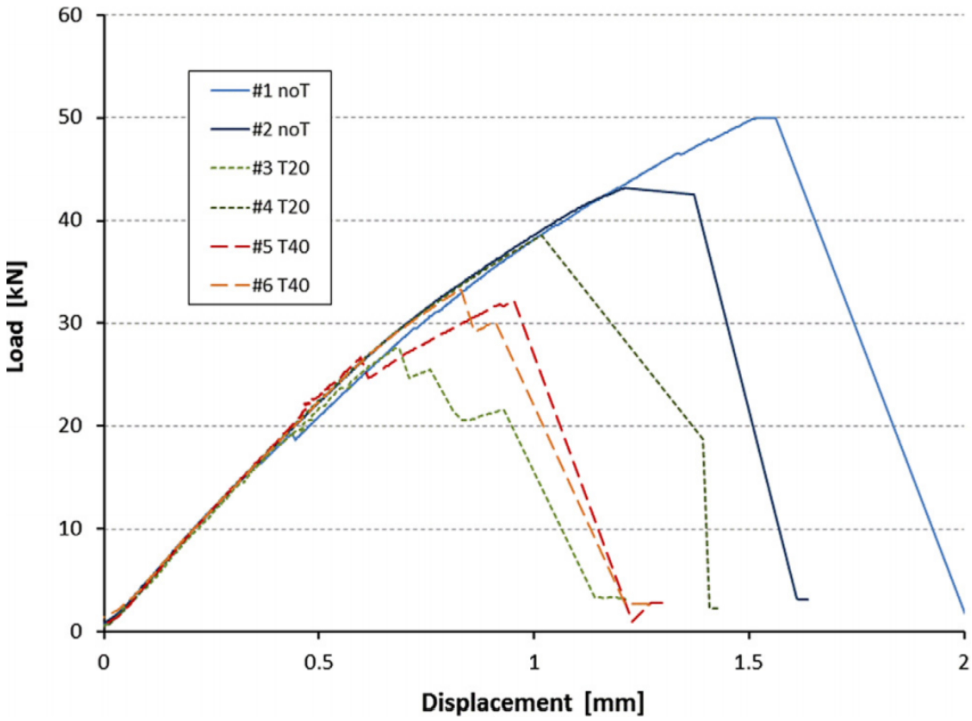

FIGURE 2.11 – Load-displacement curve for a co-cured single hat specimen with initial disbond of 0 (noT), 20 (T20) and 40mm (T40) [Bisagni e Davila 2014]

Ultimate load

The studie by Bisagni and Davila (2014) suggests that there is a potential correlation between the ultimate load of a bonded panel and the disbond size. They registered a 17% decrease in ultimate load for a small debond (6.67%) and a 28% decrease for a medium sized debond (13.33%). Orifici et al. (2008) reported an even bigger decrease of almost 50% for large sized debonds (26.67%). Boundary conditions in both studies were similar with a potted top and bottom and free edges. However, the type of debond was different, as Bisagni et al. (2014) used the previously described single Teflon strip underneath one flange of a hat stringer, whereas Orifit et al. (2008) used a full width Teflon strip underneath a T-stiffener. Therefore, one has to be careful with drawing any conclusions from the correlation between these two studies.

2.3.3 The influence of compression post-buckling fatigue on bonded composite stiffened panels

Two studies were found describing the compression post-buckling fatigue behavior of bonded composite stiffened panels [Abramovich e Weller 2010, Davila e Bisagni 2017].

Interestingly, both studies were performed using an initial disbond between the stiffener and panel and got very different results. Below the disbond growth during the cyclic loading and the influence on the stiffness of the panels are treated. Because all panels of Abramovich and Weller (2010) and Davila and Bisagni (2017) failed during the cyclic loading, no knowledge is available on the influence of the cyclic loading on the residual strength of the panels.

Disbond growth

Abramovich and Weller (2010) did not register any noticeable disbond growth during the cyclic loading until final collapse of the structure occurred at 63,821 cycles. Davila and Bisagni (2017) on the other hand did report significant disbond growth of up to 2.5 times the original disbond length of 40 mm. The reason for this difference is likely due to the difference in set-up. Abramovich and Weller (2010) used a large panel with 5 T-stiffeners, among which 3 contained a disbond classified as small by Yap et al. (2002). Davila and Bisagni (2017) used a single hat-stiffened panel with a medium sized disbond at one flange of the hat. Both set-ups can be seen in figure 2.12.

(a) Panel with 5 T-stiffeners and 3 disbonded areas [Abramovich e Weller 2010]

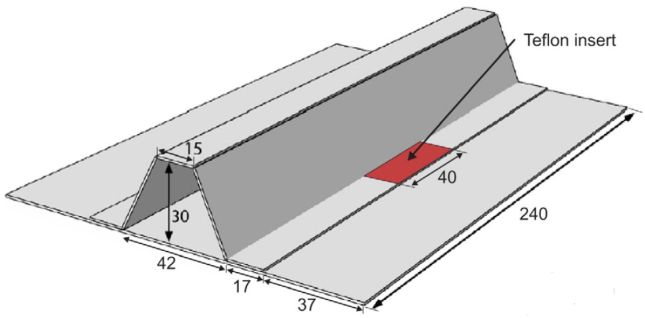

(b) Hat stiffened panel with single disbonded area [Davila e Bisagni 2017]

FIGURE 2.12 – Panels as used by Abramovich and Weller (2010) and Davila and Bisagni (2017).

Based on subsection 2.3.2 it seems likely that the disbond size present in the panel from Abramovich and Weller (2010) was too small to promote delamination growth prior to final failure if local buckling indeed occurred after global buckling. The disbond growth that was registered by Davila and Bisagni (2017) can be seen in figure 2.13. For both tested specimens the initial delamination growth occurred rather sudden. Respectively during the first cycle and after 2002 cycles. This was attributed to a combination of the high cyclic load of 80-85% of panels' static strength and residual glue being present around the Teflon insert. After the initial jump more stable mode I growth was observed until final collapse of the specimens after 6793 and 25,521 cycles.

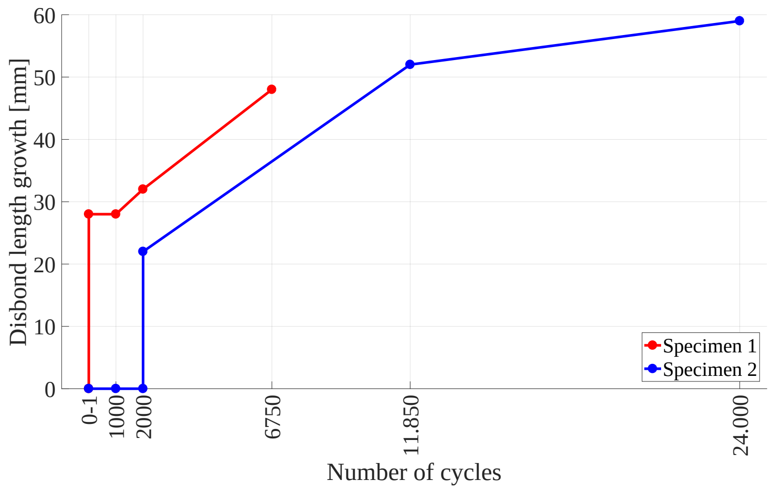

FIGURE 2.13 – Growth of disbond due to cyclic compression loading as observed by Davila and Bisagni [Davila e Bisagni 2017]

Stiffness

Abramovich and Weller (2010) registered no stiffness reduction of the panel throughout the entire testing procedure. This indicates that the translaminar and intralaminar damage in the panel due to the cyclic loading was limited. Davila and Bisagni (2017) on the other hand did mention that the stiffness of the panel declined after the sudden crack growth in the panels. They stated that this change was likely not caused by fatigue damage in the CFRP, but rather by residual adhesion that was still present around the Teflon and prohibited the skin from buckling before the sudden growth.

2.3.4 Concluding remarks

The tertiary research questions to be answered in this section were:

1b) How does disbond size affect the quasi-static buckling and post-buckling behavior of bonded composite stiffened panels?

1c) What is the state of the art knowledge on the effects of cyclic post-buckling loading on composite stiffened panels?

Small disbonds in CFRP stiffened panels (less than 10% of the panel's length) do not influence the global buckling load and tend to not buckle locally before globally [Yap *et al.* 2002, Abramovich e Weller 2010]. Yap et al. (2002) found that disbonds larger than 10% of the panel's length, such as the one used in this thesis, tend to buckle locally before globally. Although this specific number is only relevant for the boundary conditions and panel configuration used in that study, it is worth noting that Davila and Bisagni (2017), Bisagni and Davila (2014) and Orifici et al. (2008) indeed reported local buckling at disbonds larger than 10% of the panel's length. Moreover, Yap et al. (2002) state that as the size of the disbond increases, both the local and global buckling load decrease. Although the local buckling load only decreases up to a certain length (18% for the conditions of Yap et al. (2002))

Panels of which the skin buckles locally at the disbonded area can have problems with disbond growth well below the ultimate load of a pristine version of the same panel. The static load at which the disbond starts to grow is mainly dependent on the buckling shape of the skin buckling [Orifici *et al.* 2008, Yap *et al.* 2002]. Generally mode I opening, which occurs for example for a single half wave buckling mode, is the most critical scenario [Orifici *et al.* 2008, Yap *et al.* 2002, Bisagni e Davila 2014]. Static failure of stiffened panels with a disbond loaded in compression is often induced by this same skin-stiffener delamination [Yap *et al.* 2002, Stevens *et al.* 1994, Bisagni e Davila 2014, Bisagni 2006, Orifici *et al.* 2008].

The presence of a disbond generally does not significantly influence the stiffness of composite stiffened panels [Abramovich e Weller 2010, Bisagni e Davila 2014, Orifici *et al.* 2008, Yap *et al.* 2002]. The only exception being a study by Davila and Bisagni (2017) where stiffness reduction occurred between a panel with a disbond of 25% of the panel's length and a pristine panel.

Relatively little is known about the consequences of post-buckling compression fatigue on composite bonded panels. For a disbond to grow during the cyclic loading it needs to buckle locally at the disbonded area [Abramovich e Weller 2010, Davila e Bisagni 2017]. The amount of growth depends on the shape of the local buckling mode, with mode I opening once again proving critical [Davila e Bisagni 2017]. The stiffness of the panels does not tend to be affected by the cyclic compression loading [Abramovich e Weller 2010].

2.4 Numerical modeling of disbond growth during compression fatigue

For clarity purposes the tertiary research questions to be answered in this section are repeated here:

2a) What type(s) of damage does a numerical model of cyclic post-buckling loading of bonded composite panels need to be able to simulate?

2b) Which numerical techniques are currently available to model this damage?

2c) Which of these techniques is most suitable for the current application?

Based on subsection 2.3.3 it is expected that the main form of damage occurring in the panels will be delamination between the skin and stiffener, as neither Abramovich and Weller (2010) nor Davila and Bisagni (2017) reported significant damage in the CFRP due to post-buckling compression fatigue. Therefore, a numerical model capable of predicting fatigue delamination is sought.

Degrieck and van Paepegem (2001) classify fatigue models in three categories: fatigue life models, phenomenological models and progressive damage models. Fatigue life models use methods such as S-N curves or Goodman diagrams to formulate a fatigue failure criterion without predicting the actual degradation of the component. This criterion is generally a number of cycles at which the component fails. Phenomenological models describe the deterioration of mechanical properties such as residual strength and stiffness.

Degrieck and van Paepegem (2001) state that both of these categories are incapable of simulating actual damage growth. Progressive damage models, as the name suggests, do have this ability. They can be used to simulate the evolution of damage types such as delamination and matrix cracking and to predict residual mechanical properties due to damage accumulation. For this reason only progressive damage models will be further investigated.

2.4.1 Progressive damage models

Many types of progressive damage models exist. Pascoe et al. (2013) stated that when they are applied to the delamination of bonded structures four techniques can be distinguished:

- Stress/strain based methods
- Fracture mechanics based methods
- Cohesive zone models (CZMs)
- Extended finite element method (XFEM) based models

Stress/strain based methods use the stress, strain or strain energy to predict the crack growth per cycle ($\frac{da}{dN}$). An example of such a growth law using a stress based approach is [Poursartip e Chinatambi 1989]:

$$\frac{da}{dN} = C\left(\frac{1+R}{1-R}\right)^m (\triangle\sigma)^n \tag{2.1}$$

Where R is the stress ratio equal to $\frac{\sigma_{min}}{\sigma_{max}}$ and $\triangle\sigma$ the stress amplitude $\sigma_{max} - \sigma_{min}$. C, m and n are the fitting parameters.

Fracture mechanics based models use either the strain energy release rate (SERR) or the stress intensity factor (SIF) to predict crack growth. A typical fracture mechanics based progressive damage model is given by [Oliveira 2018]:

$$\frac{da}{dN} = C\left(\frac{\triangle G}{G_c}\right)^n \tag{2.2}$$

Where G depicts the SERR in the particular mode of interest. The most common technique to determine the SERR in FEM is the virtual crack closure technique (VCCT) [Pascoe *et al.* 2013,Krueger 2004]. VCCT uses the assumption made by Irwin (1958) that extension of a crack by $\triangle a$ requires the same energy as closing the crack over that length.

Cohesive zone modelling often goes hand in hand with the damage mechanics approach originally developed by Kachanov (1958) and Rabotnov (1969). In the damage mechanics approach an independent damage parameter is used to progressively reduce the stiffness of elements to zero [Pascoe *et al.* 2013,Silva e Campilho 2012]. The criteria upon which this happens are generally stress or fracture mechanics based. The unique part of the method is that it uses interface elements along the expected crack growth path and applies the damage law to those elements only.

The last category, XFEM, is unique in the fact that it allows crack growth in any direction. It does so by using virtual nodes that complement the regular nodes. These virtual nodes can move with respect to the regular nodes, which allows for discontinuities in the mesh. Initiation of this growth is generally again dependent on stress or fracture mechanics based criteria.

A more thorough explanation of all four techniques, including the most important advantages and disadvantages of each, can be found in appendix A.

2.4.2 Model choice

Of the methods proposed in subsection 2.4.1 CZM is currently the most widespread method for the prediction of static and fatigue damage in structures [Silva e Campilho 2012]. Stress/strain based methods have the problem that stresses at the crack tip are highly mesh depended and therefore require very a very fine local mesh [Anderson 2005, Silva e Campilho 2012]. Similarly, it has been shown that XFEM requires a finer mesh than CZMs [Campilho *et al.* 2011]. This makes CZM a more computationally efficient method than XFEM and stress/strain based methods. CZMs are also more efficient than the VCCT because the latter requires re-meshing after crack advancement, which can especially be time consuming for fatigue crack growth problems [Pascoe *et al.* 2013]. In CZM re-meshing is not necessary due to the use of interface elements.

The computational efficiency associated with CZM makes it the method of choice for the simulation of the cyclic post-buckling compression loading in this research. Unfortunately, no CZM, or any of the other previously mentioned methods, is readily available in Abaqus for the simulation of damage accumulation in high cycle fatigue.

To counter this problem several authors have written user defined material models in Abaqus in the form of UMATs and VUMATs. One of these models is the CZM VUMAT developed by Oliveira (2018) at ITA. The static and fatigue damage prediction capabilities of this material model have previously been validated on coupon level in the form of double cantilever beam (DCB), four end notch flexure (4-ENF) and mixed mode bending (MMB) simulations [Oliveira 2018]. Using this VUMAT on sub-component level in the research described in this work will aid in the validation of the user defined material model and bring actual use in the industry one step closer. For more background information on how the VUMAT works the reader is referred to appendix B.

3 Methodology

The literature review has provided an overview of the current knowledge on post-buckling in composite stiffened panels. To increase this knowledge the fatigue behavior of co-bonded composite stiffened panels is investigated experimentally and numerically in this research. This chapter explains the experimental procedure. Firstly, the material and specimen preparation are explained in section 3.1. Secondly, the procedure and setup used in the experimental phase of this research are treated in section 3.2.

3.1 Materials and specimen preparation

This section first discusses the materials used in the panels and their corresponding mechanical properties. Subsequently, the ply lay-up of the panels and finally the conditioning of the hygrothermally aged panels are treated.

3.1.1 Materials

The adherent consisted of T800 carbon fiber tape impregnated with 3900-2B epoxy resin produced by Toray. This type of epoxy resin contains thermoplastic polyamide particles which toughens the interlayer domain to improve the impact resistance and slow crack propagation [Toray, Shivakumar *et al.* 2013]. The adhesive EA 9695, produced by Henkel, was used for the bonding procedure. The initial disbond was created using a Teflon^{TM} insert of 0.085 mm thick. The material properties of the tape and adhesive, as provided by the manufacturers Toray and Henkel, are given in table 3.1 and 3.2.

TABLE 3.1 – Mechanical properties of the T800-3900-2B tape as provided by Toray [Toray, Toray 2017]

$\boldsymbol{E_1^T}$ [MPa]	$\boldsymbol{E_1^C}$ [MPa]	$\boldsymbol{E_2^T}$ [MPa]	$\boldsymbol{E_2^C}$ [MPa]	$\boldsymbol{\mu_{12}}$ [MPa]	$\boldsymbol{\nu}$ [-]
$142 \cdot 10^3$	$125 \cdot 10^3$	$7.8 \cdot 10^3$	$9.9 \cdot 10^3$	$3.5 \cdot 10^3$	0.34

$\boldsymbol{S_1^T}$ [MPa]	$\boldsymbol{S_1^C}$ [MPa]	$\boldsymbol{S_2^T}$ [MPa]	$\boldsymbol{S_2^C}$ [MPa]	$\boldsymbol{S_{12}}$ [MPa]	$\boldsymbol{S_{13}}$ [MPa]
2793	1432	36	226.8	63.8	88.1

$\boldsymbol{G_{Ic}^T}$ [N/mm]	$\boldsymbol{G_{Ic}^C}$ [N/mm]	$\boldsymbol{G_{IIc}^T}$ [N/mm]	$\boldsymbol{G_{IIc}^C}$ [N/mm]	$\boldsymbol{T_g}$ [°C]	$\boldsymbol{\rho}$ [ton/mm^3]
165	25	10	2	166-204	$1.58 \cdot 10^{-9}$

Where μ_{12} is the shear modulus in direction 1-2. With 1 being the fiber direction, 2 the in-plane direction perpendicular to the fibers. 3 is the out of plane direction perpendicular to the fibers. S is the tape's strength, with different values existing for the tensile (T) and compression (C) conditions. Finally, ρ is the density and ν Poisson's ratio.

TABLE 3.2 – Mechanical properties of the adhesive as provided by Henkel [Henkel Adhesives]

$\boldsymbol{E}$ [MPa]	$\boldsymbol{S_1}$ [MPa]	$\boldsymbol{S_2 = S_3}$ [MPa]	$\boldsymbol{T_g}$ [°C]	$\boldsymbol{\nu}$ [-]
3100	6.9	31	95-150	0.33

In addition to the material properties provided by the manufacturers, Brito (2017) performed coupon level tests to determine the fracture toughness of the adhesive layer. The B-K parameter, developed by Benzeggagh and Kenane (1996), was used to predict the mixed mode I and II fracture toughness. They state that the fracture toughness for a certain mixed mode ratio can be calculated according to:

$$G_c = G_{Ic} + (G_{IIc} - G_{Ic}) \left(\frac{G_{II}}{G_I + G_{II}} \right)^{\eta} \tag{3.1}$$

Where η is the B-K interpolation parameter and G_I and G_{II} the values for the SERR in mode I and II respectively. The obtained properties are as displayed in table 3.3.

TABLE 3.3 – Mixed mode fracture toughness parameters as obtained from Brito (2017) and Brito et al. (2017)

$\boldsymbol{G_{Ic}}$ [N/mm]	$\boldsymbol{G_{IIc}}$ [N/mm]	$\boldsymbol{\eta}$ [-]
0.235	6.961	8.48

3.1.2 Specimens

Separate skin and stiffeners were produced using hand lay-up by Altec. The stiffener was cured in the autoclave at 177°C for 7 hours, after which the uncured skin and cured stiffener were bonded together using the adhesive with a 100 mm Teflon insert to create an initial disbond. Finally, the panels were again cured in the autoclave for 7 hours at 177°C. The dimensions of the panels were previously given in figures 1.2 and 1.3. The lay-up is given in table 3.4.

TABLE 3.4 – Lay-up of the skin and stiffener. Ply degrees are with respect to the x-axis as displayed in figure 1.2

	Skin	**Stiffener base**	**Stiffener flange**
Number of plies	8	16	24
Lay-up	$[45/90/\text{-}45/0]_s$	$[45/0/\text{-}45/90/45/90/\text{-}45/0]_s$	$[45/0/\text{-}45/90/45/90/\text{-}45/0/0/\text{-}45/90/45]_s$

The panels were named according to standards provided through the INOVA Project with the following structure: 40X-YY ZZZ. Where:

X : Either 1,5 or 7. Referring to co-cured, co-bonded and secondary bonded respectively
YY : Panel number (01-07)
ZZZ : RTA or RTW

As an example, the non-aged co-bonded panel that was tested first is numbered 405-01 RTA.

3.1.3 Conditioning

The co-bonded panels were divided in two groups: room temperature ambient (RTA) and room temperature wet (RTW). The RTA panels were stored in a clean room at ambient conditions until testing. The RTW panels were conditioned in an environmental chamber at 80°C and 90% humidity for 280-396 days. They were weighed regularly until the 190$^{\text{th}}$ day, at which point effective saturation was reached. A 0.02% moisture increase per subsequent weighting moment, as suggested by ASTM D5529 (2014), was used as criterion to determine this. The moisture content of the panels was calculated using ASTM D5229 (2014):

$$\text{Moisture content [\%]} = \frac{W_t - W_0}{W_0} 100\% \tag{3.2}$$

Where W_t is the weight of the panel at time t and W_0 is the weight of the panel before conditioning. A typical moisture absorption curve can be seen in figure 3.1. At the moment of testing all panels contained between 0.61% and 0.64% moisture.

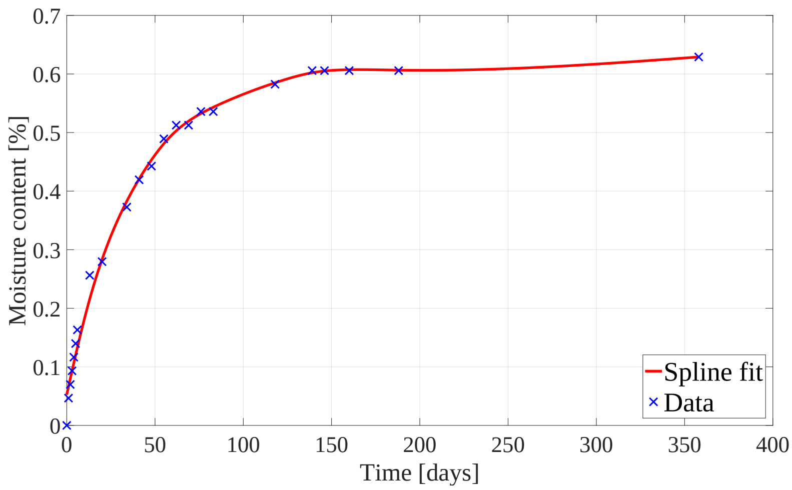

FIGURE 3.1 – Moisture absorption of panel 405-02 RTW

It was chosen to keep all panels in the environmental chamber until the moment of testing. As each panel was tested separately, this resulted in different aging times. However, taking the panels out of the environmental chamber simultaneously could have lead to moisture loss before testing. During the actual experiments the weight of all panels was monitored and none of the panels lost weight in the order of magnitude of 0.1 grams.

3.2 Experimental procedure

As stated in the research outline, the testing phase of the panels consisted of three steps: quasi-static compression tests until failure, cyclic loading and determination of the residual strength. The procedure behind the quasi static compression experiments, also referred to as the ultimate strength tests, is explained in subsection 3.2.1. Step II, the cyclic loading, is treated in subsection 3.2.2. The residual strength experiments are the same as the quasi-static compression tests on the non-cyclic loaded panels, as will already be discussed in subsection 3.2.1 and will therefore not be repeated.

It is important to mention that all panels were pre-cracked before the experiments. This was required because during the second curing process of the panels, in which the adhesive and skin are cured together, part of the adhesive is pressed out from underneath the Teflon^{TM} tape and connects the skin and stiffener at the initially pre-cracked area. To make sure all panels have a fully opened disbonded area with roughly the size of the Teflon tape all panels were subjected to 7 point bending pre-cracking. More background information about the actual pre-cracking procedure can be found in appendix C.1.

3.2.1 Quasi static compression test

The quasi static compression test is explained in three parts. First the boundary conditions to which the panels are subjected are treated. Subsequently, the experimental set-up is discussed. Finally, the procedure used to determine the buckling load is explained.

Boundary conditions

The panels were placed in a testing-rig which subjected them to the boundary conditions as displayed in figure 3.2. The ends were clamped for a total of 40 mm at each side. To simulate this clamping conditions three blocks were fabricated with the inverse shape of the panel. These blocks were then bolted to a platform around the panel to restrict movements. The edges of the panel were constrained from buckling using two blades with a 2.5 mm radius. Additional figures of the parts used to impose the boundary conditions in this study can be found in appendix C.2.

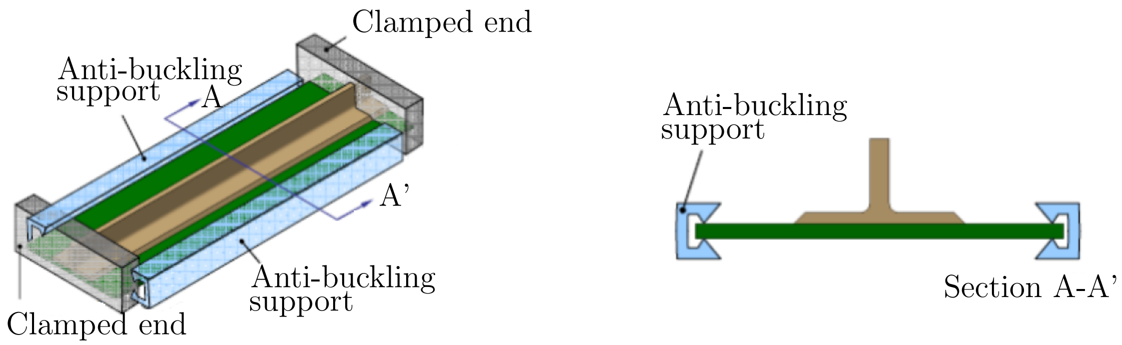

FIGURE 3.2 – Boundary conditions of the panels

The anti-buckling blades were pre-defined in the INOVA project and had as goal to represent a continuous panel with several stiffeners. The validity of this assumption however is not guaranteed, as Bisagni and Vescovini (2011) showed for example that with the right dimensions a single stiffener panel without anti-buckling support is capable of reproducing the buckling behavior of a continuous panel. To make the experiments and simulations as realistic as possible future studies are therefore recommended to use numerical simulations to aid in defining the panel size and boundary conditions.

Experimental set-up

A load controlled Baldwin machine was used to compress the panels until failure. The entire set-up can be seen in figure 3.3 and a close-up of the test-rig in figure 3.4. In addition to the components visible in these figures, the following elements were part of the set-up:

- Baldwin loading machine
- Linear variable differential transformer (LVDT) to determine the out of plane displacement. Placed in the middle of the panel at the backside of the skin.
- 6 strain gauges. 2 strain gauges were placed on the back-side of the skin to determine the buckling load. 2 more were placed at the same location on the front side of the skin to be able to determine the membrane and bending strains. The last two strain gauges were placed back to back on the stiffener. The exact location of the strain gauges can be found in appendix C.2.

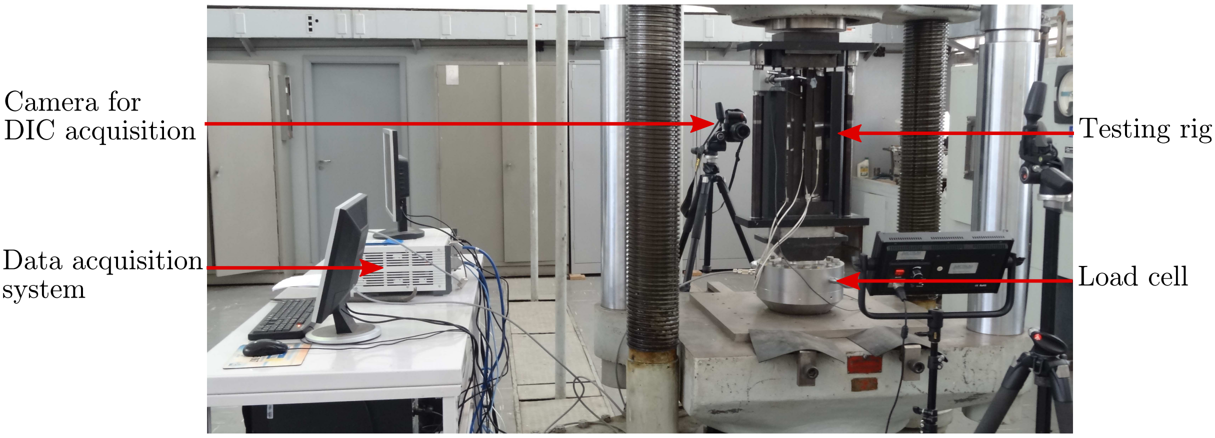

FIGURE 3.3 – Overview of the static testing system

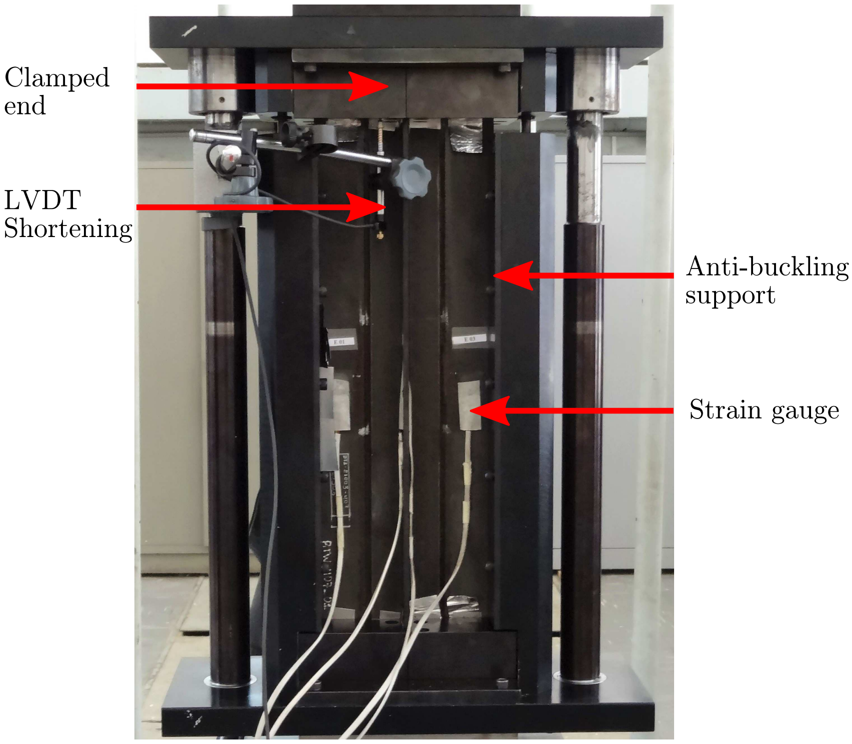

FIGURE 3.4 – Close up of the test-rig

As strain gauges, micro-measurement general purpose strain gauges produced by VPG with a resistance of 350±0.3%Ω and a gauge factor of 2.120±0.5% were used. They were placed in a quarter Wheatstone bridge configuration measuring the sum of the axial and bending strain. As all strain gauges were placed back to back with another strain gauge this data could also be converted into membrane and bending strains.

During several static experiments, instead of using a LVDT to measure the out of plane displacement, the 2D displacement field was monitored throughout the test using a digital image correlation (DIC) system. An overview of this DIC system is displayed in figure 3.5. Pictures of the speckle pattern on the back side of the panel were taken manually at every load increase of -10 kN and subsequently post-processed using ncorr V1.2 in Matlab to obtain the displacement field.

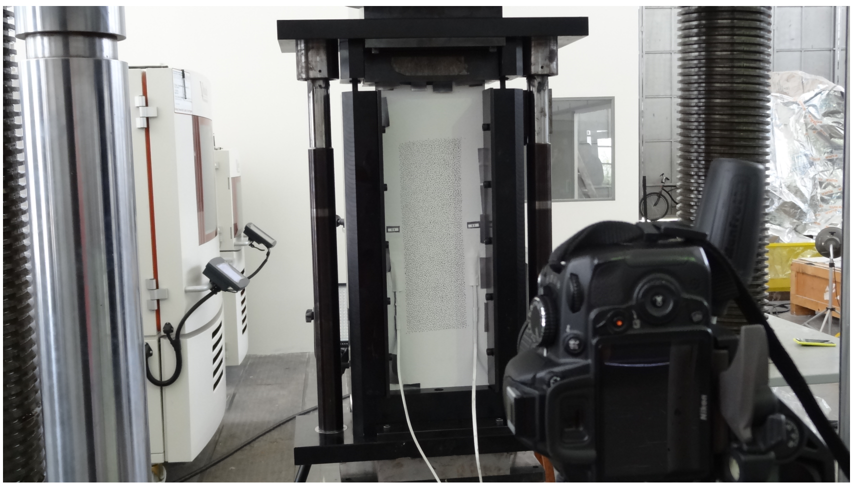

FIGURE 3.5 – DIC system set-up

Determination of the buckling load

The strain gauges on the back-side of the skin were used to obtain the buckling load according to the strain reversal method. This method is frequently used in literature [Dobrowski *et al.* 1944, Romeo e Frulla 1997, de Paula Guedes Villani *et al.* 2015] and is based on the work of NACA in the mid forties [Singer *et al.* 1998, Hu *et al.* 1946]. It defines the buckling load as the point at which the extreme-fiber strain on the convex side of the buckle, ϵ_2 in figure 3.6, starts decreasing [Hu *et al.* 1946, Jones 2006]. Generally it results in more conservative outcomes than many of the other methods currently available in the open literature [Singer *et al.* 1998]. The tool used to extract this point from the strain gauge data was developed by Hottentot Cederløf (2018).

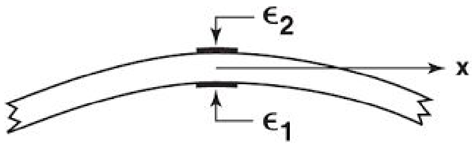

FIGURE 3.6 – Strain definitions in the strain reversal method [Jones 2006]

3.2.2 Cyclic loading

To explain the experimental procedure behind the cyclic loading this subsection first treats the experimental set-up. Thereafter the procedure to determine the size of the disbond during the cyclic loading is discussed. At set intervals throughout the experiment the stiffness of the panels was also monitored, this is treated last.

Experimental set-up

3 RTA and 5 RTW panels were subjected to 300,000 cycles of compression loading. This amount was chosen to comply with the earlier tests performed on co-cured panels, from which it was also determined that the disbond growth after 300,000 cycles was limited. A frequency of 5Hz was applied, for which the material did not heat up, as was measured using an infra red camera, and the test set-up remained relatively free of vibrations. Originally it was planned to test only 3 RTA and 3 RTW panel. However, 2 additional RTW panels were tested because the outcome of the first 3 was different from the expectations at that moment. The load cycles were roughly between -4.7 kN and -47.5 kN, resulting in a load ratio (R) of 0.1. This amplitude was chosen in such a way that it was just below the maximum load of -50 kN of the set-up. It had proven suitable for earlier tests with co-cured panels. An overview of the test set-up can be seen in figure 3.7.

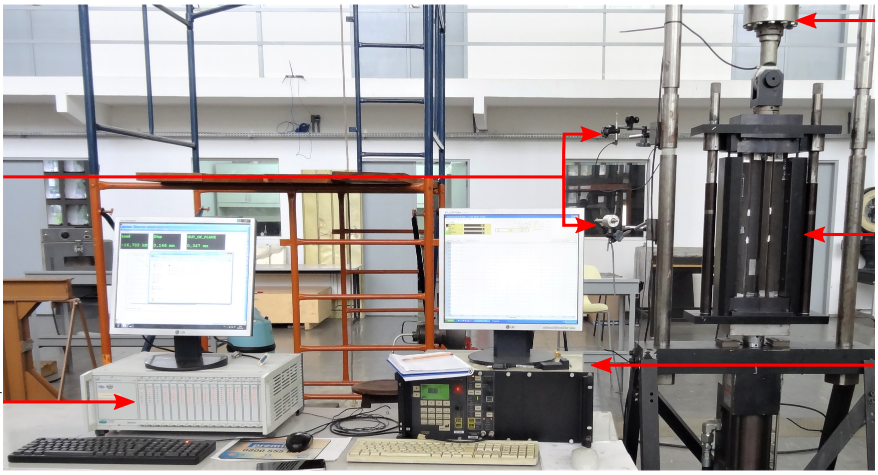

FIGURE 3.7 – Set-up of the fatigue experiments

Disbond size

Based on the measured disbond growth during the cyclic loading of the aforementioned co-cured panels, it was concluded that disbond growth during the initial cycles was likely to be bigger than the growth during the final fatigue cycles. Therefore, the measurements were more closely spaced in the beginning of the testing than at the end. Resulting in the following cycles after which the disbond length was measured: 0, 1, 500, 5000, 10,000, 30,000, 50,000, 100,000, 150,000, 200,000 and 300,000. The measuring was performed with ultra-sound using an Isonic 2006 produced by Sonotron NDT. As only the disbond size was relevant just the areas near the disbond edges were scanned. Everything in between the edges was assumed to be disbonded because it buckled and everything outside was assumed to be intact.

The panel had to be taken out of the set-up and brought to the Isonic 2006 to be able to carry out the ultra-sound tests. To minimize repeatability errors the panels were kept inside the ends providing clamped boundary conditions. The blades providing the anti-buckling support did have to be re-tied after every measurement. The same procedure, with one operator pressing the blade in place and one tying the bolts, was used throughout the entire testing phase.

According to the Isonic 2006 user manual a scanning accuracy of 1 mm can be achieved. However, during the scanning of the panels it was noticed that sometimes probe location shifted when it was close to the antennas, which is where also the crack fronts were located. This caused the accuracy of the probe to be roughly 2 mm per side.

After scanning, the results were post-processed to obtain the disbond length and disbond area. Both parameters only considered the disbonded part underneath the stiffener, the adhesive present on the edges of the stiffener typically cracked in a different way and was not considered relevant. A more thorough explanation of how the disbond length and area were determined based on the outcome of the c-scan can be found in appendix C.3.

Stiffness

To get a sense of the overall damage state of the panel the overall stiffness was determined by constructing a load-shortening curve up to -47.5 kN at every other disbond length measurement point. Thus, during the 1^{st} cycle and after 500, 10,000, 50,000, 150,000 and 300,000 cycles. Stiffness losses can be an indication of intralaminar or translaminar damage, both of which are not picked up by the c-scan. During the load-shortening measurement of the RTW panels the out of plane displacement was also measured using a second LVDT. This was done in the middle on the backside of the skin, where the out of plane displacement was expected to be at its maximum.

For clarity, all measurements are summarized in table 3.5.

TABLE 3.5 – Measurements of the panels at set intervals

Number of cycles	Disbond length	Shortening	Out of plane displacement
0	RTA & RTW		
1	RTA & RTW	RTA & RTW	RTW
500	RTA & RTW	RTA & RTW	RTW
5000	RTA & RTW		
10,000	RTA & RTW	RTA & RTW	RTW
30,000	RTA & RTW		
50,000	RTA & RTW	RTA & RTW	RTW
100,000	RTA & RTW		
150,000	RTA & RTW	RTA & RTW	RTW
200,000	RTA & RTW		
300,000	RTA & RTW	RTA & RTW	RTW

4 Experimental results

The experiments described in chapter 3 were divided in three steps: quasi-static compression tests until failure on pristine reference panels (ultimate strength), cyclic loading and quasi-static compression tests until failure on the cyclically loaded panels (residual strength). The results of these experiments are treated in that same order in the subsequent sections.

4.1 Quasi static compression of the reference panels

Panels 405-01 RTA and 405-01 RTW were tested in compression up to final failure using the methodology described in subsection 3.2.1. Both panels were monitored using 2D DIC throughout the experiment. In this section the buckling and failure behavior are presented.

4.1.1 Buckling

The strains and corresponding buckling loads for both the RTA and RTW panel can be seen in figure 4.1. The buckling load of strain gauge 2 is different from 4 because the buckling shape is tilted diagonally due to the presence of the 45° layers on the outside of the skin lay-up. This diagonal shape can be distinguished in the results of the DIC analysis presented in figure 4.2. Combining this knowledge with the locations of the strain gauges suggests that strain gauge 4 is expected to buckle first. This effect is reversed for the RTW panel however. The fact that in all residual strength tests that will be presented in section 4.3 strain gauge 4 did indeed buckle first indicates that strain gauge 2 of the RTW panel is likely unreliable. Possibly it was placed too far upward. If strain gauge 2 of the RTW panel is omitted, both panels have almost identical buckling loads.

The buckling shape that is observed both visually and through the DIC analysis is a single half wave. Single half wave buckling shapes typically result in more dominant mode I fracture and are therefore critical with respect to disbond growth, as was concluded in subsection 2.3.2. The similarities in both the buckling load and the buckling mode between the RTA and RTW panel are a first indication that the skin and stiffener did not degrade significantly due to the hygrothermal aging.

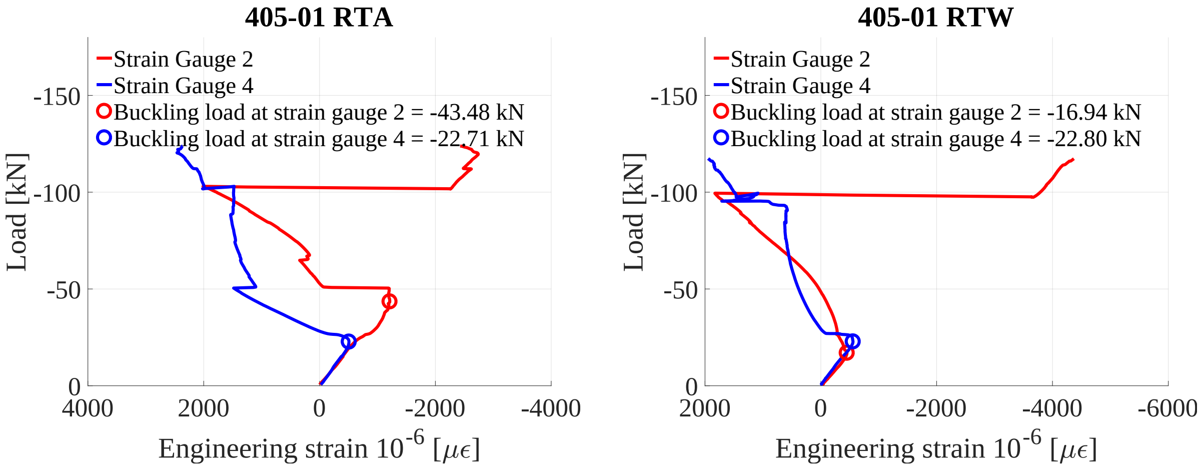

(a) (b)

FIGURE 4.1 – Strain gauges on the back-side of the skin during ultimate load compression test

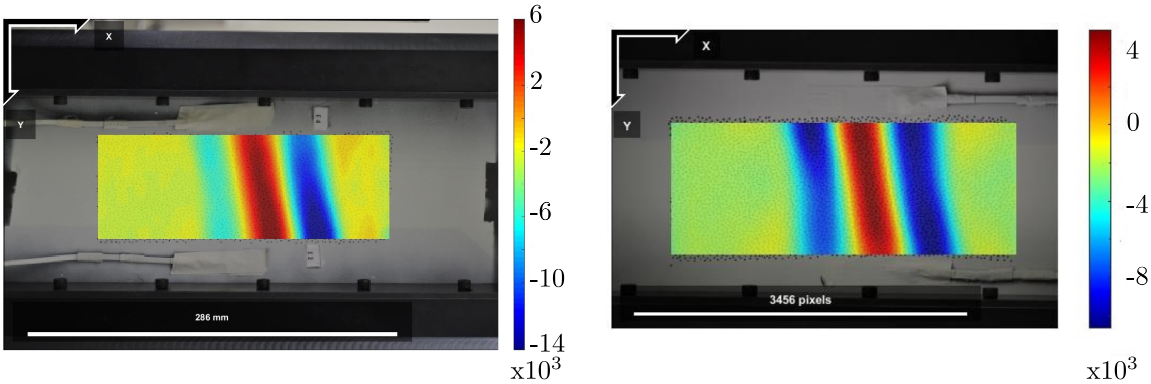

(a) 405-01 RTA* (b) 405-01 RTW*

FIGURE 4.2 – Strain field ($\mu\epsilon_{xx}$) at a load of -50 kN
**Legend scales are incorrect due to out of plane displacement in combination with the 2D DIC setup*

4.1.2 Failure behavior

Figure 4.3 displays the load-shortening curves for both panels up to failure. No significant effects of degradation due to hygrothermal aging can be distinguished from these curves alone. The stiffness of the panels was determined based on the load and displacement at disbond growth onset, which can be distinguished from the load drop at roughly -100 kN. The 7% difference seems quite large, but the residual load tests performed in step III of the experimental phase showed that the load-shortening curves were not a reliable measure for the stiffness. The membrane strains in the stiffener produced more reliable results, however strain gauge 5 of panel 405-01 RTA malfunctioned and thus this measure was not available. Therefore, no conclusions should be derived from the stiffness difference between the RTA and RTW panel.

In subsection 2.2.4 it was mentioned that the strength of the panels was expected to be affected by the hygrothermal aging through degradation of the matrix and adhesive.

Although the strength of the panel did indeed decrease by 5%, this effect can not directly confirmed, as only two panels were tested during this phase. Therefore, one has to be careful with drawing any conclusions based on this outcome.

The stiffness of both panels remained largely unaffected by disbond growth during the experiment. This can be distinguished from the fact that the slope of the curves remain relatively constant after the load drop at roughly -100 kN. The fact that the stiffness does not change after disbond growth is in line with subsection 2.3.2, in which it was stated that the disbond size has limited influence on the stiffness of stiffened panels.

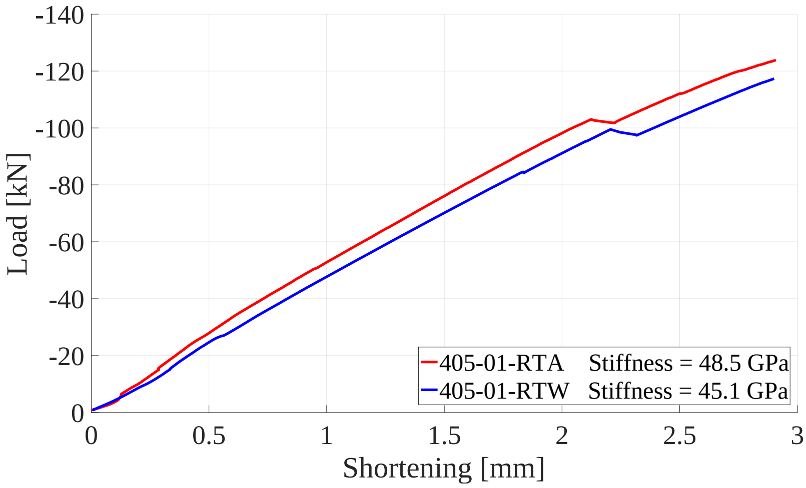

FIGURE 4.3 – Load shortening curve of 405-01 RTA & RTW

Interestingly, even though the buckling mode shape, load at which the disbond grew and the ultimate strength were quite similar for both panels, the failure modes were not. The RTA panel after failure can be seen in figure 4.4 and the RTW panel in figure 4.5. It can be distinguished that the RTA panel failed locally in the skin and stiffener with only a small amount of disbond growth. The RTW panel on the other hand failed due to almost complete delamination between the skin and stiffener.

Although one might expect that this difference is an indication of degradation of the adhesive, the residual strength tests in step III of the experimental phase, which will be described in section 4.3, showed that this was likely not the case. In these experiments both RTA and RTW panels exhibited this type of failure. Rather, the difference between failure modes might exist due to a difference in tightness of the clamped ends. All panels that failed through delamination showed signs of crushed stiffeners, indicating that the clamping boundary conditions were not as tight as they should be. An example of such a crushed end can be seen in figure 4.6, which was taken from one of the residual load tests. Shims were used to improve the tightness of the clamped ends. Although this indeed increased the tightness, it did not mitigate the problem completely.

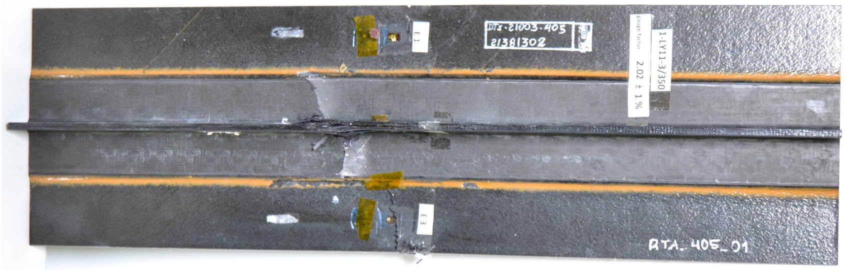

FIGURE 4.4 – Post-failure 405-01 RTA

FIGURE 4.5 – Post-failure 405-01 RTW

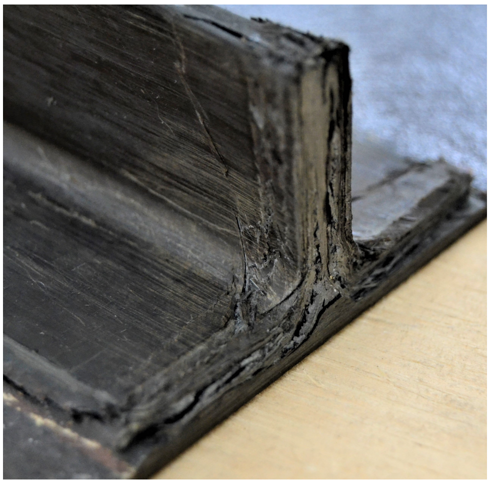

FIGURE 4.6 – Crushed end of 405-03 RTW after the residual load test of phase III

4.2 Post-buckling fatigue

At set intervals during the cyclic loading, the size of the disbond and the stiffness were monitored. First the growth of the disbond is treated in subsection 4.2.1. Subsequently the influence of the cyclic loading on the stiffness of the panel is discussed in subsection 4.2.2.

4.2.1 Disbond growth

Figures 4.7 and 4.8 show the average growth of the disbond length and area throughout the cyclic loading of the RTA and RTW panels. To get these curves the experimental data was averaged and only the data from the first cycle and onward were considered. This was done because several panels were not fully opened after the pre-cracking. These panels opened during the first load cycle, which caused large deviations in growth within this cycle. The experimental data was fitted with a power curve, as this gave the fit with the lowest normalized root mean square error (NRMSE).

The first interesting fact that can be distinguished from the graphs is that the disbond growth of both the RTA and RTW panels slowed down as the amount of cycles increased. If this is not immediately obvious from figures 4.7 and 4.8 due to the log-scale used on the x-axes, it can be clearly seen when the disbond growth per cycle is plotted against the amount of cycles (figure 4.9).

The declining disbond growth speed is likely related to a decrease of the stress concentrations in the corners of the bonded area. These stress concentrations are provoked by the diagonal buckling shape. However, as the disbond grows the disbonded area starts to match better with the buckling shape and thus the stress concentrations decrease. An example of the diagonal growth of the disbond can be seen in figure 4.10. Interestingly, the RTW panels showed more profound diagonal disbond growth than the RTA panels. This can be distinguished by the fact that the area growth of the RTW panels stays behind in comparison to its length growth and the area growth of RTA.

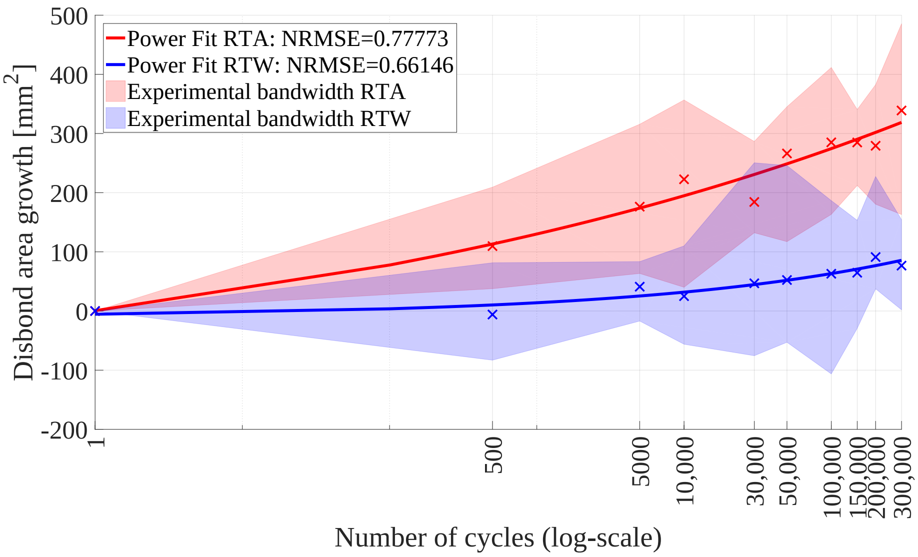

FIGURE 4.7 – Disbond area growth

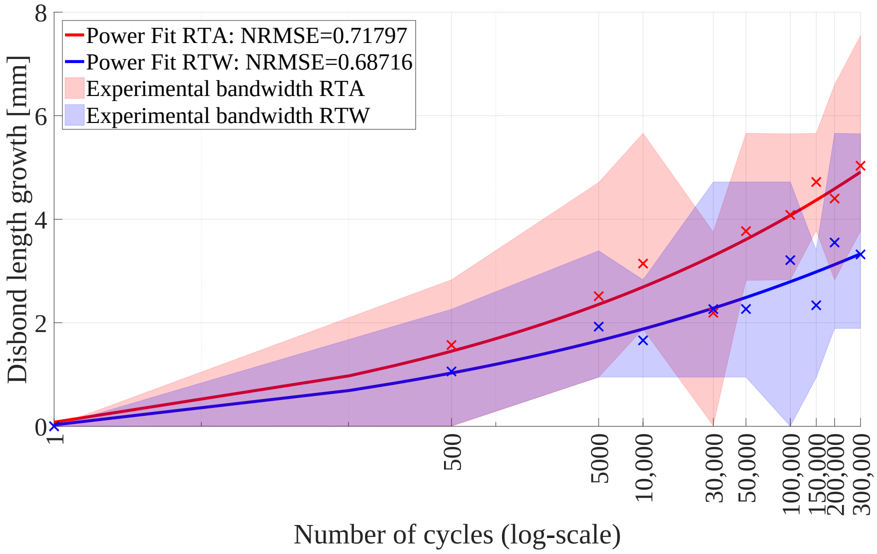

FIGURE 4.8 – Disbond length growth

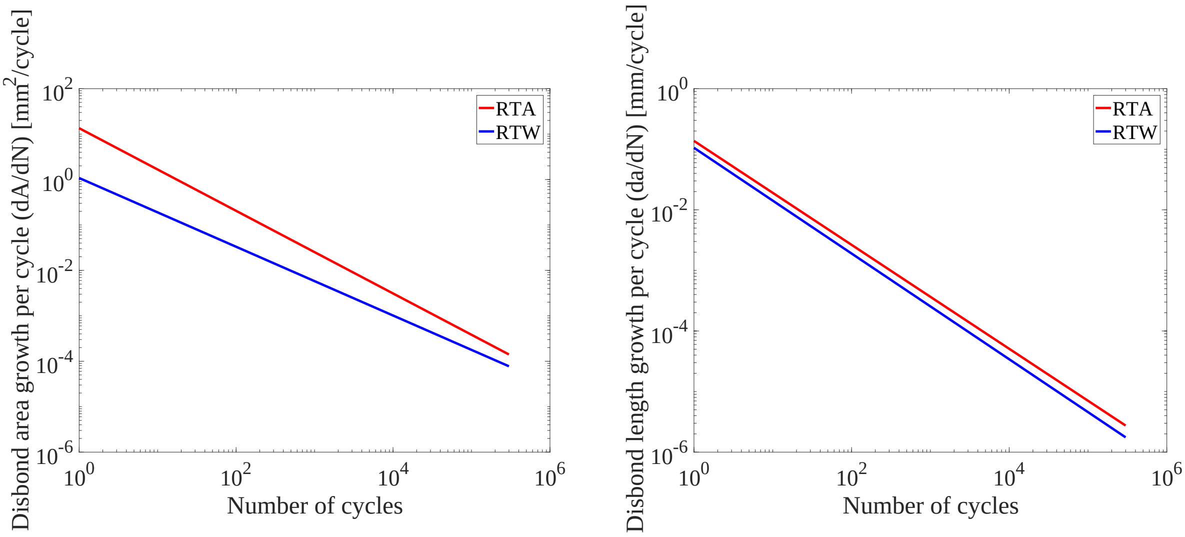

(a) Average growth rate disbond area (b) Average growth rate disbond length

FIGURE 4.9 – Average growth rate RTA and RTW panels

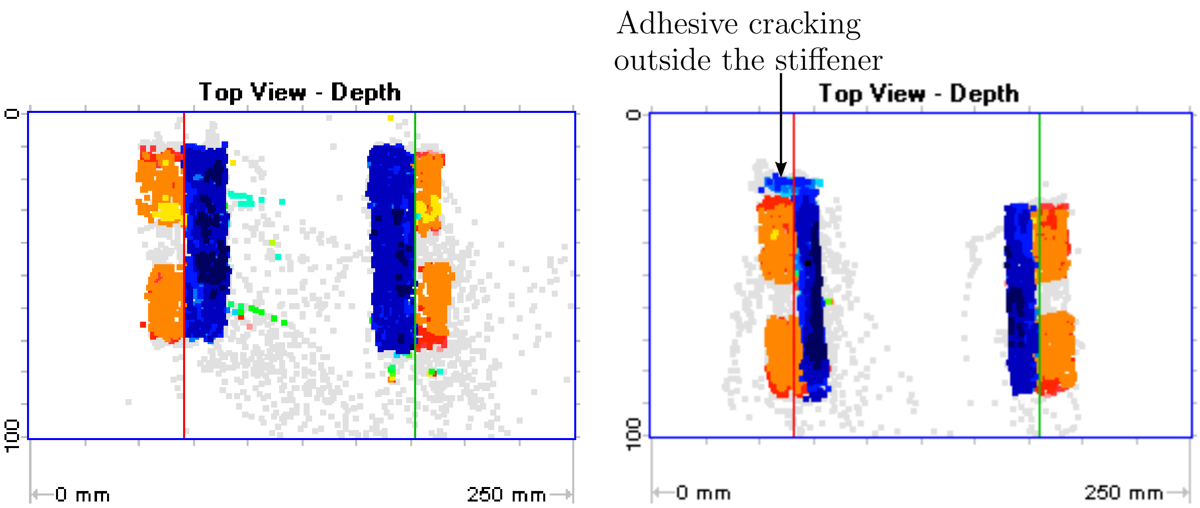

(a) N=1 (b) N=300,000

FIGURE 4.10 – Disbonded area (blue) 405-02 RTA after 1 cycle and 300,000 cycles

Based on the literature review it was not entirely clear what the effect of the hygrothermal aging would be on the disbond growth during the cyclic loading. However, a decrease in disbond growth after hygrothermal aging was not expected. Three factors that potentially contributed to the lower amount of growth were identified:

- Stress relaxation in the adhesive resulting in an increase of the propagation fracture toughness
- Crack blunting due to the presence of moisture
- The average disbonded area of the RTW panels being 4% larger larger than the RTA panels after pre-cracking

In section 2.2 stress relaxation was already mentioned as a potential consequence of hygrothermal aging. However, Halliday et al. (2000) only reported an increase in the mode I fracture toughness due to stress relaxation after 78 days at the crack initiation point. No such increase was present in their study after 25 mm of crack growth.

An important difference between the coupon level study performed by Halliday et al. (2000) and the sub-component level of this research is the specimen size. Bigger specimens have relatively less surface area and larger distances for the moisture to cover, thus slowing down moisture penetration. This, in combination with the fact that the temperature during conditioning remained below the T_g of the adhesive, might have caused the propagation fracture toughness to increase even after prolonged exposure. Unfortunately, no studies were found reporting on the influence of hygrothermal aging on the mode II fracture toughness tested at RTW conditions. Hence, the proposed hypothesis that the propagation fracture toughness increased due to stress relaxation can not be verified based on the literature.

The second factor that can play a role is the plasticization of the adhesive due to moisture, which causes blunter crack tips [Packham 2005]. This in turn leads to lower stress concentrations at the crack tip and can therefore result in a lower amount of fatigue crack growth. As discussed in subsection 2.2.1, Abanilla et al. (2006) already reported that this phenomenon could lead to a decrease in interlaminar crack growth in CFRP.

The third factor is the difference in average disbond size between RTA and RTW panels after pre-cracking. Although the pre-cracking procedure for the RTA and RTW panels was the same, the disbonded area for the RTW panels ended up being roughly 4% larger than the disbond of the RTA panels after pre-cracking (6622 mm^2 and 6360 mm^2 respectively). The influence of this difference on the growth during fatigue will be investigated using the numerical model presented in chapter 5.

The difference in disbond size after pre-cracking was likely caused by a combination of a decreased fracture toughness at the crack initiation point of the RTW panels and the fact that the pre-cracking of the RTA and RTW panels was performed by different operators. An indicator of the decreased fracture toughness at crack initiation is that the load required to initiate disbond growth during pre-cracking was significantly lower for the RTW than the RTA panels, as displayed in figure 4.11.

The fact that the initiation fracture toughness decreased, but the propagation fracture toughness potentially increased can be explained by how they are exposed to the humid environment. As was mentioned in subsection 2.2.3 the original crack tip is exposed to 4 edges, of which 2 directly. Further down the crack path however the exposure reduces to 2 indirect edges, making it harder for the moisture to penetrate. Moreover, Halliday et al. (2000) already showed that the fracture toughness at the crack initiation point was affected differently by hygrothermal aging than the propagation fracture toughness.

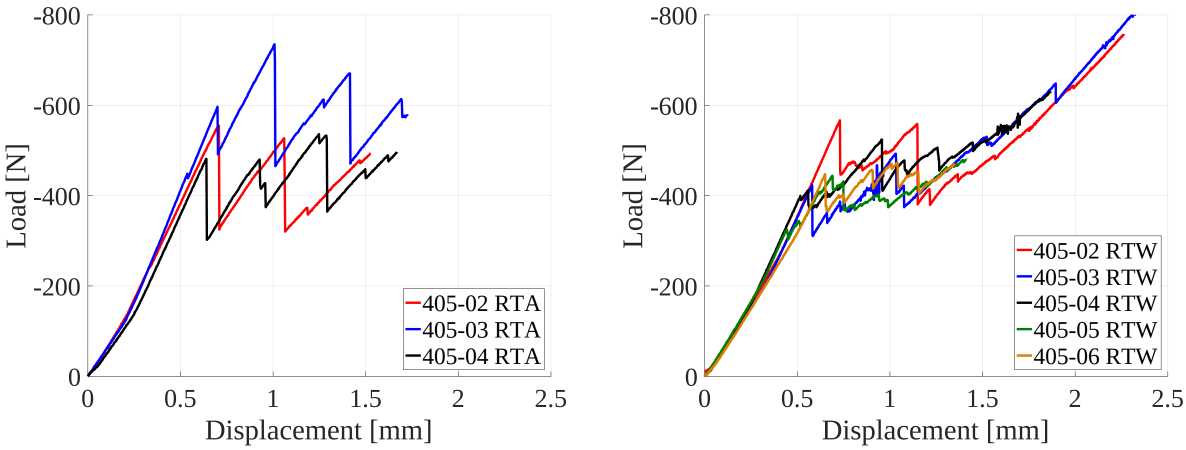

(a) Pre-cracking RTA panels (b) Pre-cracking RTW panels

FIGURE 4.11 – Average growth rate RTA and RTW panels

Lastly, a note has to be made about the large and jagged bandwidth of the experimental values. This may have been caused by the relatively inaccurate c-scanning device. As discussed in subsection 3.2.2, the location of the disbond could only be measured up to an accuracy of ±2 mm. Using average values can mitigate this problem, but the results are likely still influenced by this phenomenon. It is advised to use a higher accuracy machine or force a larger amount of crack growth such that the inaccuracies become less significant in future experiments. More growth can for example be achieved by not using the anti-buckling support blades or increasing the maximum cyclic load.

In addition to measuring the disbond length using the c-scanning device, the out of plane displacement was measured throughout the testing phase for all RTW panels. The hypothesis being that as the disbond grows the out of plane displacement of the skin after buckling increases. This was confirmed by the fact that for each panel, at every subsequent measurement, a larger out of plane displacement was measured at the maximum load of -47.5 kN. An example of which can be seen in figure 4.12.

Interestingly, in all cases the out of plane displacement grew more substantially than the crack. The average out of plane displacement of the RTW panels grew by 13% versus a disbond length growth of only 3%. Based on the data currently available no direct relation could be constructed between the out of plane displacement and the total disbonded length or area.

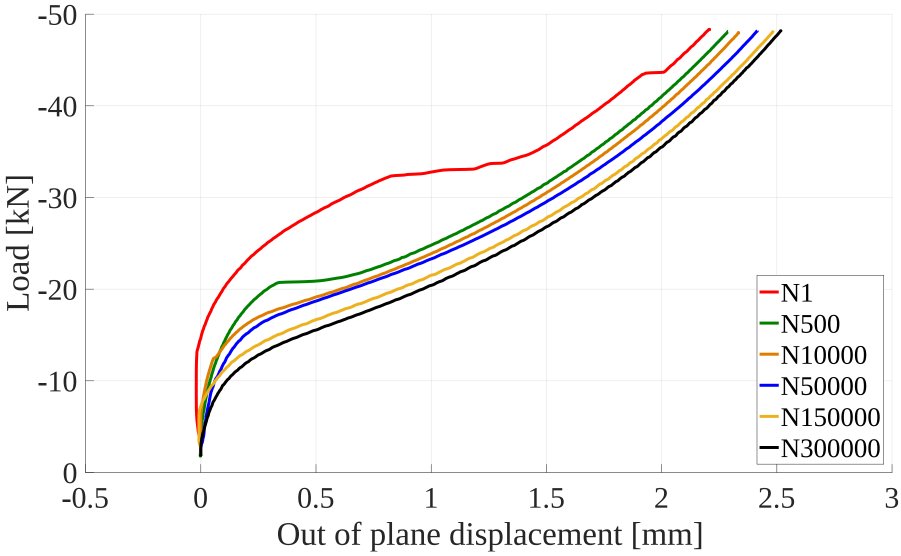

FIGURE 4.12 – Typical load vs out of plane displacement curve as constructed throughout the fatigue testing phase (405-03 RTW)

4.2.2 Stiffness

Typical examples of load-shortening curves constructed at set points throughout the cyclic loading can be seen in figure 4.13. Several measurement points were omitted for clarity purposes. Similar to the results obtained by Abramovich and Weller (2010), discussed in subsection 2.3.3, none of the panels showed any sign of stiffness loss due to the cyclic loading.

The fact that no stiffness degradation took place throughout the cyclic loading further strengthens the statement made in subsection 4.1.2 that the disbond size has limited influence on the stiffness of the panel. Moreover, it solidifies the assumption that the numerical model simulating the post-buckling fatigue should focus on the disbond growth, as was proposed in section 2.4.

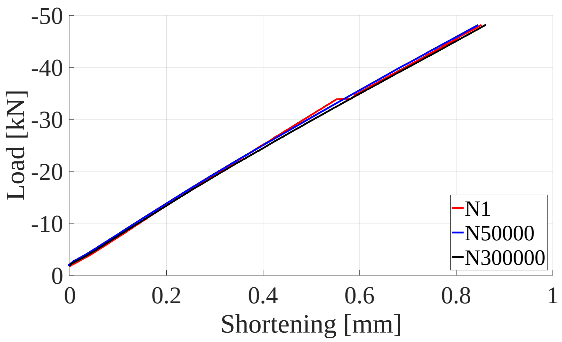

(a) 405-02 RTA

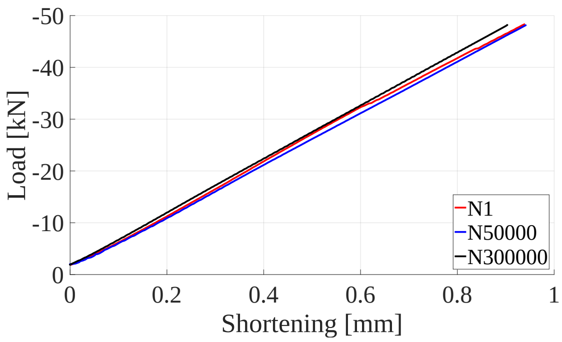

(b) 405-03 RTW

FIGURE 4.13 – Typical load-shortening curves as constructed throughout the fatigue testing phase

4.3 Residual strength

During the last step of the experimental phase the residual strength of the cyclically loaded panels was determined. Subsection 4.3.1 first treats the buckling behavior of the panels during the experiments. Subsequently, the failure behavior is discussed in subsection 4.3.2.

Unfortunately, the LVDT measuring the shortening of the panels malfunctioned during several experiments. Possibly this was related to calibration issues. To mitigate this problem the membrane strain in the stiffeners was used to compare the stiffness of the panels instead of the shortening.

4.3.1 Buckling

Table 4.1 shows that the average buckling loads of the RTW panels did not differ significantly from the RTA panels. The difference with the reference panels on the other hand is remarkable. This change was not caused by a lower overall stiffness, as subsection 4.2.2 already demonstrated that the stiffness of the panels was unaffected by the cyclic loading for at least the first -47.5 kN.

Possibly the difference in disbond length between the reference panels and the cyclically loaded panels played a role in decreasing the buckling load. Although this is not expected to be of such a big influence, as the disbond size of the RTA and RTW panels was also different but did not influence the buckling load. Additionally, within the RTA panels and RTW panels the buckling loads varied as well, but no correlation could be distinguished between the buckling load and the disbond length there either. A linear buckling analysis in chapter 5 will be used to shed more light on the influence of the disbond size on the buckling load.

Another possible scenario is that the repeated buckling and corresponding out of plane displacement caused the out of plane bending stiffness of the skin to decrease. Van Paepegem and Degrieck (2001) have shown that repeated bending can decrease the bending stiffness of GFRP specimens significantly. They registered a bending stiffness decrease of 50% for unidirectional specimens and 15% for 45°specimens after 300.000 load cycles. It is not possible to say with certainty whether or not this occurred in the panels as no observable damage was present. However, this is generally very difficult with fatigue damage due to the presence of micro cracks.

If a stiffness decrease as a consequence of the cyclic loading did indeed occur it would also explain why no relation could be found between the disbond length and the out of plane displacement in subsection 4.2.1, as a lower stiffness in the skin likely results in a larger out of plane displacement. This would make the out of plane displacement dependent on both the fatigue damage in the skin and the disbond length.

As Abaqus has no numerical tool readily available to simulate intralaminar high cycle fatigue damage in CFRP it is not possible to determine the amount of damage numerically. Therefore, a linear buckling analysis with lower stiffness properties in the skin around the disbonded area will be performed in chapter 5 to strengthen or debunk the hypothesis that local damage in the skin around the disbonded area (partially) caused the buckling load to decrease after the cyclic loading.

TABLE 4.1 – Buckling loads and disbond length of the panels at onset of quasi static compression test

	Average disbond length [mm]	**Average buckling load (SG4)** [kN]
RTA panels	112.6	-16.3
RTW panels	115.9	-16.4
Reference panels	107.6	-22.8

4.3.2 Failure behavior

The membrane strain in the stiffeners during the residual strength tests can be seen in figure 4.14. From comparing figure 4.14 a and b it can be seen that the hygrothermal aging did not significantly affect the average failure load, which was -119 kN for the RTA panels versus -117.3 kN for the RTW panels. Moreover, no significant influence of the hygrothermal aging on the stiffness of the panels can be distinguished either, which is demonstrated more clearly in figure 4.15. This indicates that the 5% stiffness reduction after hygorthermal aging of the reference panel might have actually been caused by inaccuracies in the experimental set-up, rather than the hygrothermal aging. Subsection 2.2.4 already indicated that the fiber related properties were not expected to change because they are not affected by moisture and the temperature remained far below the critical temperatures for carbon fibers. This likely played an important role in keeping the stiffness constant.

The failure modes of the panels were similar to the ones of the reference panels described in section 4.1 and randomly distributed among the RTA and RTW panels. Hence, rendering any correlation between failure mode and aging condition impossible. Based on the information presented here it can be concluded that the hygrothermal aging did not influence the quasi-static failure behavior of the panels after the cyclic loading.

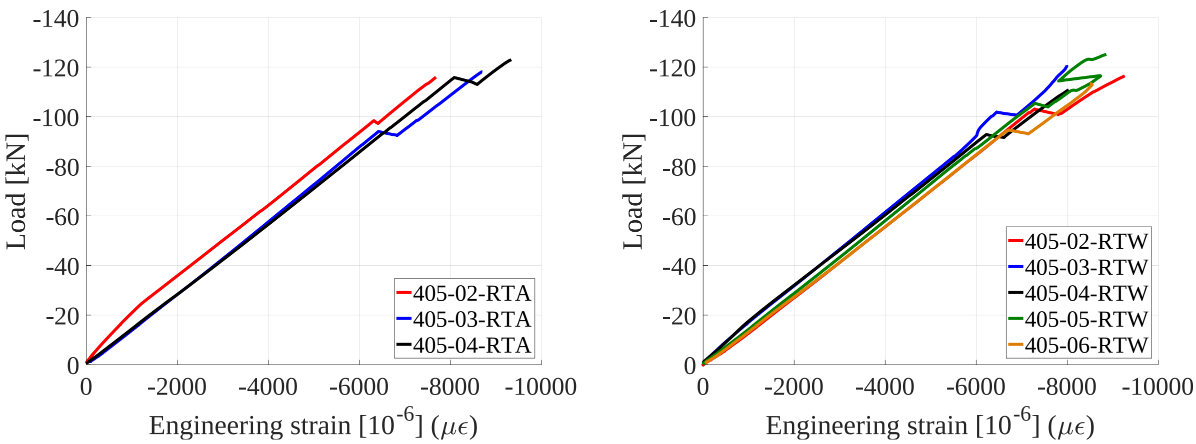

(a) RTA panels (b) RTW panels

FIGURE 4.14 – Membrane strain in the stiffener as a function of the load

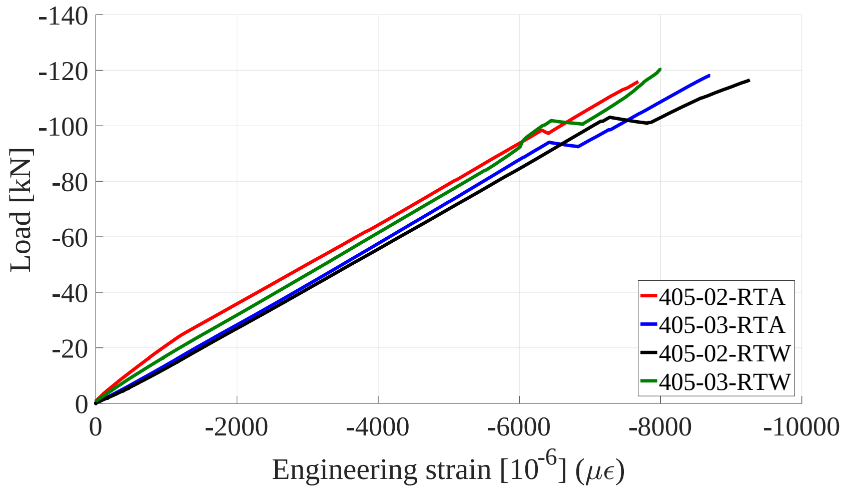

FIGURE 4.15 – Membrane strain in the stiffener for two RTA and two RTW panels

A comparison of the load-shortening curves of the reference panels and two typical cyclically loaded panels, depicted in figure 4.16, shows that also the cyclic loading had no influence on the strength and stiffness of the panels. This also shows that if any intralaminar or translaminar damage occurred during the cyclic loading it had no influence on the overall stiffness strength of the panel.

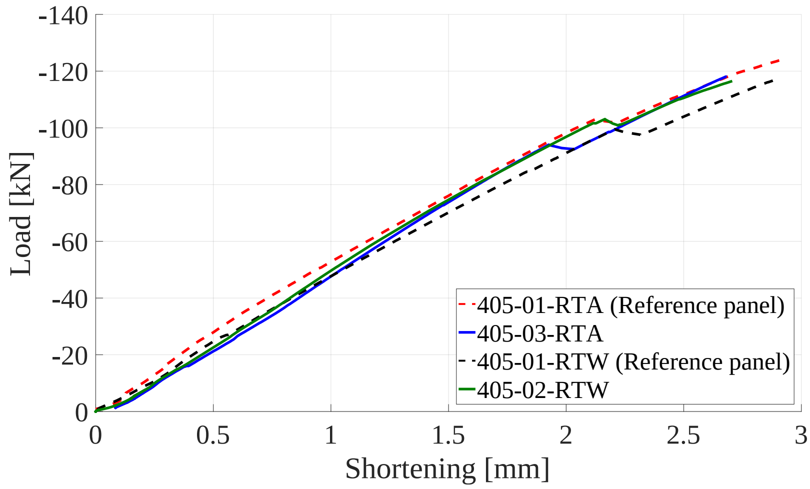

FIGURE 4.16 – Typical load shortening curves of the quasi-static residual strength tests

4.4 Concluding remarks

The goal of the experimental phase was to answer the first research sub-question that was stated in section 1.4. For clarity this sub-question is repeated here:

1. <u>What is the influence of cyclic post-buckling loading on co-bonded composite stiffened panels with a disbond and how does hygrothermal aging affect this?</u>

The cyclic compression loading caused the disbond to grow. The disbond grew diagonally because of the diagonal buckling shape, caused by the presence of a 45° layer on the outside of the skin. As the original pre-crack was approximately straight this lead to stress concentrations in the corners. These stress concentrations decreased as the disbond area started to match the buckling shape, which likely caused the decrease in crack growth speed during the fatigue experiments.

The fatigue damage did not influence the overall stiffness of the panels. Additionally, all panels were capable of taking 300,000 cycles in the compressive post-buckling regime without any noticeable effect on the strength, stiffness or failure behavior of the panels. This expands the knowledge gained by Davila and Bisagni (2017) and Abramovich and Weller (2010) who also remarked about the durability of composite stiffened panels under cyclic post-buckling loading. However, they only tested up to roughly 25,000 and 64,000 post-buckling cycles.

One unanticipated effect of the cyclic loading was that the buckling load decreased 28.5% in comparison to the reference panels. Two factors that could potentially have caused this are the difference in disbond length between the cyclically loaded panels and the reference panels and a decrease in out of plane bending stiffness of the skin at the location of the disbond due to the repeated out of plane bending.

Overall the hygrothermal aging had a relatively small effect on the behavior of the panels during the experiments. Based on the literature study presented in section 2.2 it was expected that the mechanical properties of the matrix and adhesive would degrade, which could potentially lead to a decrease in the strength of the panel. The experiments showed however that neither the strength, stiffness, nor the buckling load of the panels changed due to the aging process.

The fracture toughness of the adhesive did change as a consequence of the hygrothermal aging. The initiation fracture toughness decreased, as could be distinguished from the fact that debonding during pre-cracking occurred at a lower load for those panels. The total disbond growth during the cyclic loading on the other hand was lower for the RTW panels. This indicates that the propagation fracture toughness might have actually increased, instead of decreased. Other possible causes of the decrease in disbond growth are crack blunting due to the presence of moisture in the adhesive and the fact that the RTA and RTW panels had different disbond lengths at the experiment onset. The influence of the latter will be further investigated with the numerical model in chapter 5.

To further investigate the influence of environmental aging on bonded joints in composite stiffened panels it would be interesting to investigate the performance of these joints at cryogenic temperatures. Cryogenic temperatures are known to make adhesives more brittle, which could give a completely different result to the presence of moisture that plasticizes the adhesive [Adams *et al.* 1992]. To the best of the author's knowledge, no study investigating the influence of cryogenic temperatures on the fatigue behavior of bonded composite joints on sub-component level is currently available in the open literature.

5 Numerical model

The numerical simulations were carried out using Abaqus 6.14-1 finite element software. To validate the model proposed by Oliveira (2018) for the current material combination, the quasi-static experiments on coupon level performed by Brito (2017), previously mentioned in subsection 2.1.1, were simulated. These simulations, modeling a quasi static double cantilever beam, four end notch flexure and one mixed mode bending experiment, showed satisfactory results when compared to the experiments. Details on these models and their results can be found in Appendix E.

Four different simulations were performed to increase the understanding of the full range of experiments carried out in this research. The models behind these simulations are treated in section 5.1. The first simulation that was executed was a linear buckling analysis used to gain insight in the buckling load of the panels. The results of this simulation are discussed in section 5.2. Subsequently, the numerical results of the quasi static compression test performed on the reference RTA panel are treated in section 5.3. The results of the cyclic loading and residual strength simulations are given in sections 5.4 and 5.5. Thereafter, a sensitivity analysis of the interface strength is discussed in section 5.6. Finally, the most important conclusions are repeated in section 5.7.

5.1 Numerical models

Even though the goal of each simulation described in sections 5.2 - 5.6 is different, fundamentally the numerical models behind these simulations were very similar. Parameters such as boundary conditions, geometry and element type did not change from model to model. This constant basis is explained in subsection 5.1.1. The specific parts for each simulation are treated in subsections 5.1.2 - 5.1.4.

5.1.1 Numerical model basis

An overview of the geometry of the panel can be seen in figure 5.1. Only the non-clamped part of the panel was modelled to save computational costs. As each side was clamped for 40 mm this resulted in a free length of 420 mm. Different disbond lengths were used for the various simulations.

A 0.0192 mm thick layer was used to represent the adhesive interface, which equals 10% of the laminates' ply-thickness. This thickness had already been used in the coupon simulations described in chapter E and proved satisfactory. The adhesive was connected to the stiffener and skin using tie constraints. The Abaqus user manual suggests to take the stiffest surface as master and most compliant surface as slave [ABAQUS Inc. 2014]. Thus resulting in skin and stiffener master surfaces and cohesive slave surfaces.

The load, which was different for the linear buckling analysis, cyclic and strength simulations, was prescribed to the reference point (RP). The reference point was then connected in x-direction to the edges of the stiffener and skin using an equation constraint. This creates a distributed load along the edges of the composite part of the panel.

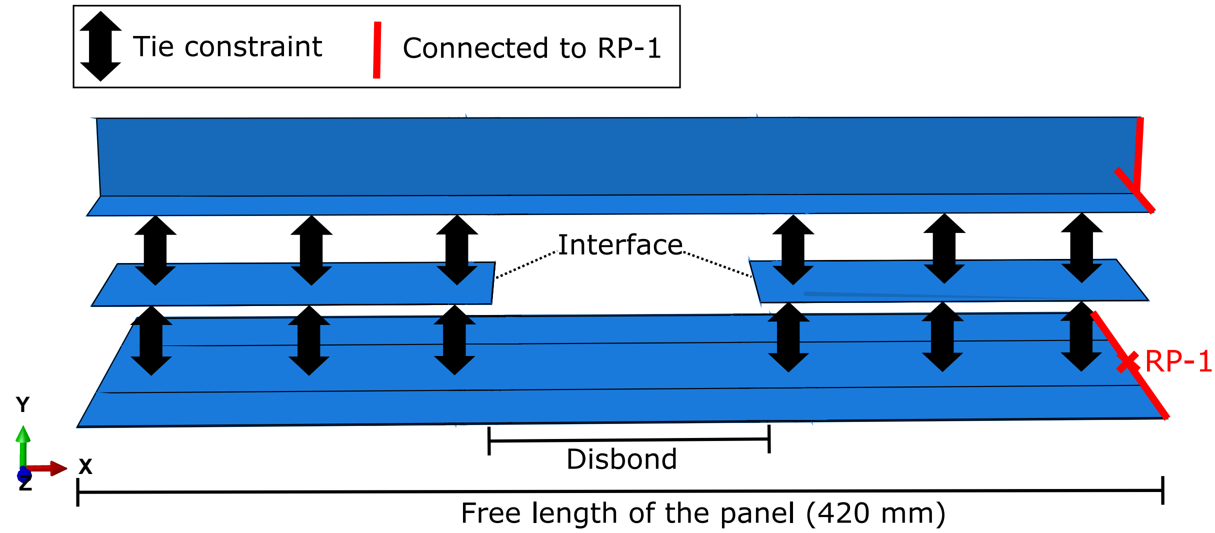

FIGURE 5.1 – Overview of the model of the panel

The boundary conditions that were applied to the model had to be representative of the real testing boundary conditions. As the clamped ends were not modeled to increase the computational efficiency, only the edges of the panel were subjected to these clamping boundary conditions. One edge was still able to translate in the x-direction and the other not. The anti-buckling blades were modeled by not allowing 1.5 mm of the sides of the panel to translate in y-direction or rotate around the z-axis. These boundary conditions can be seen in figure 5.2.

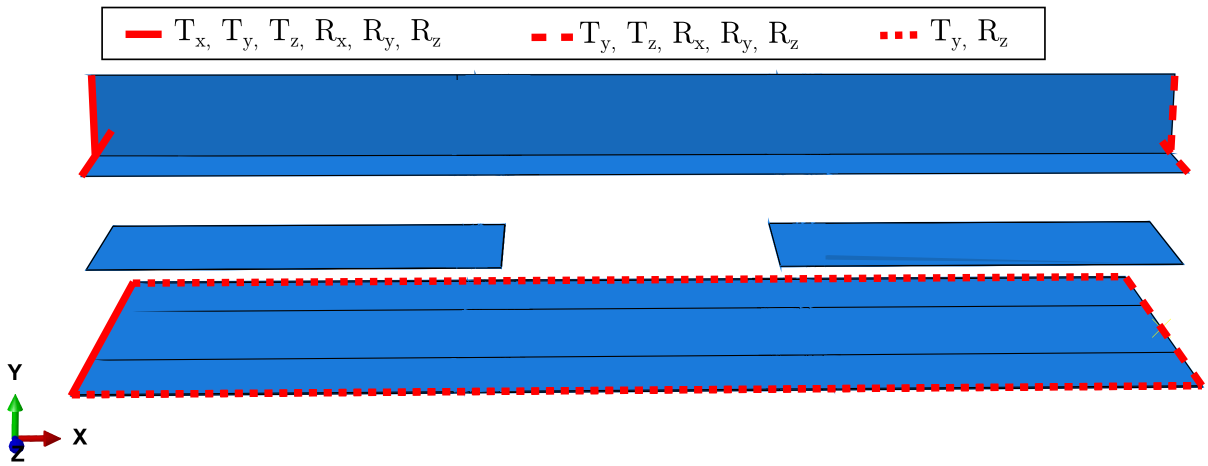

FIGURE 5.2 – Boundary conditions imposed on the model

The lay-up of the skin and stiffener was as previously mentioned in table 3.4. Four node shell elements with reduced integration (S4R) were used to model the laminates. Throughout the thickness a single integration point was assigned to each ply, resulting in constant stress and strain in the plies. This was not considered a problem because the relatively large amount of plies still allowed for smooth stress/strain changes throughout the laminate thickness. The cohesive elements were eight node reduced integration linear brick elements (C3D8R), as is required for the VUMAT.

5.1.2 Linear Buckling analysis

A relatively simple mesh, as depicted in figure 5.3, was sufficient to get a good trade-off between a smaller mesh size at the buckling shape and a rougher mesh at the edges, while keeping the time spend on modeling local mesh refinements low. A mesh convergence study, in which the element size was halved until the outcome difference was <1%, was performed to determine the final size of the elements.

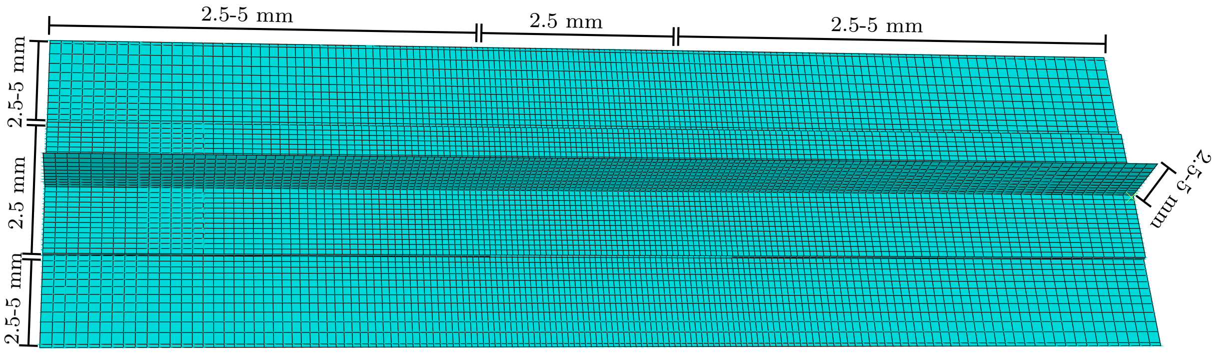

FIGURE 5.3 – Element size distribution of the linear buckling model

The material properties of the plies are given in table 5.1 and the adhesive's properties can be found in table 5.2. The material types are linearly elastic, which is in line with the nature of the simulation considering linear material and geometrical behavior.

TABLE 5.1 – Material properties of the plies, based on table 3.1

$\boldsymbol{E_1}$ [MPa]	$\boldsymbol{E_2}$ [MPa]	$\boldsymbol{\mu_{12} = \mu_{13} = \mu_{23}}$ [MPa]	$\boldsymbol{\nu}$ [-]
$125 \cdot 10^3$	$9.9 \cdot 10^3$	$3.5 \cdot 10^3$	0.34

TABLE 5.2 – Material properties of the adhesive, based on table 3.2

$\boldsymbol{E}$ [MPa]	$\boldsymbol{\nu}$ [-]
3100	0.33

5.1.3 Quasi static compression

The RTA reference panel in the experiments failed due to a combination of delamination between the stiffener and skin and failure in the CFRP of the skin and stiffener. The delamination was modelled using the VUMAT model developed by Oliveira (2018). The damage in the CFRP was modelled using the readily available Hashin's damage model, which is based on the work of Hashin and Rotem (1973) and Hashin (1980). This damage model can be used for any anisotropic material, but is primarily intended for fiber reinforced polymers [ABAQUS Inc. 2014]. The theory behind Hashin's damage model can be found in appendix D.

A much finer mesh was required to adequately model the damage growth in the cohesive and the CFRP than was used for the linear buckling analysis. Mesh convergence studies showed that the mesh required to adequately model the disbond growth was finer than for the damage propagation in the CFRP. With this in mind mesh transitions were used to keep the computational costs low, while having a fine mesh in the areas where damage occurred. The locations of the mesh transitions can be seen in figure 5.4. A close-up of what the mesh transitions look like can be seen in figure 5.5.

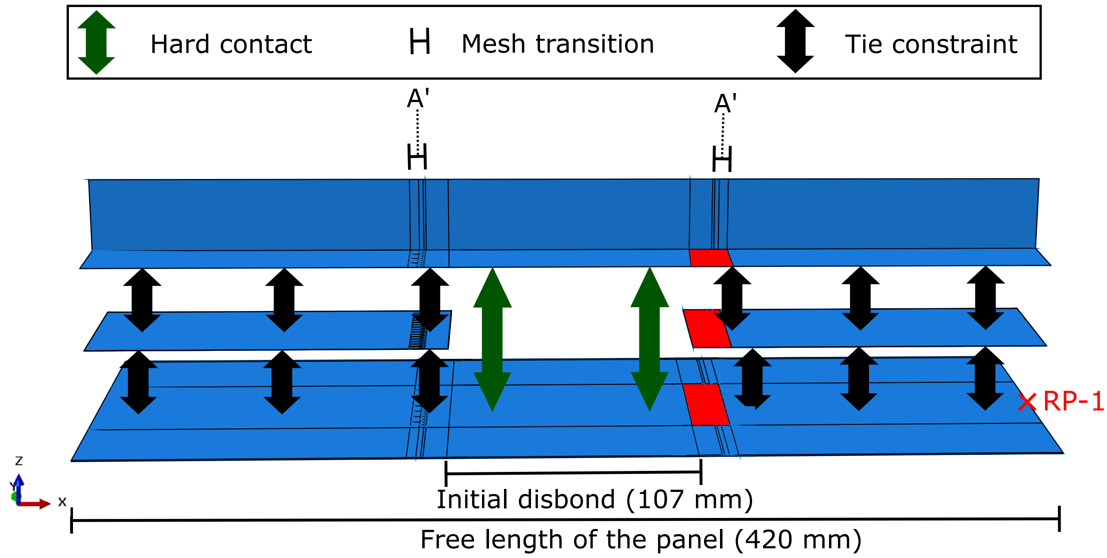

FIGURE 5.4 – Overview of the geometry of the panel
Red areas are possible locations of the mesh transition displayed in figure 5.5

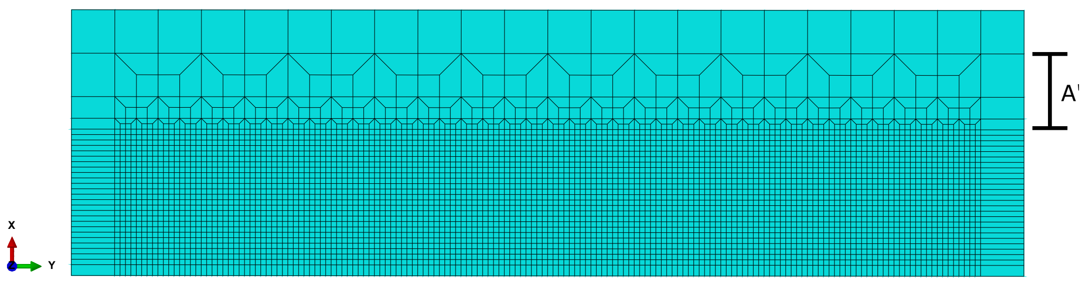

FIGURE 5.5 – Close-up of the mesh transition

Using these transitions, the final mesh was as explained in figure 5.6

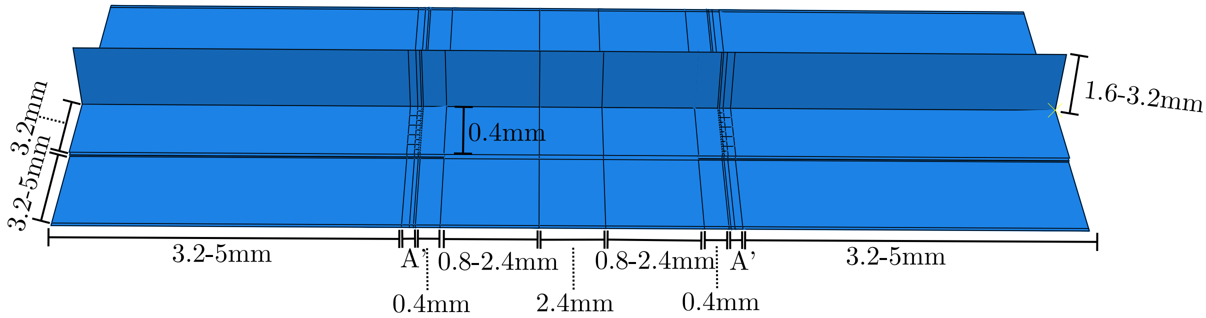

FIGURE 5.6 – Element size distribution of the quasi-static compression model

The material properties used as input for the model were largely the same as mentioned in the materials section 3.1. The only difference being the strength properties of the adhesive. The strength of an interface is generally stronger than the strength of the adhesive itself. Coupon level simulations confirmed that using the adhesive's strength properties resulted in too early disbonding. Therefore, the strength properties of the interface were modified to the ones visible in table 5.3, which are based on a T800/3900-2B co-cured interface. This proved satisfactory during the coupon simulations. To get a grasp of the influence of this assumption on the predicted static and fatigue damage section 5.6 will discuss the numerical results for an interface strength equal to the shear strength of the adhesive.

TABLE 5.3 – Strength properties of the interface layer [Arbelo 2017]

$\boldsymbol{S_{33}}$ [MPa]	$\boldsymbol{S_{12}}$ [MPa]	$\boldsymbol{S_{23}}$ [MPa]
50	180	180

As stiffness of the CFRP, the compression values of table 3.1 were used. The fracture toughness and strength required both compression and tensile values due to the way Hashin's damage model calculates damage.

The simulation was performed using the dynamic explicit solver through the dynamic relaxation method, with geometrical non-linearities activated. To speed up the simulation mass scaling was used. Mass scaling changes the density of elements which have high wave speeds to increase their stable time increment [ABAQUS Inc. 2014]. A target stable time increment of 1E-06 seconds resulted in relatively high computational speed while keeping the kinetic energy low compared to the internal energy. A criterion stating that the kinetic energy could not be more than 10% of the internal energy was used for this, to make sure dynamic effects were limited in the simulation. The total step time of the simulation was set at 0.5 second, during which the panel was compressed 3 mm. Using a single core of an i7 intel processor this resulted in a computation time of roughly 24 hours.

5.1.4 Post-buckling compression fatigue and residual strength

A single model was used to model the compression fatigue and residual load experiments. This way the acquired damage during fatigue was automatically taking into account during the residual strength simulation. The model was largely the same as the one used for the ultimate load, as described in subsection 5.1.3. The main differences being the input of fatigue related material parameters in the adhesive and the applied load. The additional material parameters are given in table 5.4.

TABLE 5.4 – Fatigue related material properties in the adhesive

Parameter	**Value**	**Unit**	**Description**
l_e	0.2	[mm]	Element size along crack direction
C_I	0.00221	[-]	Mode I Paris constant*
n_I	5.09	[-]	Mode I Paris exponent*
C_{II}	0.122	[-]	Mode II Paris constant*
n_{II}	4.38	[-]	Mode II Paris exponent*
C_b	609,000	[-]	Mixed mode Paris interpolation constant*
n_b	5.48	[-]	Mixed mode Paris interpolation exponent*
$G_{I,th}$	0.0627	[N/mm]	Fatigue threshold value mode I [Garpelli 2018]
$G_{II,th}$	0.0593	[N/mm]	Fatigue Threshold value mode II [Garpelli 2018]
$n_{b,th}$	2.737	[-]	B-K interpolation exponent for G_{th}**

* Obtained from Blanco et al. (2004) for co-cured HTA/6376C

** Obtained from Asp et al. (2001) for co-cured HTA/6376C

Although several coupon level experiments were performed on the material combination used in this research, not all fatigue related parameters were known. For example mode I and II threshold value tests were carried out by Garpelli (2018), but no mixed mode experiments. The material properties that were not known had to be taken from the open literature. Unfortunately, no fatigue related values could be found for the material and bonding combination used in this research. Instead it was chosen to use co-cured HTA6376C, as its material properties ($G_{I,th}$,$G_{II,th}$,G_{Ic},G_{IIc}) were the most similar to the ones used in this research. Not having all material properties well defined is a significant uncertainty in the numerical simulation.

Two steps were used to be able to separately simulate the cyclic loading and the subsequent quasi-static compression until failure. The first step started with a load ramp from 0 to -47.5 kN in 0.1 pseudo seconds. The load was then kept constant for 0.1 pseudo seconds, during which the numerical frequency (3,000,000 Hz) was applied.

The second step was similar as during the quasi-static compression simulation of the reference panels. A 3 mm compression was applied on the panel over a course of 0.5 seconds, during which the panel failed. The entire load build up can be found in figure 5.7. Total computation time using a single i7 core for this set-up was roughly 36 hours.

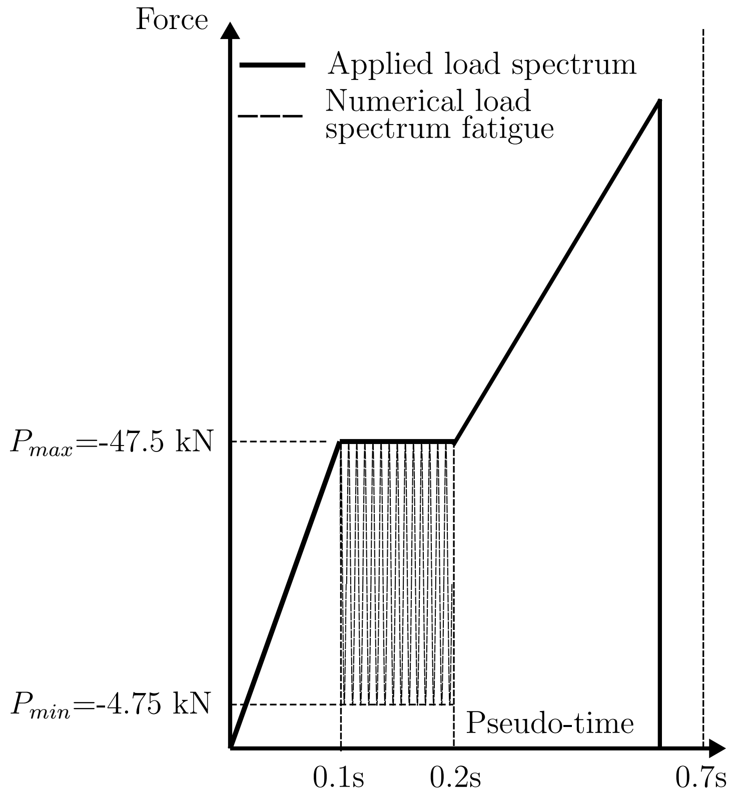

FIGURE 5.7 – Numerical load applied for the fatigue and residual strength simulations

5.2 Linear buckling analysis

The linear buckling analysis was used as a first check for the quality of the model. It is computationally cheap and can be used to compare the experimental and numerical buckling load and shape. The results were expected to match relatively well, as the geometrical behavior before buckling is predominantly linear. In the subsections below first the results of the model described in subsection 5.1.2 are treated. Subsequently, the influence of degraded stiffness properties in the skin at the location of the buckling shape is investigated. This is done to determine whether this could have caused the buckling load to decrease after the cyclic loading, as was suggested in section 4.3.

5.2.1 Pristine panels with initial disbond

The influence of the disbond length on the first buckling load can be seen in figure 5.8. An exponentially decreasing influence of the disbond length on the buckling load becomes apparent. From a physical point of view the decreasing buckling load makes sense because the length over width ratio of the skin decreases. As was expected based on the experiments, the influence of the disbond size on the buckling load is relatively small however, as the buckling load only decreases 3.5% between a disbond length of 105 and 115 mm.

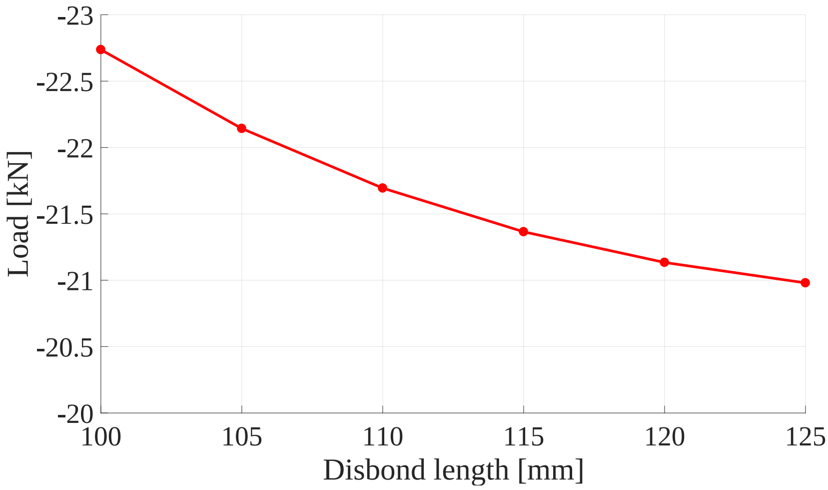

FIGURE 5.8 – Influence of disbond length on the buckling load of the first mode

The buckling load corresponding to a disbond length of 107 mm, which is representative for the RTA panels before cyclic loading, was equal to -21.7kN. This is 4.5% lower than the buckling load of the reference panel 405-01-RTA. Indicating that the influence of non-linearities before buckling are indeed relatively small. The shape of the first buckling mode is displayed in figure 5.9. Similar to the observations from the DIC camera, which are repeated in figure 5.10, a diagonal buckling shape can be distinguished.

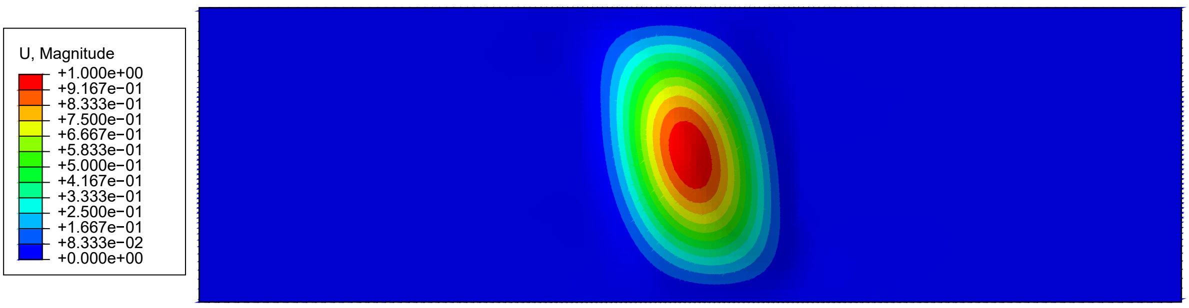

FIGURE 5.9 – Buckling shape of the first buckling mode
U being the normalized total displacement

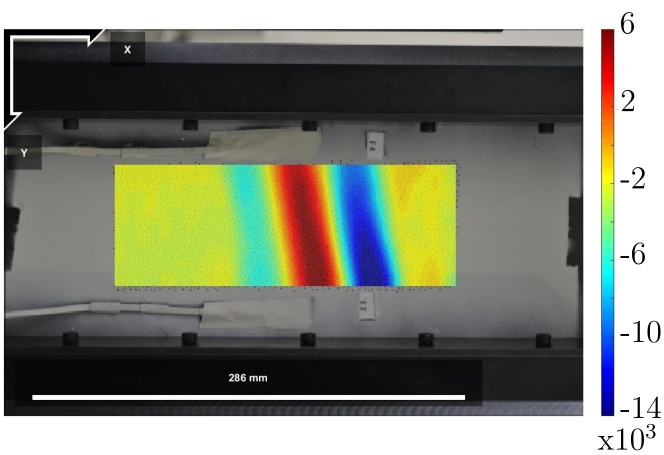

FIGURE 5.10 – Strain field 405-01 RTA ($\mu\epsilon_{xx}$) at a load of -50 kN

5.2.2 Influence of decreased stiffness on the buckling load

During the ultimate load simulation, which will be described in section 5.3, at a load of -47.5 kN static damage occurred in the skin's matrix at the location of the disbond. If this damage indeed occurred during static loading it could have grown further in fatigue, though no estimation can be made of how much due to the previously mentioned lack of numerical tools readily available for this purpose. To investigate whether matrix damage by itself can cause the buckling load to drop from -22.8 kN to -16.3 kN, the matrix related stiffnesses were varied over the full width of the skin at the disbonded area. This resulted for example in the material properties of table 5.5 for a stiffness decrease of 50%. The simulation was performed with a disbond length of 110 mm.

TABLE 5.5 – Material properties of the plies at the location of the disbond for a 50% decrease in matrix stiffness

$\boldsymbol{E_1}$ [MPa]	$\boldsymbol{E_2}$ [MPa]	$\boldsymbol{\mu_{12} = \mu_{13} = \mu_{23}}$ [MPa]	$\boldsymbol{\nu}$ [-]
$125 \cdot 10^3$	$4.45 \cdot 10^3$	$1.75 \cdot 10^3$	0.34

From figure 5.11 it can be seen that a large reduction in matrix related stiffness is required to be able to decrease the load all the way to the experimentally measured load during the residual strength tests. However, it also becomes apparent that the matrix stiffness influences the buckling load. Hence, if matrix damage indeed already occurred during the static loading at -47.5 kN and grew during the fatigue, it is probable that this phenomenon was indeed partially, but unlikely entirely, responsible for the decrease in the experimental buckling load after cyclic loading.

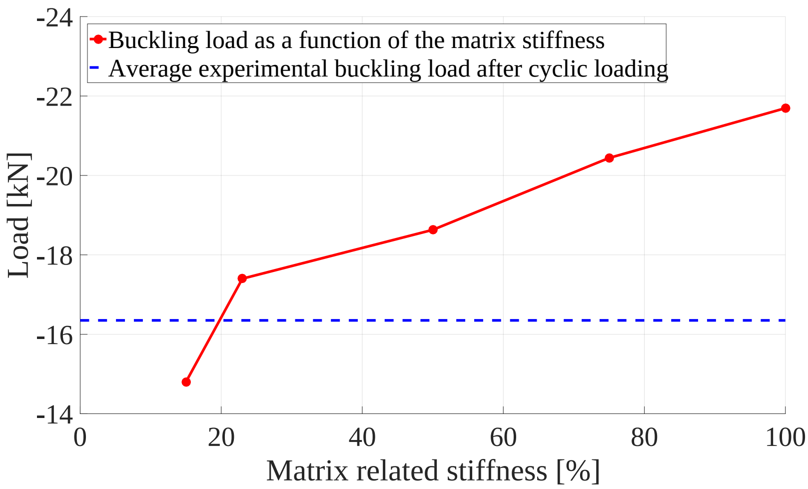

FIGURE 5.11 – Influence of degraded matrix related stiffness on the buckling load

5.3 Quasi static compression reference panel

To further validate the numerical model before subjecting it to cyclic compression loading, its quasi-static (post-)buckling and failure behavior were compared to the experimental data of panel 405-01 RTA. The former is treated in subsection 5.3.1 and the latter in subsection 5.3.2.

5.3.1 Buckling and post-buckling

Figure 5.12 compares the axial and membrane strains from the numerical simulation to the experiments at the location of strain gauge 4. From these graphs it can be seen that the overall behavior of the numerical model matches well with the experiment. The difference between the numerical and experimental buckling load of 8.5% is considered acceptable when considering that the numerical simulation assumes a perfect panel, whereas in real life panels will always contain imperfections. Moreover, the boundary conditions might also play a role, as the tightness of the clamped ends was not perfect in the experiments as discussed in section 4.1.

One aspect in which the numerical model does not match the experimental behavior is the disbond growth before failure. All RTA and RTW panels, with and without fatigue damage, displayed a sudden growth in disbond length before the final fracture. The numerical model only shows this disbond growth at the moment of failure. This is why the sudden jump in strain around -100 kN, as for example visible for the membrane strain in figure 5.12b, does not occur in the numerical model. This might be an indication that the interface strength as described in table E.1 is too high and does not allow for enough disbond growth.

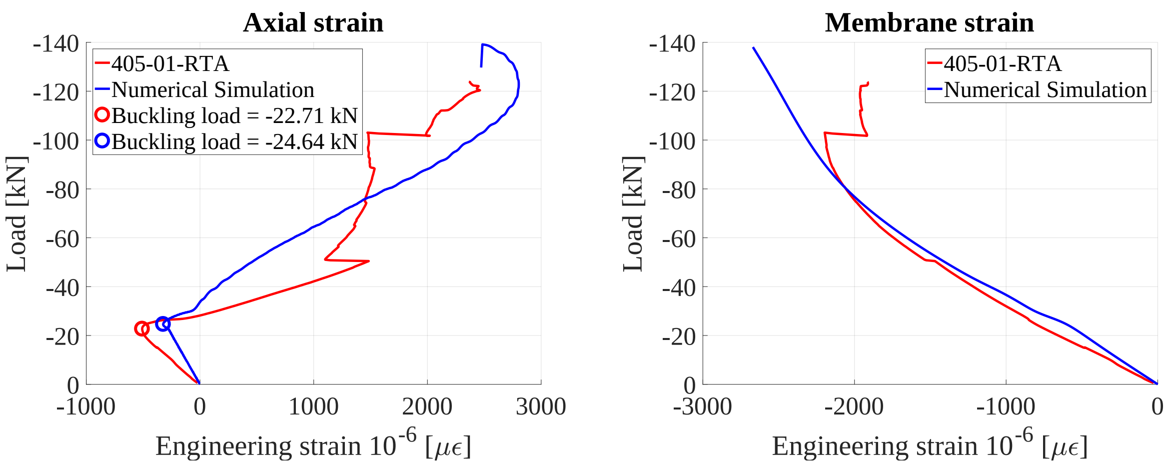

(a) Strain gauge 4 (b) Strain gauges 3 and 4

FIGURE 5.12 – Numerical and experimental buckling behavior

5.3.2 Failure

Figure 5.13a shows the load shortening curves of the numerical simulation and 405-01-RTA. Because the membrane strain in the stiffener had proven more reliable for other experiments, but was not available for 405-01-RTA due to malfunctioning of strain gauge 5, also the membrane strain in the stiffener was compared to 405-02-RTA and 405-01-RTW. The former after being subjected to cyclic loading and the latter subjected to hygrothermal aging. This was not considered problematic though, as no signs of stiffness degradation due to the hygrothermal aging or the cyclic loading were distinguished in chapter 4.

The numerical model does not simulate the fact that the stiffness of the panel in the load-displacement curve is not perfectly linear up to the point of failure. Interestingly, the membrane strain in both the stiffener (figure 5.13b) and skin (figure 5.12b) were predicted correctly. This indicates that non-linearities outside the panel itself might play a role in the above mentioned discrepancy. Possible factors that could cause this are deformations in the experimental set up, incorrect alignment of the LVDT or an imperfect contact of the panel with the clamped end boundary conditions.

The model overestimated the ultimate load of the panel by 12%. This was potentially caused by the way the clamped ends were modeled. By not simulating the clamped ends, it was assumed that a perfect potting was present, whereas in subsection 4.1.2 it was already shown that in practice the ends were not completely clamped. In future experiments this problem could be mitigated by using potted ends of for example epoxy and aluminum powder, as was done by Bisagni and Davilia (2014). Another possible influence is the aforementioned strength of the interface layer, for which co-cured T800/3900-2B was used. This could have lead to less disbond growth, keeping the panel more stable until collapse.

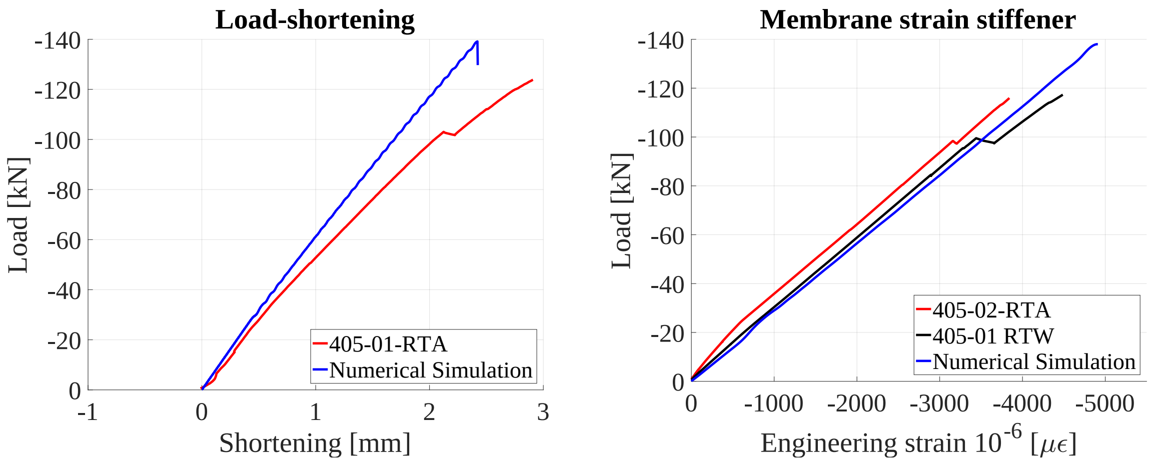

(a) Load vs shortening

(b) Averages of strain gauges 5 and 6

FIGURE 5.13 – Numerical and experimental failure behavior

By requesting the damage in the CFRP and the cohesive as output it was possible to determine the progression of damage throughout the simulation. Interestingly, a small amount of matrix damage already occurred in the skin at a load of -47.5 kN, as can be seen in figure 5.14. It was previously mentioned in subsections 4.3.1 and 5.2.2 that damage in the skin at the disbonded area was suspected to be one of the causes of the decreased buckling load after the cyclic loading. As the resistance against crack growth of CFRP is generally lower in cyclic than static loading, the static damage visible in figure 5.14 could have kept on growing during the cyclic loading. A numerical model simulating high cycle fatigue in CFRP could help validating this statement, however this is outside of the scope of this research as no such damage model is readily available in Abaqus.

One side note has to be placed about the fact that Abaqus' Hashin damage model does not account for in-plane shear non-linearities. This simplification means that the total shear damage gets over predicted. Potentially meaning that the predicted static skin damage at -47.5 kN is not present in the experiments. However, even if this is the case, it does not exclude fatigue damage from occurring during cyclic loading.

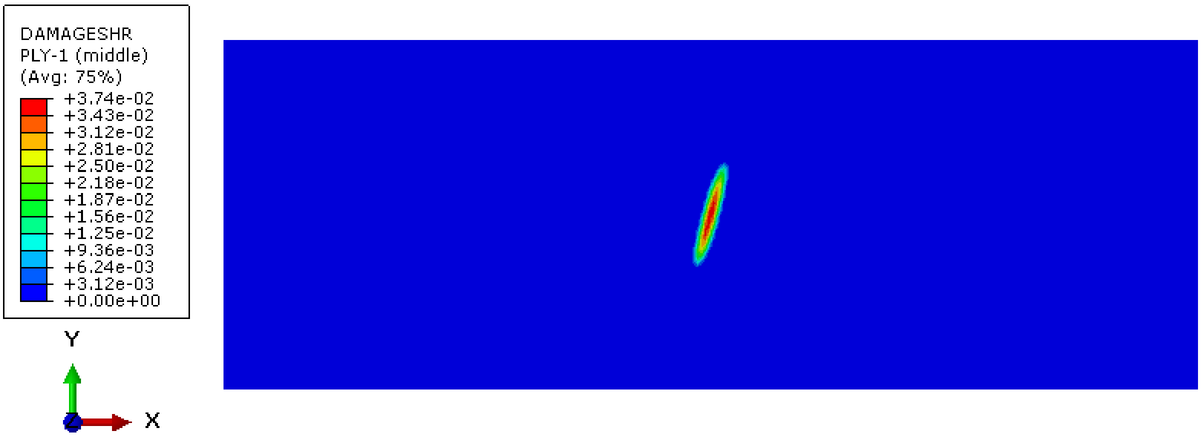

FIGURE 5.14 – Static shear damage in the bottom ply of the skin at -47.5 kN

Right before the final failure of the panel the previously described skin damage had progressed quite significantly in the numerical model. Interestingly, the location and severity of the damage depended on the ply number. The ply farthest away from the stiffener (bottom ply) damaged in the middle of the buckling shape, as can be seen in figure 5.15. The top ply on the other hand damaged more towards the sides, whereas the mid plies did not show any damage at all. This can be seen in figures 5.16 and 5.17. No shear damage occurred in the stiffener until final failure of the panel.

These differences were caused by the different location of tensile and compression stresses along the stacking sequence. As the tensile strength of the matrix is much lower than the compression strength the skin is more inclined to damage at locations where tensile stress is present. In the bottom ply tensile stress occurs in the middle of the buckling shape. In the top ply on the other hand compression is present at that location and tensile stress takes place more towards the edges of the disbonded area. This is a direct consequence of the single half wave buckling shape.

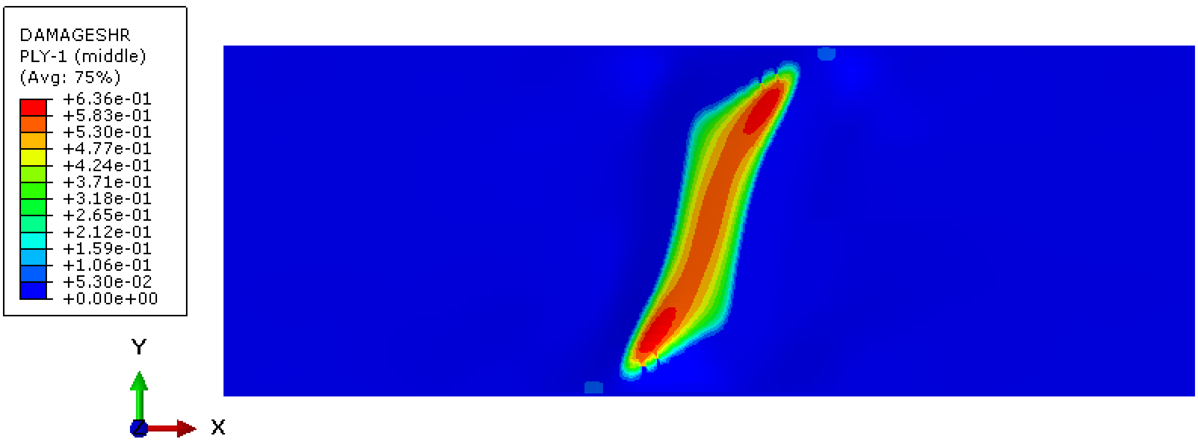

FIGURE 5.15 – Shear damage in the bottom ply of the skin just before collapse

FIGURE 5.16 – Shear damage in the mid plies of the skin just before collapse

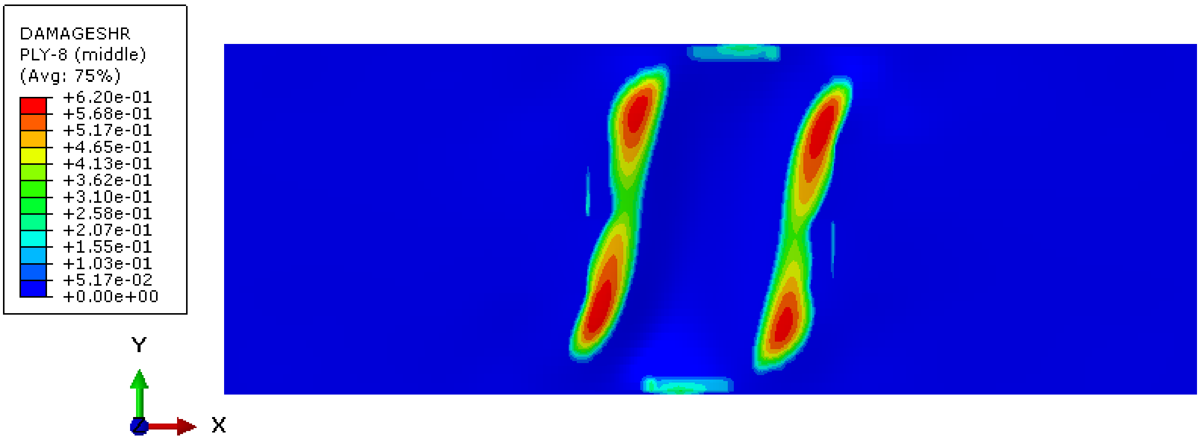

FIGURE 5.17 – Shear damage in the top ply of the skin just before collapse

The panel in the numerical simulation failed first in the skin. This failure was accompanied by simultaneous damage growth in the cohesive, for as far as the frequency of output requests went. Figures 5.18 and 5.19 show both the skin and cohesive at the moment of failure. Before the failure only marginal damage was present in the cohesive. Immediately after the damage in the skin the stiffener breaks as well, as displayed in figure 5.20.

The numerical failure pattern matches well with the experimental failure of panel 405-01 RTA described in subsection 4.1.2. For clarity reasons a post-failure picture of 405-01 RTA is repeated in figure 5.21. Both the numerical and experimental panel failed in different locations for the skin and stiffener and the stiffener did not fail in the mid plane. Unfortunately, it was not possible to determine the experimental sequence of the failure due to the fact that on the recorded videos no difference in skin and stiffener failure could be distinguished. Using a high speed camera for future experiments can mitigate this problem.

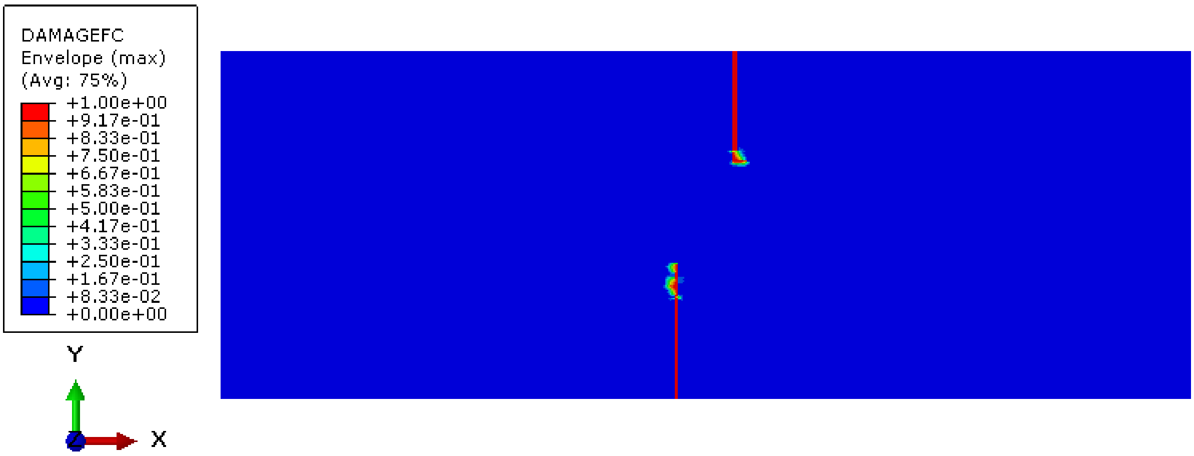

FIGURE 5.18 – Fiber compression damage in the skin at the moment of failure

FIGURE 5.19 – Disbond size at the moment of failure in the skin
SDV17 being the value of the stiffness damage variable

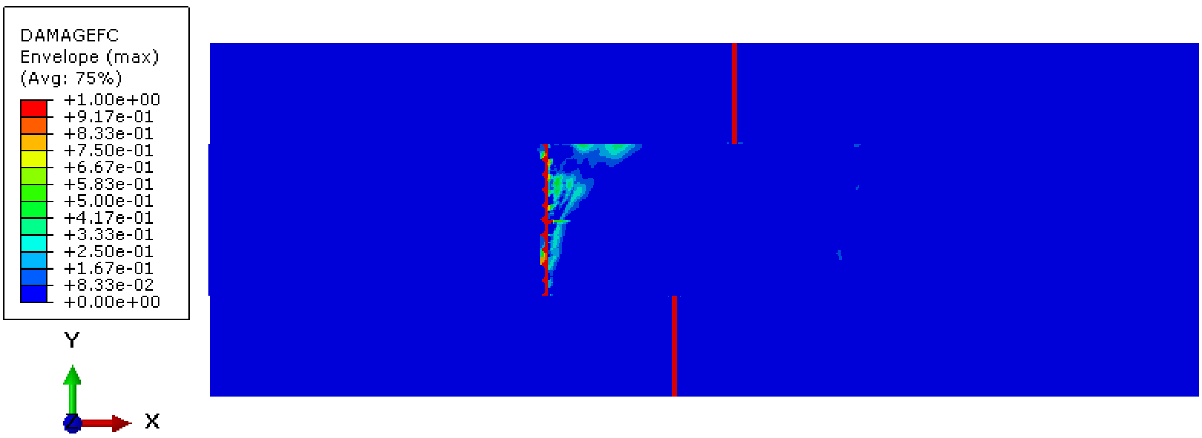

FIGURE 5.20 – Fiber compression damage in the skin and stiffener immediately after skin failure

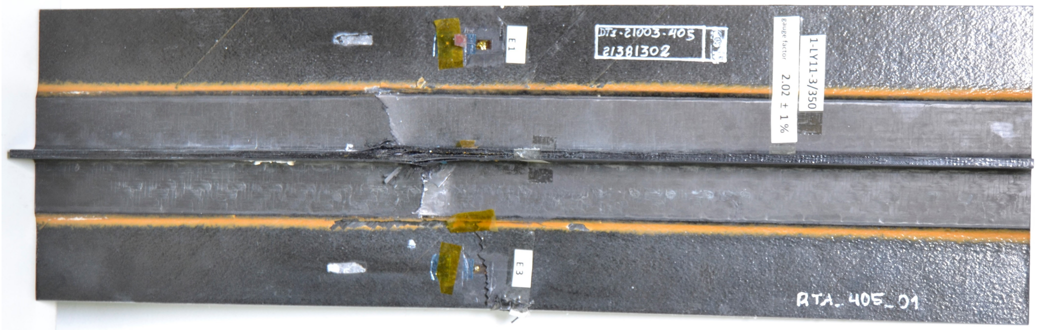

FIGURE 5.21 – Post-failure 405-01 RTA

5.4 Post-buckling compression fatigue

The goal of the numerical simulation of the post-buckling fatigue was to model the disbond growth during the cyclic loading. This damage progression is treated in subsection 5.4.1. Subsequently, several factors that may have caused a difference in the numerical and experimental results are discussed in subsection 5.4.2.

5.4.1 Disbond growth

A comparison of the numerical and experimental disbonded area and length over the course of the 300,000 cycles can be seen in figures 5.22 and 5.23, where it has to be noted that the numerically disbonded area was calculated semi-continuously and the numerical disbond length measured manually at set points. Similar to in the experiments, the disbond growth was measured from the first cycle onward. This is also why it is possible that the length remains constant during the first cycles, whereas the area grows. During these cycles the bond only grows diagonally.

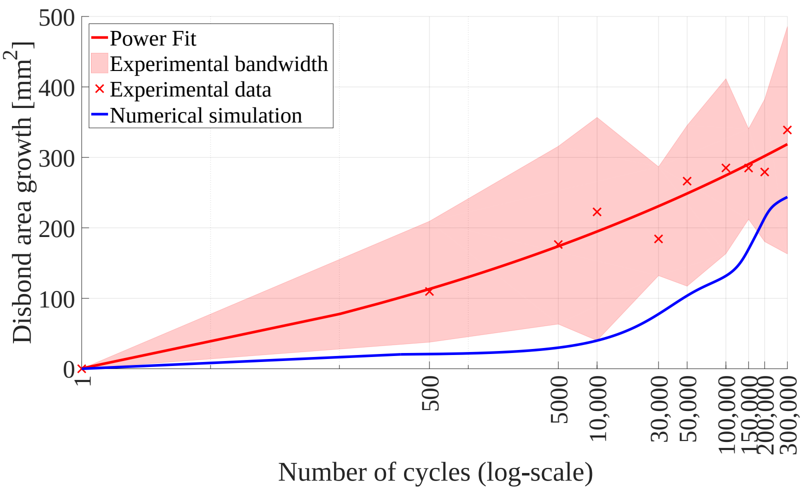

FIGURE 5.22 – Experimental and numerical growth of the disbonded area

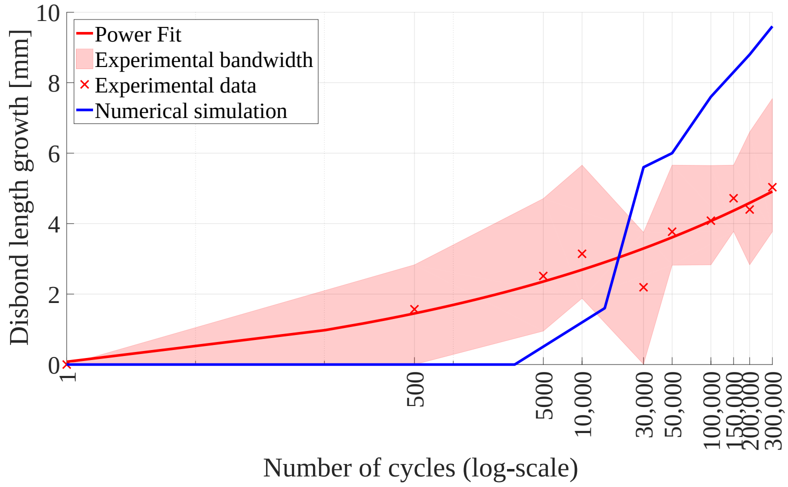

FIGURE 5.23 – Experimental and numerical disbond length growth

Figure 5.22 shows that the numerical model slightly underestimates the growth of the disbonded area, whereas from figure 5.23 it can be distinguished that the length, once it starts growing, overestimates the experiments quite severely. This combination indicates that the numerical disbond grew more diagonal than the experimental disbond. This is confirmed by comparing the numerical disbond shape, as displayed in figure 5.24, to the experimental disbond shape that is repeated in figure 5.25.

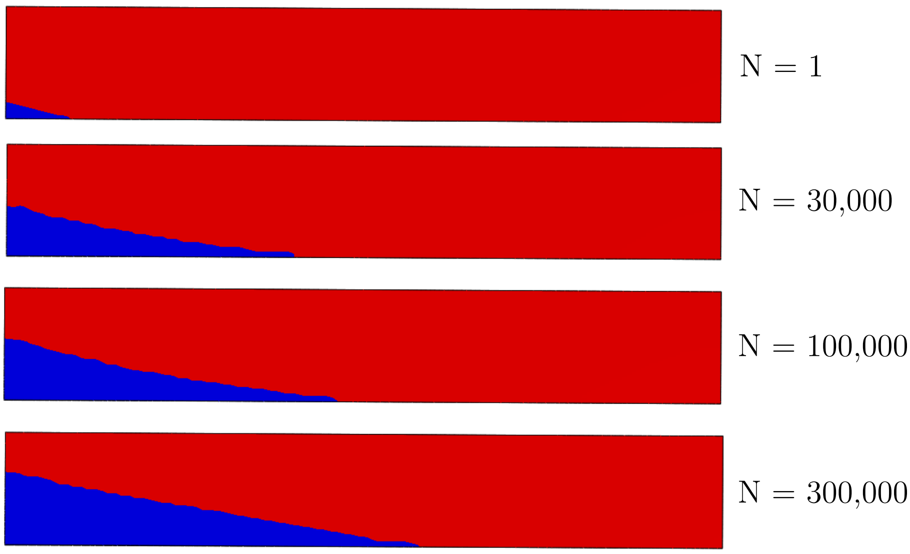

FIGURE 5.24 – Numerical disbond growth (blue)

One edge of the disbond is displayed and it is rotated 90°. Moreover only the first 10 mm of the bonded/disbonded area is shown.

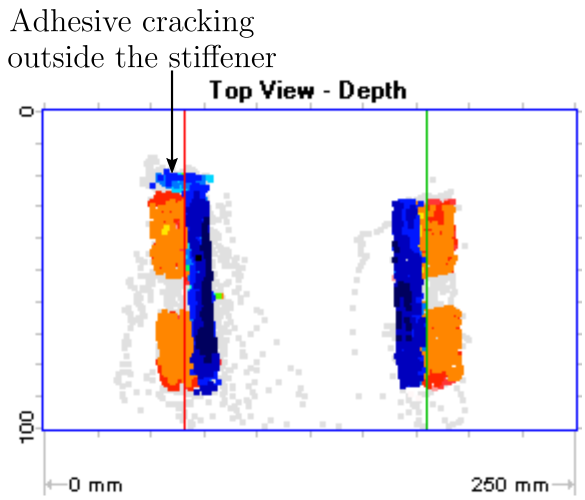

FIGURE 5.25 – Experimental disbond (blue) 405-02 RTA after 300,000 cycles

The diagonal disbond shape is caused by the buckling shape at -47.5 kN, as presented in figure 5.26. Due to this buckling shape the SERR is much higher in the corners at which disbond growth takes place. The severity of this effect can be seen in figure 5.27, where the SERR along the width of the crack is displayed. These two figures combined suggest that in the currently proposed model the crack will likely always grow more diagonal than was determined experimentally.

Figure 5.26 also shows that the maximum out of plane displacement is 2.3 mm. The numerical out of plane displacement did not increase significantly after 300,000 cycles. This is in contrast to what was previously reported about the increase of out of plane displacement throughout the fatigue experiments in figure 4.12. Once again this indicates that not only the disbond growth played a role in the change of buckling behavior after the cyclic loading. Rather, effects not included in these simulations, such as fatigue damage in the CFRP, may have played a role.

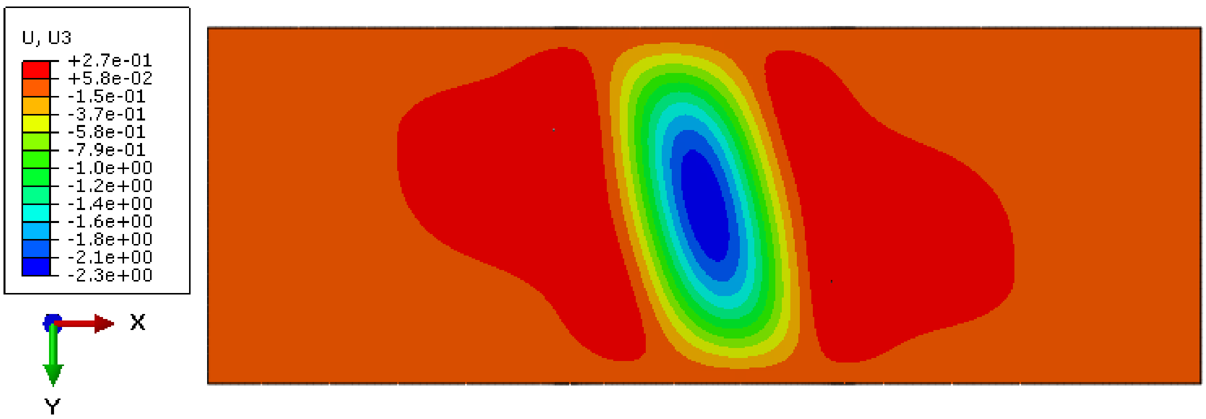

FIGURE 5.26 – Out of plane displacement in the skin at -47.5 kN

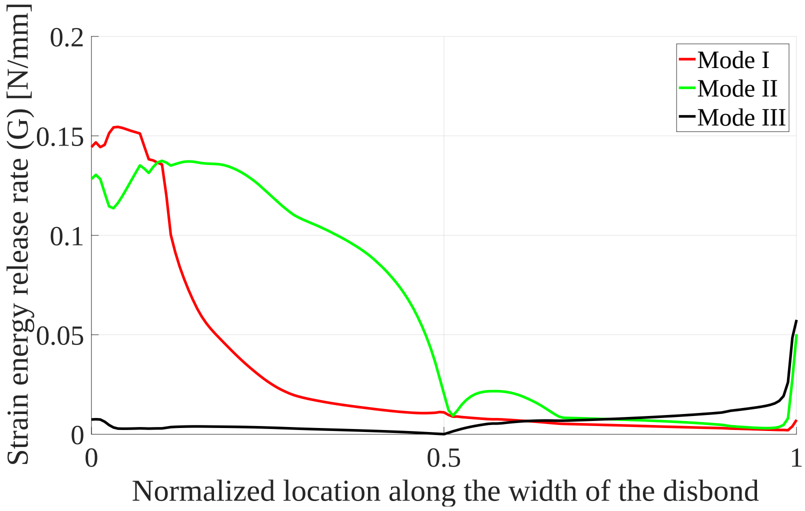

FIGURE 5.27 – SERR ratio at the bonded/disbonded edge at the end of the first cycle (along the y-axis in figure 5.26)

An additional simulation was performed to check whether the larger initial disbond of the RTW panels could have indeed resulted in less disbond growth, as was suggested in section 4.2. In this simulation an initial disbond of 112 mm, representative of the RTW panels after pre-cracking, was used. This 5% increase in initial disbond size caused the disbonded area to grow by 15% less than the original simulation. This indicates that the larger initial pre-crack of the RTW panels was indeed partially responsible for the decreased disbond growth.

5.4.2 Possible causes of the discrepancies between the numerical model and the experiments

This subsection discusses several factors that may have lead to the differences in disbond growth between the numerical prediction and experimental outcome.

Fatigue material properties: As was already mentioned in subsection 5.1.4, the Paris law parameters used to predict the disbond growth in fatigue were taken from a different material combination (HTA/6376C) and bonding technique (co-cured). Although HTA/6376C and T800/3900-2B are relatively similar with respect to strength, stiffness and fracture toughness, there is no comparison between the material properties and the adhesive EA 9695. Based on the information currently available it is not possible to say how much this influenced the simulation. For future simulations however it is recommended to first determine all parameters of the Paris law through coupon level experiments.

Static strength of the interface: As was mentioned in subsection 5.1.3 the strength properties of co-cured T800-3900-2B were used to define the strength of the interface. The influence of this assumption on both the static and cyclic behavior of the panel will be investigated in section 5.6.

Local SERR ratio: The numerical model assumes that the local ratio of $\frac{G_{min}}{G_{max}}$ is equal to the global R-ratio of $\frac{P_{min}}{P_{max}}$. Although this assumption is reasonably valid for coupon level experiments, the complex geometrical non-linearities related to buckling make it more difficult to validate this assumption for sub-component simulations. The fact that

$\frac{G_{min}}{G_{max}}$ is proportional to R^2 suggests however that this influence is likely to be limited. Nevertheless, a separate investigation should be performed to confirm this.

Lack of fatigue damage in the CFRP: If the skin did indeed suffer from fatigue damage as a consequence of the repeated out of plane bending this would explain why the out of plane displacement in the numerical simulation does not increase the way it does in the fatigue experiments. It is likely that an increase in out of plane displacement also results in more disbond growth. As stated before, including CFRP in the numerical model was considered out of the scope of this research.

Accuracy c-scan: As discussed in subsection 4.2.1, the low accuracy of the Isonic 2006 likely was responsible for the relatively large bandwidth of the experimental disbond growth. It might have had a particularly significant influence on the disbond length, as this is more dependent on small deviations near the edges due to the diagonal shape.

5.5 Residual strength

As was explained in subsection 5.1.4 the simulation of the residual load test was performed using a second step within the fatigue model. This means that a loss of stiffness during the fatigue step is directly visible in the local load-strain curves. Figure 5.28 shows the membrane strain in the stiffener, from which it can be distinguished that the disbond growth did not result in a loss of overall stiffness or strength in the panel. This is consistent with the experiments in which the stiffness and strength of the panel did not decline as a consequence of the cyclic loading either. The residual load model overestimates the strength of the panel by roughly 14%.

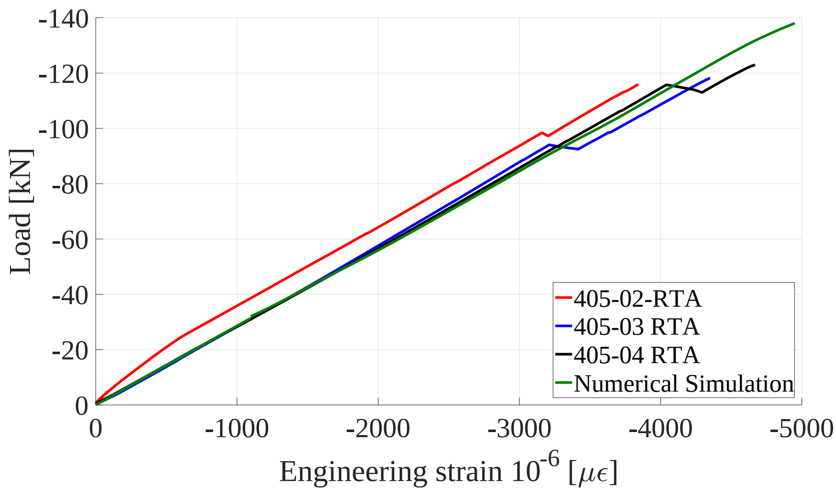

FIGURE 5.28 – Membrane strain stiffener

The observed failure modes were similar to the quasi-static simulation: failure in the skin accompanied by disbond growth, immediately followed by failure in the stiffener. Even the total amount of disbonded area at the moment of failure was not significantly different from the reference simulation, as was displayed in figure 5.19. For this reason these figures are not repeated here.

Overall it can be concluded that the numerical disbond growth during the cyclic loading did not alter the behavior of the panel in the subsequent quasi-static simulation. This is in agreement with the experiments where only the buckling load changed significantly. This effect was not present in the numerical simulation, likely partially because fatigue damage was not taken into account in the CFRP.

5.6 Sensitivy of the numerical results to the static strength of the interface layer

In subsection 5.1.3 the choice for the strength properties of the interface of co-cured T800/3900-2B was explained. However, whether these properties are truly representative for the strength of the co-bonded interface is not known. It proved satisfactory during the quasi-static coupon level simulations, but its influence on sub-component level, as well as during cyclic loading, is not yet known.

To be able to get a grasp of how important the strength properties of the interface are for the numerical results, this section demonstrates its influence on both the fatigue related disbond growth and residual strength of the panel. The modified interface strength in these simulations was chosen equal to the shear strength of the adhesive ($S_{33} = S_{12} = S_{23} = 31$ MPa).

5.6.1 Disbond growth in fatigue

Figure 5.29 shows the numerical growth of the disbonded area using the updated and original strength and compares it to the experimental disbonded area growth. It can be seen that the disbond growth increases and matches better with the experimentally obtained values. This does not show that these strength values are more realistic, as using these values for coupon level simulations lead to incorrect results. It does demonstrate however how important it is to use the correct values for a specific material combination.

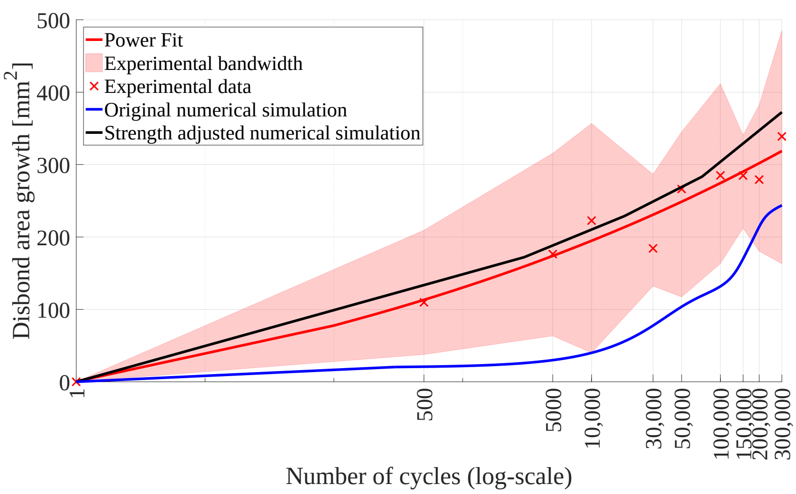

FIGURE 5.29 – Influence of the static interface strength on the disbond growth

5.6.2 Residual strength

The influence of the interface strength on the residual strength of the panels becomes clear from figure 5.30. The load at failure of the panel is 11% lower than originally predicted in figure 5.28 and therefore matches better with the experimental results. Interestingly, the failure mode changed from compressive fiber failure in the skin followed by the stiffener to solely disbond induced failure. The numerical load decreased when a sudden disbond growth occurred. Failure in the skin and stiffener came only after this disbond growth. The amount of disbonded cohesive at the moment of failure can be seen in figure 5.31.

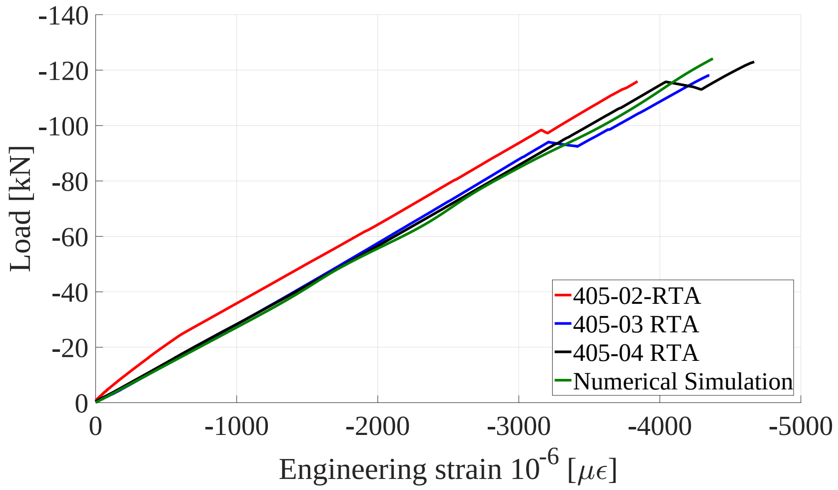

FIGURE 5.30 – Membrane strain stiffener

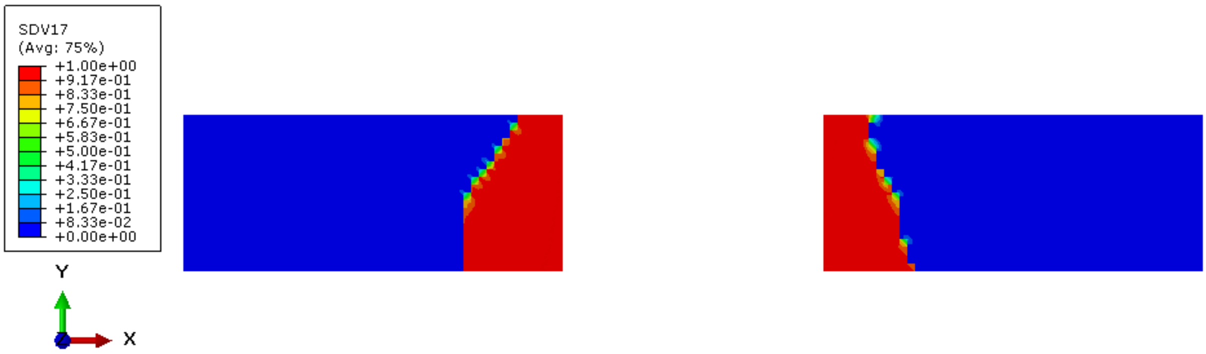

FIGURE 5.31 – Failure of the panel through disbond growth

The discrepancy of the results treated in this section compared to those treated in sections 5.4 and 5.5 show how important it is to use the correct material properties. Future studies are therefore recommended to first determine both the static strength and Paris parameters of the interface layer before conducting any numerical simulations.

5.7 Concluding remarks

The goal of this chapter was to answer research sub-question 2. For clarity this sub-question is repeated here:

2. How can post-buckling fatigue damage in a composite stiffened panel be numerically modeled both efficiently and accurately?

A model to numerically simulate the post-buckling fatigue experiments was proposed in section 5.1. The cohesive zone model proposed by Oliveria (2018) was used to simulate the disbond growth and it was assumed that no fatigue damaged occurred in the CFRP.

The disbond growth in the numerical simulation slowed down in a similar fashion as during the experiments. However, after 300,000 cycles the total growth of the disbonded area was roughly 25% below the experimentally disbonded area, whereas the growth in disbond length was almost 100% larger. This disbond growth did not significantly influence the strength and stiffness of the panel, which matches well with the experiments of the residual load tests. However, as the simulation of the reference panel already overestimated the ultimate strength by 12%, the residual strength was also overestimated by 14%. Several potential causes for the inconsistencies in disbond growth and panel strength, as well as how they can be improved in future studies, were mentioned:

- The numerical model uses Paris law parameters of co-cured HTA/6376C carbon fiber epoxy. Future studies are recommended to perform coupon level fatigue experiments to determine the Paris law parameters required as input of the material model.
- The strength properties of the interface layer were taken from co-cured T800/3900-2B. Future studies are recommended to first determine the static strength of the interface layer through coupon level experiments.
- The CZM uses the global load ratio as the ratio for the SERR at the crack tip. Additional numerical simulations are required to determine how much this influences the final result.
- Lack of fatigue damage in the CFRP, meaning that potential stiffness losses in the skin were not modelled and that therefore the buckling behavior remained constant throughout the simulation. It would be interesting to determine whether local damage in the skin indeed occurred, and if so, whether it influences the disbond growth.
- The c-scan used in the experiments had an accuracy of $\pm$ 2mm. Compared to the total growth of the disbond this is quite significant. Future studies are therefore recommended to either increase the total disbond growth or use a more accurate system to determine the disbond length.
- The imperfectly clamped boundary conditions in the experiments were modeled as perfect. This problem can be mitigated by potting the ends of the panel in epoxy to improve their clamping condition.

In addition to the above described simulations a linear buckling analysis was performed. A good match was found between this simulation and the experimental observations: the disbond length only had a small influence on the buckling load and no influence on the buckling mode. The linear buckling analysis also demonstrated that a 67% decrease of the matrix related stiffness in the skin at the disbonded area was capable of causing a drop in buckling load of 20%. This makes it likely that fatigue induced matrix damage was only partially responsible for the decrease in the experimental buckling load after the cyclic loading.

6 Conclusions and recommendations

Chapters 4 and 5 have answered the research sub-questions. Combining these preliminary conclusions leads to the answer on the main research question as posed in chapter 1:

What is the influence of hygrothermal aging on the post-buckling fatigue behavior of co-bonded composite stiffened panels and how can this cyclic loading be simulated efficiently and accurately?

The answer to this question is treated in section 6.1. Subsequently, section 6.2 discusses several recommendations to improve future research, as well as propose areas upon which future research can focus.

6.1 Conclusions

In order to answer the research question it is relevant to first summarize the effects 300,000 post-buckling load cycles between -47.5 kN and -4.7 kN had on co-bonded composite stiffened panels under RTA conditions:

- The disbond length grew by 4.9 mm and the area by 320 mm^2.
- The disbond grew diagonally. This was caused by the fact that the skin buckled diagonally, which in turn was due to the presence of a 45° layer on the outside of the skin.
- No significant effects on the overall stiffness and strength of the panel were distinguished.
- The buckling load decreased by 28.5 %. This may have partially been caused by local damage in the skin around the disbonded area as a consequence of repeated buckling.

The effect of the hygrothermal aging on the quasi-static behavior of the panels was limited. No noticeable differences between the RTA and RTW panels with respect to strength and stiffness, both before and after the cyclic compression loading, were present. Similarly the bucking load was not affected by the aging.

The behavior of the panel in cyclic loading did change however, as evidenced by the fact that the growth in disbonded area decreased by 75% and the growth in disbond length by 32% with respect to the RTA panels. This may have been caused by either, or a combination of:

- An increase in fracture toughness due to stress relaxation caused by the moisture
- Crack blunting in the adhesive due to the moisture
- The larger initial disbond present for the RTW panels after pre-cracking

The cohesive zone model developed by Oliveira (2018) was used to simulate the damage in the interface layer as a consequence of the cyclic loading. The proposed model underestimated the growth in disbonded area by 25% and overestimated the residual strength by 14%. These numbers were considered satisfactory given the fact that the Paris law parameters and strength properties of the interface layer of different material combinations were used, because the correct values were not available. No damage in the CFRP due to the cyclic loading was modeled. The validity of this assumption is not guaranteed due to the potential fatigue damage that occurred in the skin around the disbonded area. This could also potentially have lead to a lower prediction of disbond growth in the numerical simulation.

Altogether the CZM proposed by Oliverira (2018) is capable of simulating high cycle fatigue in interface layers in composite stiffened panels efficiently, as 300.000 load cycles and the subsequent quasi-static compression until failure could be simulated in less than 36 hours on a single core of an i7 processor. The accuracy of the model should be investigated further using the correct material properties. The results of this research in this regard are promising however.

6.2 Recommendations

This section will first propose several recommendations on how studies investigating the post-buckling fatigue behavior of composite stiffened panels can be improved. Subsequently suggestions will be made on which areas future research should focus.

The goal of investigating a panel is to get as close to a real part as possible without having to use the entire structure. Bisagni et al. (2011) have shown that it is possible to represent a multi-stringer continuous panel using its single stiffened counterpart by choosing the right dimensions and no anti-buckling supports. It is recommended for future studies to follow a similar approach in which numerical simulations help in deciding on the final design of the panel and corresponding boundary conditions. If clamped ends are to be used, the use of epoxy potting is recommended. As every panel is slightly different, metal parts can simply not impose perfect clamping.

To decrease the volatility of the outcome of the fatigue experiments it is recommended to either increase the accuracy of the disbond measuring system or the total amount of disbond growth. The former can be achieved by using a more accurate c-scanning device or possibly by using different measuring techniques such as DIC or piezoelectric wafers. An increase in disbond growth can most easily be achieved by removal of the anti-buckling supports. A numerical simulation confirmed that removal of these supports increases the disbond growth significantly, whereas the effect of for example an increase of the maximum load to -75 kN only influences the growth marginally.

Moreover, it is recommended to first determine all unknown material parameters using coupon level experiments before starting numerical simulations. For the material combination used in this research this leaves the strength of the interface and the Paris parameters. After obtaining them they can than be verified by simulating the coupon level experiments. Subsequently, they can be used on the sub-component scale to predict fatigue related disbond growth. This mitigates uncertainties and increases the reliability of the numerical model.

It is recommended to further pursue the development of high cycle fatigue material models of both CFRP and interface layers in finite element modeling. The CZM used in this work proved of high efficiency, but the accuracy can only be proven when all correct material properties of the panel are used. Future models are recommended to include CFRP fatigue, as damage in the CFRP might also influence the disbond growth. Moreover, using both types of models will aid in their maturation and thus facilitate their future implementation in the industry.

In this research it became clear that the influence of hygrothermal aging on the fatigue behavior of the panels was limited. It would be interesting to investigate what the influence of cold temperature environments would be on similar panels. Planes often fly at high altitudes and adhesives tend to become brittle at low temperatures, potentially leading to a completely opposite effect as the plasticizing of adhesives due to moisture [Adams *et al.* 1992].

The current research should also be extended to the performance of different joining techniques for thermoplastic composites. Thermoplastic composites have the advantage over thermoset composites that they are recyclable and generally posses a high fracture toughness [De Baere *et al.* 2012]. Although the use of thermoplastics in aircraft is already an active field of research, a large comparative study of different joining techniques, such as the INOVA project is doing for thermosets, has currently not yet been performed.

Bibliography

ABANILLA, M. A.; KARBHARI, V. M.; LI, Y. Interlaminar and intralaminar durability characterization of wet layup carbon/epoxy used in external strengthening. **Composites Part B: Engineering**, v. 37, n. 7-8, p. 650–661, oct 2006. ISSN 13598368. Disponível em: <http://linkinghub.elsevier.com/retrieve/pii/S1359836806000412>. 14

ABANILLA, M. A.; LI, Y.; KARBHARI, V. M. Durability characterization of wet layup graphite/epoxy composites used in external strengthening. **Composites Part B: Engineering**, v. 37, n. 2-3, p. 200–212, apr 2005. ISSN 13598368. Disponível em: <http://linkinghub.elsevier.com/retrieve/pii/S135983680500082X>. 14

ABAQUS Inc. 2014. **ABAQUS analysis user's manual**. version 6.14: [s.n.]. 54, 56, 57, 112, 113, 114, 116, 117

ABDELKADER, A. F.; WHITE, J. R. Water absorption in epoxy resins: The effects of the crosslinking agent and curing temperature. **Journal of Applied Polymer Science**, Wiley Subscription Services, Inc., A Wiley Company, v. 98, n. 6, p. 2544–2549, dec 2005. ISSN 0021-8995. Disponível em: <http://doi.wiley.com/10.1002/app.22400>.

ABRAMOVICH, H.; WELLER, T. Repeated buckling and postbuckling behavior of laminated stringer-stiffened composite panels with and without damage. **International Journal of Structural Stability and Dynamics**, World Scientific Publishing Co., v. 10, n. 04, p. 807–825, oct 2010. ISSN 0219-4554. Disponível em: <https://doi.org/10.1142/S0219455410003750>. 3, 24, 25, 26, 27, 28

ADAMS, R.; COPPENDALE, J.; MALLICK, V.; AL-HAMDAN, H. The effect of temperature on the strength of adhesive joints. **International Journal of Adhesion and Adhesives**, Elsevier, v. 12, n. 3, p. 185–190, jul 1992. ISSN 0143-7496. Disponível em: <https://www-sciencedirect-com.ezproxy2.utwente.nl/science/article/pii-/014374969290052W?via%3Dihub>. 52, 77

ANDERSON, T. L. **Fracture mechanics : fundamentals and applications TT -**. 2nd ed.. ed. Boca Raton :: CRC Press,, 1995. ISBN 0849342600 9780849342608 0849389747 9780849389740. xi, 92, 93, 94

ANDERSON, T. L. **Fracture mechanics : fundamentals and applications TT -**. 3rd ed.. ed. Boca Raton :: CRC Press,, 2005. ISBN 0849342600 9780849342608 0849389747 9780849389740. ix, 10, 11, 30, 93

ARBELO, M. A. **FAPESP REPORT: Modelagem de Juncoes Coladas para Aplicacoes em Estruturas Aeronauticas de Materiais Compositos.** Sao Jose dos Campos, 2017. 1–78 p. xiii, 57

ASLAN, Z.; SAHIN, M. Buckling behavior and compressive failure of composite laminates containing multiple large delaminations. **Composite Structures**, Elsevier, v. 89, n. 3, p. 382–390, jul 2009. Disponível em: <http://www.sciencedirect.com/science/article/pii/S026382230800281X>. 3

ASP, L.; SJOGREN, A.; GREENHALGH, E. Delamination Growth and Thresholds in a Carbon/Epoxy Composite Under Fatigue Loading. **Journal of Composites, Technology and Research**, v. 23, n. 2, p. 55–68, 2001.

ASTM. **ASTM D 5573-99, Standard practice for classifying failure modes in fiber-reinforced plastic (FRP) joints**. [S.l.], 1999. 476–478 p.

ASTM. **ASTM D6671 / D6671M - 13e1 Standard Test Method for Mixed Mode I-Mode II Interlaminar Fracture Toughness of Unidirectional Fiber Reinforced Polymer Matrix Composites**. [S.l.], 2013. Disponível em: <http://www.astm.org/cgi-bin/resolver.cgi?D6671D6671M-13e1>.

ASTM International. **Standard Test Method for Mode I Interlaminar Fracture Toughness of Unidirectional Fiber-Reinforced Polymer Matrix Composites BT - Standard Test Method for Mode I Interlaminar Fracture Toughness of Unidirectional Fiber-Reinforced Polymer Matrix Composites**. 2013.

ASTM International. **Standard Test Method for Moisture Absorption Properties and Equilibrium Conditioning of Polymer Matrix Composite Materials BT - Standard Test Method for Moisture Absorption Properties and Equilibrium Conditioning of Polymer Matrix Composite Materials**. 2014.

ATAG. The Right Flightpath to Reduce Aviation Emissions. **Unfccc Cop17**, n. November, p. 1–6, 2010. Disponível em: <http://www.atag.org/our-publications/latest.html>. 1

BANKS-SILLS, L. Update: Application of the Finite Element Method to Linear Elastic Fracture Mechanics. **Applied Mechanics Reviews**, American Society of Mechanical Engineers, v. 63, n. 2, p. 020803, mar 2010. ISSN 00036900. Disponível em: <http://appliedmechanicsreviews.asmedigitalcollection.asme.org/article-.aspx?articleid=1399611>.
95

BARENBLATT, G. The formation of equilibrium cracks during brittle fracture. General ideas and hypotheses. Axially-symmetric cracks. **Journal of Applied Mathematics and Mechanics**, Pergamon, v. 23, n. 3, p. 622–636, jan 1959. Disponível em: <http://www.sciencedirect.com/science/article/pii/0021892859901571>.

BARENBLATT, G. The Mathematical Theory of Equilibrium Cracks in Brittle Fracture. Elsevier, v. 7, p. 55–129, jan 1962. Disponível em: <http://www.sciencedirect.com/science/article/pii/S0065215608701212>.

BENZEGGAGH, M.; KENANE, M. Measurement of mixed-mode delamination fracture toughness of unidirectional glass/epoxy composites with mixed-mode bending apparatus. **Composites Science and Technology**, Elsevier, v. 56, n. 4, p. 439–449, jan 1996. ISSN 0266-3538. Disponível em: <https://www.sciencedirect.com/science/article/pii/026635389600005X>.

BISAGNI, C. Progressive Delamination Analysis of Stiffened Composite Panels in Post-Buckling. In: **47th AIAA/ASME/ASCE/AHS/ASC Structures, Structural Dynamics, and Materials Conference**. American Institute of Aeronautics and Astronautics, 2006, (Structures, Structural Dynamics, and Materials and Co-located Conferences). Disponível em: <https://doi.org/10.2514/6.2006-2178>. 3, 28

BISAGNI, C.; DAVILA, C. Experimental investigation of the postbuckling response and collapse of a single-stringer specimen. **Composite Structures**, Elsevier, v. 108, p. 493–503, feb 2014. Disponível em: <http://www.sciencedirect.com/science/article/pii/S0263822313004650>. ix, 24, 25, 28

BISAGNI, C.; VESCOVINI, R.; DÁVILA, C. **Single-stringer compression specimen for the assessment of damage tolerance of postbuckled structures**. 2011. 495–502 p. 3

BLANCO, N.; GAMSTEDT, E.; ASP, L.; COSTA, J. Mixed-mode delamination growth in carbon–fibre composite laminates under cyclic loading. **International Journal of Solids and Structures**, Pergamon, v. 41, n. 15, p. 4219–4235, jul 2004. ISSN 0020-7683. Disponível em: <https://www.sciencedirect.com/science/article/pii/S0020768304000964>.

BRITO, C. **HYGROTHERMAL EFFECTS ON INTERLAMINAR FRACTURE TOUGHNESS OF COMPOSITE JOINTS**. 2017. xii, 119, 121

BRITO, C.; de Cassia Mendonca Sales Contini, R.; GOUVÊA, R. F.; Scaglioni De Oliveira, A.; ARBELO, M. A.; DONADON, M. V. Mode I Interlaminar Fracture Toughness Analysis of Co-Bonded and Secondary Bonded Carbon Fiber Reinforced Composites Joints. v. 20, p. 873–882, 2017. Disponível em: <http://dx.doi.org/10.1590/>.

BUDHE, S.; BANEA, M. D.; BARROS, S. de; SILVA, L. F. M. da. An updated review of adhesively bonded joints in composite materials. **International Journal of Adhesion and Adhesives**, Elsevier, v. 72, n. October, p. 30–42, 2017. ISSN 01437496. Disponível em: <http://linkinghub.elsevier.com/retrieve/pii/S0143749616302068>. ix, 2, 4, 9, 10, 11, 13, 14, 15, 17, 97, 98

BUDHE, S.; RODRÍGUEZ-BELLIDO, A.; RENART, J.; MAYUGO, J. A.; COSTA, J. Influence of pre-bond moisture in the adherents on the fracture toughness of bonded joints for composite repairs. **International Journal of Adhesion and Adhesives**, v. 49, p. 80–89, mar 2014. ISSN 01437496. Disponível em: <http://linkinghub.elsevier.com/retrieve/pii/S0143749613002170>. 15, 16

BÜRGER, D.; Rocha de Faria, A.; ALMEIDA, S. F. de; MELO, F. C. de; DONADON, M. V. Ballistic impact simulation of an armour-piercing projectile on hybrid ceramic/fiber reinforced composite armours. **International Journal of Impact**

Engineering, Pergamon, v. 43, p. 63–77, may 2012. ISSN 0734-743X. Disponível em: <https://www.sciencedirect.com/science/article/pii/S0734743X11001916>. 99, 100, 101

CAMPILHO, R.; BANEA, M. D.; PINTO, A.; SILVA, L. F. M. da; JESUS, A. de. Strength prediction of single- and double-lap joints by standard and extended finite element modelling. **International Journal of Adhesion and Adhesives**, Elsevier, v. 31, n. 5, p. 363–372, jul 2011. ISSN 0143-7496. Disponível em: <http://www.sciencedirect.com/science/article/pii/S0143749611000273>. 30, 98

CERVENKA, A.; BANNISTER, D.; YOUNG, R. Moisture absorption and interfacial failure in aramid/epoxy composites. **Composites Part A: Applied Science and Manufacturing**, v. 29, n. 9-10, p. 1137–1144, jan 1998. ISSN 1359835X. Disponível em: <http://linkinghub.elsevier.com/retrieve/pii/S1359835X98000128>. 14

CORDISCO, P.; BISAGNI, C. Cyclic Buckling Tests Under Combined Loading on Predamaged Composite Stiffened Boxes. **AIAA Journal**, American Institute of Aeronautics and Astronautics, v. 49, n. 8, p. 1795–1807, aug 2011. ISSN 0001-1452. Disponível em: <https://doi.org/10.2514/1.J050999>. 3

COSTA, M.; VIANA, G.; SILVA, L. F. M. da; CAMPILHO, R. D. S. G. Environmental effect on the fatigue degradation of adhesive joints: A review. **The Journal of Adhesion**, Taylor and Francis, v. 93, n. 1-2, p. 127–146, jan 2017. ISSN 0021-8464. Disponível em: <https://www.tandfonline.com/doi/full/10.1080/00218464.2016.1179117>. 4

DAVILA, C.; BISAGNI, C. Fatigue life and damage tolerance of postbuckled composite stiffened structures with initial delamination. **Composite Structures**, Elsevier, v. 161, p. 73–84, feb 2017. ISSN 0263-8223. Disponível em: <http://www.sciencedirect.com/science/article/pii/S0263822316317925>. x, 3, 25, 26, 27, 28

DAVIM, J. P.; REIS, P. Drilling carbon fiber reinforced plastics manufactured by autoclave-experimental and statistical study. **Materials and Design**, v. 24, n. 5, p. 315–324, 2003. ISSN 02641275. 1

De Baere, I.; JACQUES, S.; Van Paepegem, W.; DEGRIECK, J. Study of the Mode I and Mode II interlaminar behaviour of a carbon fabric reinforced thermoplastic. **Polymer Testing**, v. 31, p. 322–332, 2012. Disponível em: <https://ac.els-cdn.com-/S0142941811002133/1-s2.0-S0142941811002133-main.pdf?_tid=5a9f1f20-e571-4644-95e6-b60931780382acdnat=1532358017_03ebd61e6f899598790c194d6e087f8f>. 77

de Paula Guedes Villani, A.; DONADON, M. V.; ARBELO, M. A.; RIZZI, P.; MONTESTRUQUE, C. V.; BUSSAMRA, F.; RODRIGUES, M. R. B. The postbuckling behaviour of adhesively bonded stiffened panels subjected to in-plane shear loading. **Aerospace Science and Technology**, v. 46, n. Supplement C, p. 30–41, 2015. ISSN 1270-9638. Disponível em: <http://www.sciencedirect.com/science/article/pii/S1270963815002059>. 37

DEGRIECK, J.; Van Paepegem, W. Fatigue damage modeling of fibre-reinforced composite materials: Review. **Applied Mechanics Reviews**, ASME, v. 54, n. 4, p.

279–300, jul 2001. ISSN 0003-6900. Disponível em:
<http://dx.doi.org/10.1115/1.1381395>.

DILLINGHAM, G. **Aviation Safety: Status of FAA's Actions to Oversee the Safety of Composite Airplanes**. Washington, 2011. Disponível em: <https://www.gao.gov/assets/590/585341.pdf>. ix, 2

D.J., H. C. **Durability of sitffened CFRP panels with initial delaminations**. Tese (Doutorado) — Technische Universiteit Delft, 2018.

DOBROWSKI, C.; ROSSMAN, C.; BARTONE, L. **Compressive Strength of Flat Panels with Z-Section Stiffeners**. [S.l.], 1944. 37

DONADON, M.; FARIA, A. **Analysis and Design of Composite Structures**. Sao Jose dos Campos: [s.n.], 2016. 123

DUGDALE, D. Yielding of steel sheets containing slits. **Journal of the Mechanics and Physics of Solids**, Pergamon, v. 8, n. 2, p. 100–104, may 1960. Disponível em: <http://www.sciencedirect.com/science/article/pii/0022509660900132>.

FALZON, B.; STEVENS, K.; DAVIES, G. Postbuckling behaviour of a blade-stiffened composite panel loaded in uniaxial compression. **Composites Part A: Applied Science and Manufacturing**, Elsevier, v. 31, n. 5, p. 459–468, may 2000. Disponível em: <http://www.sciencedirect.com/science/article/pii/S1359835X99000858>. 3

Federal Aviation Administration. Aging Airplane Program: Widespread Fatigue Damage; Final Rule. **Federal Register**, v. 75, n. 219, p. 69745–69789, 2010.

FENG, Y.; HE, Y.; AN, T.; CUI, R.; SHAO, Q.; FAN, C. Effect of hygrothermal condition on buckling and post-buckling performance of CCF300/5228A aero composite stiffened panel under axial compression. **Journal of Reinforced Plastics and Composites**, SAGE PublicationsSage UK: London, England, v. 34, n. 12, p. 989–999, jun 2015. Disponível em:
<http://journals.sagepub.com/doi/10.1177/0731684415585381>. 4

FERNANDES, R.; MOURA, M.; MOREIRA, R. Effect of moisture on pure mode I and II fracture behaviour of composite bonded joints. **International Journal of Adhesion and Adhesives**, Elsevier, v. 68, p. 30–38, jul 2016. ISSN 0143-7496. Disponível em: <http://www.sciencedirect.com/science/article/pii/S0143749616300033>. 14

FERNANDES, R.; MOURA, M. de; MOREIRA, R. Effect of temperature on pure modes I and II fracture behavior of composite bonded joints. **Composites Part B: Engineering**, Elsevier, v. 96, p. 35–44, jul 2016. ISSN 1359-8368. Disponível em: <https://www.sciencedirect.com/science/article/pii/S1359836816302633>.

FLOROS, I.; TSERPES, K.; LOBEL, T. Mode-I, mode-II and mixed-mode I+II fracture behavior of composite bonded joints: Experimental characterization and numerical simulation. **Composites Part B: Engineering**, Elsevier, v. 78, p. 459–468, sep 2015. Disponível em:
<http://www.sciencedirect.com/science/article/pii/S1359836815002346>.

FOSTER, S. K.; BISBY, L. A. High Temperature Residual Properties of Externally-Bonded FRP Systems. **American Concrete Institute**, ACI-SP230, n. 7, p. 1235–1252, 2005. Disponível em: <https://www.researchgate.net/profile/Luke_Bisby-/publication/253516910_High_Temperature_Residual_Properties_of_Externally-Bonded_FRP_Systems/links/5416dbe10cf2788c4b35ee57.pdf>.

FOSTER, S. K.; BISBY, L. A. Fire Survivability of Externally Bonded FRP Strengthening Systems. **Journal of Composites for Construction**, v. 12, n. 5, p. 553–561, oct 2008. ISSN 1090-0268. Disponível em: <http://ascelibrary.org/doi/10-.1061/%28ASCE%291090-0268%282008%2912%3A5%28553%29>.

GARDEN, H.; HOLLAWAY, L. Environmental Durability of composites. **Internal report of the university of Surrey**, 1997. 16

GARPELLI, F. **Experimental Characterization of Fatigue Delamination Growth Onset in Composite Joints Tested at Room Temperature Ambient Condition (RTA)**. Tese (Doutorado) — Technological Institute of Aeronautics, 2018. 58

HALLIDAY, S.; BANKS, W.; PETHRICK, R. Dielectric studies of adhesively bonded CFRP/epoxy/CFRP structures - design for ageing. **Composites Science and Technology**, Elsevier, v. 60, n. 2, p. 197–207, feb 2000. Disponível em: <http://www.sciencedirect.com/science/article/pii/S0266353899001116>. ix, 18, 19

HASHIN, Z. Failure Criteria for Unidirectional Fiber Composites. **Journal of Applied Mechanics**, ASME, v. 47, n. 2, p. 329–334, jun 1980. ISSN 0021-8936. Disponível em: <http://dx.doi.org/10.1115/1.3153664>. 113

HASHIN, Z.; ROTEM, A. A fatigue failure criterion for fiber reinforced materials. **Journal of Composite Materials**, v. 7, p. 448–464, 1973. Disponível em: <http://www.dtic.mil/dtic/tr/fulltext/u2/760146.pdf>. 113

Henkel Adhesives. **LOCTITE EA 9695 AERO - Henkel Technical Information**. Disponível em: <http://na.henkel-adhesives.com/product-search-1554-.htm?nodeid=8806582550529msdsLanguage=EN_USselectedTab=technical>. xiii, 6, 32

HESHMATI, M.; HAGHANI, R.; AL-EMRANI, M. Environmental durability of adhesively bonded FRP/steel joints in civil engineering applications: State of the art. **Composites Part B: Engineering**, Elsevier, v. 81, p. 259–275, nov 2015. ISSN 1359-8368. Disponível em: <http://www.sciencedirect.com/science/article/pii/S1359836815004242>. 16

HIGGINS, A. Adhesive bonding of aircraft structures. **International Journal of Adhesion and Adhesives**, v. 20, n. 5, p. 367–376, 2000. ISSN 01437496. 2

HOJO, M.; ANDO, T.; TANAKA, M.; ADACHI, T.; OCHIAI, S.; ENDO, Y. Modes I and II interlaminar fracture toughness and fatigue delamination of CF/epoxy laminates with self-same epoxy interleaf. **International Journal of Fatigue**, Elsevier, v. 28,

n. 10, p. 1154–1165, oct 2006. ISSN 0142-1123. Disponível em: <https://www.sciencedirect.com/science/article/pii/S0142112306000351>. 116

HOLMES, M. Aerospace looks to composites for solutions. **Reinforced Plastics**, v. 61, n. 4, p. 237–241, jul 2017. Disponível em: <http://linkinghub.elsevier.com/retrieve/pii/S0034361717303302>. 1

HU, P.; LUNDQUIST, E.; BATDORF, S. **Effect of small deviations from flatness on effective width and buckling of plates in compression**. Langley Field, 1946. 37

HUTCHINSON, A. R.; HOLLAWAY, L. C. Environmental durability. In: **Strengthening of Reinforced Concrete Structures**. Elsevier, 1999. p. 156–182. ISBN 9781855733787. Disponível em: <http://linkinghub.elsevier.com/retrieve/pii/B9781855733787500101>. 14, 16

IRWIN, G. R. **Onset of fast crack propagation in high strength steel and aluminum alloys**. [S.l.], 1956. 92

IRWIN, G. R. Fracture I - Elasticity and Plasticity. In: FLÜGGE, S. (Ed.). **Encyclopedia of Physics**. Berlin, Heidelberg: Springer Berlin Heidelberg, 1958. p. 551–590. ISBN 978-3-642-45887-3. Disponível em: <https://doi.org/10.1007/978-3-642-45887-3_5>.

JABLONSKI, D. A. Fatigue Crack Growth in Structural Adhesives. **The Journal of Adhesion**, Taylor and Francis Group, v. 11, n. 2, p. 125–143, jan 1980. ISSN 0021-8464. Disponível em: <http://www.tandfonline.com/doi/abs/10.1080/00218468008078911>.

JONES, R. M. R. M. **Buckling of bars, plates, and shells**. [S.l.: s.n.], 2006. 824 p. ISBN 9780978722302. x, 37

KACHANOV, L. M. Time of the rupture process under creep conditions. **Izv. Akad. Nauk. {S.S.R.} Otd. Tech. Nauk.**, v. 8, p. 26–31, 1958. Disponível em: <citeulike-article-id:5466815>.

KARBHARI, V. M.; CHIN, J. W.; HUNSTON, D.; BENMOKRANE, B.; JUSKA, T.; MORGAN, R.; LESKO, J. J.; SORATHIA, U.; REYNAUD, D. Durability Gap Analysis for Fiber-Reinforced Polymer Composites in Civil Infrastructure. **Journal of Composites for Construction**, v. 7, n. 3, p. 238–247, aug 2003. ISSN 1090-0268. Disponível em: <http://ascelibrary.org/doi/10.1061/%28ASCE%291090-0268%282003%297%3A3%28238%29>.
16

KARBHARI, V. M.; GHOSH, K. Comparative durability evaluation of ambient temperature cured externally bonded CFRP and GFRP composite systems for repair of bridges. **Composites Part A: Applied Science and Manufacturing**, v. 40, n. 9, p. 1353–1363, sep 2009. ISSN 1359835X. Disponível em: <http://linkinghub.elsevier.com/retrieve/pii/S1359835X09000189>. 14

KIM, K.-S.; YOO, J.-S.; YI, Y.-M.; KIM, C.-G. Failure mode and strength of uni-directional composite single lap bonded joints with different bonding methods. **Composite Structures**, v. 72, n. 4, p. 477–485, apr 2006. ISSN 02638223. Disponível em: <http://linkinghub.elsevier.com/retrieve/pii/S0263822305000206>. 10

KLUG, J.; WU, X.; SUN, C. T. Efficient modeling of postbuckling delamination growth in composite laminates using plate elements. **AIAA Journal**, American Institute of Aeronautics and Astronautics, v. 34, n. 1, p. 178–184, jan 1996. ISSN 0001-1452. Disponível em: <https://doi.org/10.2514/3.13038>. 96

KONG, C.; LEE, I.; KIM, C.; HONG, C. Postbuckling and failure of stiffened composite panels under axial compression. **Composite Structures**, Elsevier, v. 42, n. 1, p. 13–21, may 1998. Disponível em: <http://www.sciencedirect.com/science/article/pii/S0263822398000440>. 3

KRUEGER, R. Virtual crack closure technique: History, approach, and applications. **Applied Mechanics and Materials**, v. 57, n. 2, p. 109–143, 2004. Disponível em: <http://pages.mtu.edu/~gmodegar/MEEM6130/AMR_2004_109.p>. xi, 29, 95, 96

LAMBERTI, L.; VENKATARAMAN, S.; HAFTKA, R. T.; JOHNSON, T. F. Preliminary design optimization of stiffened panels using approximate analysis models. **International Journal for Numerical Methods in Engineering**, John Wiley and Sons, Ltd., v. 57, n. 10, p. 1351–1380, jul 2003. ISSN 0029-5981. Disponível em: <http://doi.wiley.com/10.1002/nme.781>. ix, 22

LAPLANTE, G.; LEE-SULLIVAN, P. Moisture effects on FM300 structural film adhesive: Stress relaxation, fracture toughness, and dynamic mechanical analysis. **Journal of Applied Polymer Science**, Wiley Subscription Services, Inc., A Wiley Company, v. 95, n. 5, p. 1285–1294, mar 2005. ISSN 0021-8995. Disponível em: <http://doi.wiley.com/10.1002/app.21353>. ix, 14, 19

LI, X.; CHEN, J. The implementation of the extended cohesive damage model for multicrack evolution in laminated composites. **Composite Structures**, Elsevier, v. 139, p. 68–76, apr 2016. Disponível em: <http://www.sciencedirect.com/science/article/pii/S0263822315010971>. 98

LI, X.; CHEN, J. An extended cohesive damage model for simulating arbitrary damage propagation in engineering materials. **Computer Methods in Applied Mechanics and Engineering**, North-Holland, v. 315, p. 744–759, mar 2017. Disponível em: <http://www.sciencedirect.com/science/article/pii/S0045782516316498>. 98

Lin Ye. Role of matrix resin in delamination onset and growth in composite laminates. **Composites Science and Technology**, Elsevier, v. 33, n. 4, p. 257–277, jan 1988. ISSN 0266-3538. Disponível em: <https://www.sciencedirect.com/science/article/pii/0266353888900437>.

LYNCH, C.; MURPHY, A.; PRICE, M.; GIBSON, A. The computational post buckling analysis of fuselage stiffened panels loaded in compression. **Thin-Walled Structures**, Elsevier, v. 42, n. 10, p. 1445–1464, oct 2004. 3, 21

MARKATOS, D. N.; TSERPES, K. I.; RAU, E.; MARKUS, S.; EHRHART, B.; PANTELAKIS, S. The effects of manufacturing-induced and in-service related bonding quality reduction on the mode-I fracture toughness of composite bonded joints for aeronautical use. **Composites Part B: Engineering**, v. 45, n. 1, p. 556–564, feb 2013. ISSN 13598368. Disponível em: <http://linkinghub.elsevier.com/retrieve/pii/S1359836812003836>.

MARTIN, R. H.; DAVIDSON, B. D. Mode II fracture toughness evaluation using four point bend, end notched flexure test. **Plastics, Rubber and Composites**, Taylor and Francis, v. 28, n. 8, p. 401–406, aug 1999. ISSN 1465-8011. Disponível em: <https://doi.org/10.1179/146580199101540565>.

MCBRIERTY, V.; MARTIN, S.; KARASZ, F. Understanding hydrated polymers: the perspective of NMR. **Journal of Molecular Liquids**, v. 80, n. 2-3, p. 179–205, may 1999. ISSN 01677322. Disponível em: <http://linkinghub.elsevier.com/retrieve/pii/S0167732299800075>. 14

MEEKS, C.; GREENHALGH, E.; FALZON, B. Stiffener debonding mechanisms in post-buckled CFRP aerospace panels. **Composites Part A: Applied Science and Manufacturing**, Elsevier, v. 36, n. 7, p. 934–946, jul 2005. Disponível em: <http://www.sciencedirect.com/science/article/pii/S1359835X04003173>. 3

MOHAN, J.; IVANKOVIĆ, A.; MURPHY, N. Mode I fracture toughness of co-cured and secondary bonded composite joints. **International Journal of Adhesion and Adhesives**, v. 51, p. 13–22, jun 2014. ISSN 01437496. Disponível em: <http://linkinghub.elsevier.com/retrieve/pii/S0143749614000542>. 10

MOHAN, J.; IVANKOVIĆ, A.; MURPHY, N. Mixed-mode fracture toughness of co-cured and secondary bonded composite joints. **Engineering Fracture Mechanics**, v. 134, p. 148–167, jan 2015. ISSN 00137944. Disponível em: <http://linkinghub.elsevier.com/retrieve/pii/S0013794414004019>.

MOLENT, L.; FORRESTER, C. **The lead crack concept applied to defect growth in aircraft composite structures**. 2017. 22–26 p. 2

MOURA, M. F. de. Progressive Damage Modelling. In: **Modeling of Adhesively Bonded Joints**. Berlin, Heidelberg: Springer Berlin Heidelberg, 2008. p. 155–182. Disponível em: <http://link.springer.com/10.1007/978-3-540-79056-3_6>. xi, 95, 97, 98

MOURITZ, A. P. Fracture processes of aerospace materials. In: **Introduction to Aerospace Materials**. [s.n.], 2012. p. 428–453. ISBN 9781855739468. Disponível em: <http://linkinghub.elsevier.com/retrieve/pii/B9781855739468500182>. 2

MOURITZ, A. P. Polymers for aerospace structures. In: **Introduction to Aerospace Materials**. [S.l.: s.n.], 2012. p. 268–302. ISBN 9780857095152. 1

MUBASHAR, A.; ASHCROFT, I. a.; CRITCHLOW, G. W.; CROCOMBE, a. D. A Method of Predicting the Stresses in Adhesive Joints after Cyclic Moisture Conditioning. **The Journal of Adhesion**, v. 87, n. 9, p. 926–950, 2011. ISSN 0021-8464. Disponível em: <http://www.tandfonline.com/doi/abs/10.1080/00218464.2011.600675>. 15, 16

NIU, M. C.-Y. **Airframe Structural Design : Practical Design Information And Data On Aircraft Structures**. 8. ed. Hong Kong: Conmilit Press Ltd., 1995. ISBN 9627128090. Disponível em: <http://cataleg.upc.edu/record=b1275940˜>. 3, 21

OLGIN, S. L.; BRONDSTED, P.; ZANGENBERG, J. Composite materials: constituents, architecture and generic damage. In: TALREJ, R.; VARNA, J. (Ed.). **Modeling Damage, Fatigue and Failure of Composite Materials**. 1st. ed. [S.l.]: Woodhead Publishing, 2015. cap. Composite, p. 3–21. ISBN 9781782422860. 1

OLIVEIRA, L. A. de. **Fatigue-driven delamination modelling in composite aerostructures**. Tese (Doutorado) — Instituto Tecnologico de Aeronautica, 2018. 29, 30, 100, 102, 103

ORIFICI, A.; Ortiz de Zarata Alberdi, I.; THOMSON, R.; BAYANDOR, J. Compression and post-buckling damage growth and collapse analysis of flat composite stiffened panels. **Composites Science and Technology**, Elsevier, v. 68, n. 15-16, p. 3150–3160, dec 2008. Disponível em: <http://www.sciencedirect.com/science/article/pii/S0266353808002716>. ix, 3, 22, 24, 28

PACKHAM, D. E. D. E. **Handbook of adhesion**. [S.l.]: John Wiley and Sons, 2005. 638 p. ISBN 0470014210. 46

PANTELAKIS, S.; TSERPES, K. I. Adhesive bonding of composite aircraft structures: Challenges and recent developments. **Science China Physics, Mechanics and Astronomy**, v. 57, n. 1, p. 2–11, 2014. ISSN 1869-1927. Disponível em: <https://doi.org/10.1007/s11433-013-5274-3>. 4

PARIS, P.; ERDOGAN, F. A Critical Analysis of Crack Propagation Laws. **Journal of Basic Engineering**, American Society of Mechanical Engineers, v. 85, n. 4, p. 528, dec 1963. ISSN 00219223. Disponível em: <http://fluidsengineering.asmedigitalcollection-.asme.org/article.aspx?articleid=1431537>. 93

PASCOE, J.; ALDERLIESTEN, R.; BENEDICTUS, R. Methods for the prediction of fatigue delamination growth in composites and adhesive bonds - A critical review. **Engineering Fracture Mechanics**, v. 112-113, p. 72–96, 2013. ISSN 00137944. Disponível em: <http://linkinghub.elsevier.com/retrieve/pii/S0013794413003214>. 29, 30, 93, 94, 96, 97, 98

PAULO, R.; TEIXEIRA-DIAS, F.; VALENTA, R. Numerical simulation of aluminium stiffened panels subjected to axial compression: Sensitivity analyses to initial geometrical imperfections and material properties. **Thin-Walled Structures**, Elsevier, v. 62, p. 65–74, jan 2013. Disponível em: <http://www.sciencedirect.com/science/article/pii/S0263823112002273>. ix, 22

PEERLINGS, R. H. J.; BREKELMANS, W. A. M.; BORST, R. de; GEERS, M. G. D. Gradient-enhanced damage modelling of high-cycle fatigue. **International Journal for Numerical Methods in Engineering**, Wiley-Blackwell, v. 49, n. 12, p. 1547–1569, dec 2000. ISSN 0029-5981. Disponível em: <http://doi.wiley.com/10.1002/1097-0207%2820001230%2949%3A12%3C1547%3A%3AAID-NME16%3E3.0.CO%3B2-D>.

PICKERING, K.; EFENDY, M. A.; LE, T. A review of recent developments in natural fibre composites and their mechanical performance. **Composites Part A: Applied Science and Manufacturing**, v. 83, p. 98–112, apr 2016. ISSN 1359835X. Disponível em: <http://linkinghub.elsevier.com/retrieve/pii/S1359835X15003115>. 14

POURSARTIP, A.; CHINATAMBI, N. Fatigue Damage Development in Notched (0/45) Laminates. In: **Composite Materials: Fatigue and Fracture, Second Volume**.

100 Barr Harbor Drive, PO Box C700, West Conshohocken, PA 19428-2959: ASTM International, 1989. p. 45–65. Disponível em: <http://www.astm.org/doiLink.cgi?STP10408S>. 29, 92

PRAMANIK, A.; BASAK, A. K.; DONG, Y.; SARKER, P. K.; UDDIN, M. S.; LITTLEFAIR, G.; DIXIT, A. R.; CHATTOPADHYAYA, S. Joining of carbon fibre reinforced polymer (CFRP) composites and aluminium alloys - A review. **Composites Part A: Applied Science and Manufacturing**, Elsevier Ltd, v. 101, p. 1–29, 2017. ISSN 1359835X. Disponível em: <http://dx.doi.org/10.1016/j.compositesa.2017.06.007>. 1, 2

RABOTNOV, Y. N. Creep rupture. In: **Applied Mechanics**. Berlin, Heidelberg: Springer Berlin Heidelberg, 1969. p. 342–349. Disponível em: <http://link.springer.com/10.1007/978-3-642-85640-2_26>.

RANA, S.; FANGUEIRO, R.; NUNES, J. **1 - Advanced composites in aerospace engineering**. Elsevier Ltd, 2016. 1–15,129–174 p. ISBN 9780081009390. Disponível em: <http://dx.doi.org/10.1016/B978-0-08-100037-3.00001-8>. 1

RATWANI, M. M.; KANT, H. P. Compression Fatigue Analysis of Fiber Composites. **Journal of Aircraft**, v. 18, n. 6, p. 458–462, 1981. Disponível em: <https://arc.aiaa.org/doi/pdf/10.2514/3.57512>.

RINDERKNECHT, S.; KROPLIN, B. A computational method for the analysis of delamination growth in composite plates. **Computers \& Structures**, Pergamon, v. 64, n. 1-4, p. 359–374, jul 1997. Disponível em: <http://www.sciencedirect.com/science/article/pii/S0045794996001277>. 96

ROBINSON, P.; GALVANETTO, U.; TUMINO, D.; BELLUCCI, G.; VIOLEAU, D. Numerical simulation of fatigue-driven delamination using interface elements. **International Journal for Numerical Methods in Engineering**, Wiley-Blackwell, v. 63, n. 13, p. 1824–1848, aug 2005. ISSN 0029-5981. Disponível em: <http://doi.wiley.com/10.1002/nme.1338>.

ROMEO, G.; FRULLA, G. Post-buckling behaviour of graphite/epoxy stiffened panels with initial imperfections subjected to eccentric biaxial compression loading. **International Journal of Non-Linear Mechanics**, Pergamon, v. 32, n. 6, p. 1017–1033, nov 1997. Disponível em: <http://www.sciencedirect.com/science/article/pii/S0020746296001369>. 37

SCIOLTI, M. S.; FRIGIONE, M.; AIELLO, M. A. Wet Lay-Up Manufactured FRPs for Concrete and Masonry Repair: Influence of Water on the Properties of Composites and on Their Epoxy Components. **Journal of Composites for Construction**, v. 14, n. 6, p. 823–833, dec 2010. ISSN 1090-0268. Disponível em: <http://ascelibrary.org/doi/10.1061/%28ASCE%29CC.1943-5614.0000132>. 14, 15

SHIVAKUMAR, K. N.; PANDURANGA, R.; SHARPE, M. Interleaved Polymer Matrix Composites: A Review. In: **54th AIAA/ASME/ASCE/AHS/ASC Structures, Structural Dynamics, and Materials Conference**. Reston, Virginia: American Institute of Aeronautics and Astronautics, 2013. ISBN 978-1-62410-223-3. Disponível em: <http://arc.aiaa.org/doi/10.2514/6.2013-1903>. 31

SILVA, L. F. M. da; CAMPILHO, R. D. S. G. **Advances in Numerical Modeling of Adhesive Joints**. Berlin, Heidelberg: Springer Berlin Heidelberg, 2012. (SpringerBriefs in Applied Sciences and Technology). ISBN 978-3-642-23607-5. Disponível em: <http://link.springer.com/10.1007/978-3-642-23608-2>. 29, 30, 92, 97, 98

SILVA, L. F. M. da; ÖCHSNER, A.; ADAMS, R. D. Introduction to Adhesive Bonding Technology. In: **Handbook of Adhesion Technology**. Berlin, Heidelberg: Springer Berlin Heidelberg, 2011. p. 1–7. ISBN 978-3-642-01169-6. 1

SINGER, J.; ARBOCZ, J.; WELLER, T. **Buckling experiments : experimental methods in buckling of thin-walled structures**. [S.l.]: Wiley, 1998. 1732 p. ISBN 9780471956617. 37

SONG, M.-G.; KWEON, J.-H.; CHOI, J.-H.; BYUN, J.-H.; SONG, M.-H.; SHIN, S.-J.; LEE, T.-J. Effect of manufacturing methods on the shear strength of composite single-lap bonded joints. **Composite Structures**, v. 92, n. 9, p. 2194–2202, aug 2010. ISSN 02638223. Disponível em: <http://linkinghub.elsevier.com/retrieve/pii/S026382230900333X>. 2, 4, 9, 10, 11

STEVENS, K.; RICCI, R.; DAVIES, G. Buckling and postbuckling of composite structures. **Composites**, Elsevier, v. 26, n. 3, p. 189–199, mar 1994. Disponível em: <http://www.sciencedirect.com/science/article/pii/001043619591382F>. 3, 28

SUN, S.; LI, M.; LIU, A. A review on mechanical properties of pressure sensitive adhesives. **International Journal of Adhesion and Adhesives**, Elsevier, v. 41, p. 98–106, mar 2013. ISSN 0143-7496. Disponível em: <https://www.sciencedirect.com/science/article/pii/S0143749612001601>. 2

TORAY. **Composite Materials Research Laboratories**. Disponível em: <http://www.toray.com/technology/organization/laboratories/lab_004.html>. xiii, 31

TORAY. **3900 Prepreg System**. [S.l.], 2017. Disponível em: <https://www.toraycma.com/file_viewer.php?id=4866>. xiii, 6, 31

TRAN, K. L.; DOUTHE, C.; SAB, K.; DALLOT, J.; DAVAINE, L.; DOUTHE, C.; SAB, K. Buckling of stiffened curved panels under uniform axial compression. **Journal of Constructional Steel Research**, Elsevier, v. 103, 2014. Disponível em: <https://hal.archives-ouvertes.fr/hal-01073382/document>. 23

Van Rijn, J. C. F. N.; WIGGENRAAD, J. F. M. A seven-point bending test to determine the strength of the skin-stiffener interface in composite aircraft panels. 2000. Disponível em: <https://reports.nlr.nl/xmlui/bitstream/handle/10921/815/TP-2000-044.pdf?sequence=1>.
106

VESCOVINI, R.; DAVILA, C.; BISAGNI, C. Failure analysis of composite multi-stringer panels using simplified models. **Composites Part B: Engineering**, Elsevier, v. 45, n. 1, p. 939–951, feb 2013. ISSN 1359-8368. Disponível em: <http://www.sciencedirect.com/science/article/pii/S1359836812004817>. 3

VIANA, G.; COSTA, M.; BANEA, M.; SILVA, L. da. A review on the temperature and moisture degradation of adhesive joints. **Proceedings of the Institution of Mechanical Engineers, Part L: Journal of Materials: Design and Applications**, SAGE PublicationsSage UK: London, England, sep 2016. ISSN 1464-4207. Disponível em: <http://pil.sagepub.com/lookup/doi/10.1177/1464420716671503>. 14

WANG, X.; CAO, W.; DENG, C.; WANG, P.; FUE, Z. Experimental and numerical analysis for the post-buckling behavior of stiffened composite panels with impact damage. **Composite Structures**, Elsevier, v. 133, p. 840–846, dec 2015. Disponível em: <http://www.sciencedirect.com/science/article/pii/S0263822315006960>. 3

YAP, J.; SCOTT, M.; THOMSON, R.; HACHENBERG, D. The analysis of skin-to-stiffener debonding in composite aerospace structures. **Composite Structures**, Elsevier, v. 57, n. 1-4, p. 425–435, jul 2002. Disponível em: <http://www.sciencedirect.com/science/article/pii/S0263822302001101>. ix, 3, 21, 22, 23, 24, 27, 28

YAP, J.; THOMSON, R.; SCOTT, M.; HACHENBERG, D. Influence of post-buckling behaviour of composite stiffened panels on the damage criticality. **Composite Structures**, Elsevier, v. 66, n. 1-4, p. 197–206, oct 2004. 21, 22

YU, R. C.; PANDOLFI, A. Modeling of delamination fracture in composites: a review. In: **Woodhead Publishing Series in Composites Science and Engineering**. Woodhead Publishing, 2008. p. 429–457. ISBN 978-1-84569-244-5. Disponível em: <https://www.sciencedirect.com/science/article/pii/B9781845692445500158>. 96

ZHAO, W.; KAPANIA, R. Buckling analysis of unitized curvilinearly stiffened composite panels. **Composite Structures**, Elsevier, v. 135, p. 365–382, jan 2016. Disponível em: <http://www.sciencedirect.com/science/article/pii/S0263822315008879>. 3

Appendix A - Progressive damage growth models

As was stated in section 2.4 progressive damage models can be divided in four techniques. All of which will be treated below:

- Stress/strain based methods (section A.1)
- Fracture mechanics based methods (section A.2)
- Cohesive zone models (CZMs) (section A.3)
- Extended finite element method (XFEM) based models (section A.4)

A.1 Stress/strain based methods

Pascoe et al. (2013) state that stress/strain based methods are more suitable for fatigue life predictions than for actual delamination growth modeling. However, several authors such as Ratwani and Kant (1981) and Poursartip and Chinatambi (1989) still have successfully used them to predict delamination growth. Ratwani and Kant (1981) state that the delamination growth rate $\frac{da}{dN}$ can be predicted by:

$$\frac{da}{dN} = C\left(\tau_{max} - \tau_{min} - \tau_{th}\right)^n a^m \tag{A.1}$$

Where τ_{max} and τ_{min} are the maximum and minimum shear stress due to the cyclic loading and τ_{th} is a threshold value below which no delamination occurs. C, n and m are fitting parameters. The authors point out that, because delamination is a type of crack growth, m can be assumed to be 0.5n. This assumption makes the equation essentially fracture mechanics based, as the stress can be rewritten to the stress intensity factor K. With $K = \sigma\sqrt{\pi a}$.

The model proposed by Poursartip and Chinatambi (1989) is truly stress based. The equation relating delamination growth to the applied stress cycle is given by:

$$\frac{da}{dN} = C\left(\frac{1+R}{1-R}\right)^m (\triangle\sigma)^n \tag{A.2}$$

Where R is the stress ratio equal to $\frac{\sigma_{min}}{\sigma_{max}}$ and $\triangle\sigma$ the stress amplitude $\sigma_{max} - \sigma_{min}$. This equation is a function of both the mean stress and the stress range, with the mean stress equal to [Poursartip e Chinatambi 1989]:

$$\sigma_{mean} = \frac{1+R}{2-2R}\triangle\sigma \tag{A.3}$$

In the same article, Poursartip and Chinatambi (1989), also use an equation similar to A.2, but based on fracture mechanics:

$$\frac{da}{dN} = C\left(\frac{1+R}{1-R}\right)^m (\triangle G)^n \tag{A.4}$$

The results for both methods were very similar. The authors state that this is because the compliance change of the specimen was constant over the entire crack length. Pascoe et al. (2013) state that to be certain of the correctness of this stress bases model, it has to be tested on a specimen with a non constant compliance change. They mention that until that has been shown, there is no proof that stress by itself is a sufficient parameter to predict delamination growth.

The main advantage of stress/strain based models is their intuitive usage. They originate from the same principles as those used in static failure criteria and are therefore easy to implement. However, analytical calculation of the stress in a cracked structure is complicated by the stress singularity at the crack tip [Anderson 1995]. This also limits the use of stress based approaches in FEM, due to the great mesh dependency of the stress at the crack tip [Silva e Campilho 2012]. This in combination with the lack of proven models available in literature make stress/strain based models currently not readily applicable to predict disbond growth.

A.2 Fracture mechanics based methods

This section first explains the basic principles of fracture mechanics based numerical models and subsequently discusses a popular technique of obtaining the SERR for FEM: VCCT.

A.2.1 Basic principles

Fracture mechanics based methods predict delamination growth using either the stress intensity factor (SIF) K or strain energy release rate (SERR) G. The SERR is a measure of the energy available for an increment of crack extension and is given by [Irwin 1956, Anderson 1995]:

$$G = -\frac{d\Pi}{dA} \tag{A.5}$$

Where Π is the potential energy supplied by the internal strain energy and external forces and A is the crack area. In a mixed-mode problem the SIF can be related to the

SERR using [Anderson 1995]:

$$G = \frac{K_I^2}{E'} + \frac{K_{II}^2}{E'} + \frac{K_{III}^2}{2\mu} \tag{A.6}$$

Where K_I, K_{II} and K_{III} are the stress intensity factors in mode I, II and III respectively and μ is the shear modulus. E' is given by [Anderson 1995]:

$$\begin{aligned} E' &= E && \text{for plane stress} \\ E' &= \frac{E}{1-\nu} && \text{for plane strain} \end{aligned} \tag{A.7}$$

Where E is the Young's modulus and ν Poisson's ratio. In essence almost all fracture based delamination growth models stem from the Paris law and are based on either the SIF or SERR [Pascoe *et al.* 2013]. The original form of Paris' law describes crack growth as a function of the SIF [Paris e Erdogan 1963]:

$$\frac{da}{dN} = C \triangle K^n \tag{A.8}$$

Paris and Erdorgan (1963) originally stated that n was equal to four. However, later research proved that n is a fitting parameter which is different for every material. The fitting parameters C and n are assumed to be material constants and can be obtained by performing a series of propagation tests on coupon level for which $\triangle K$ is known.

Although G and K are essentially interchangable, as shown in equation A.6, for composites the Paris law is generally written in terms of the SERR. This is because the inhomogeneous nature of composites makes it hard to determine the SIF at the crack tip. The SERR can be obtained relatively easy by measuring the change of compliance with crack length using [Anderson 2005]:

$$G = \frac{P^2}{2W} \frac{dB}{da} \tag{A.9}$$

Where W is the width of the specimen, P the load and B the specimen thickness. When written in terms of SERR Paris' law becomes [Pascoe *et al.* 2013]:

$$\frac{da}{dN} = Cf(G)^n \tag{A.10}$$

In which the function of G is generally either $\triangle G$ or G_{max} [Pascoe *et al.* 2013]. Nowadays, many different versions of the Paris law exist because the original form is not capable of describing the delamination growth for every value of f(G). When looking at figure A.1 it can be seen that delamination growth can be divided into three regions. Region one is dominated by the threshold below which no fatigue crack growth occurs, region two can be described using Paris' law and region three is strongly dependent on the ratio of loading R [Anderson 2005].

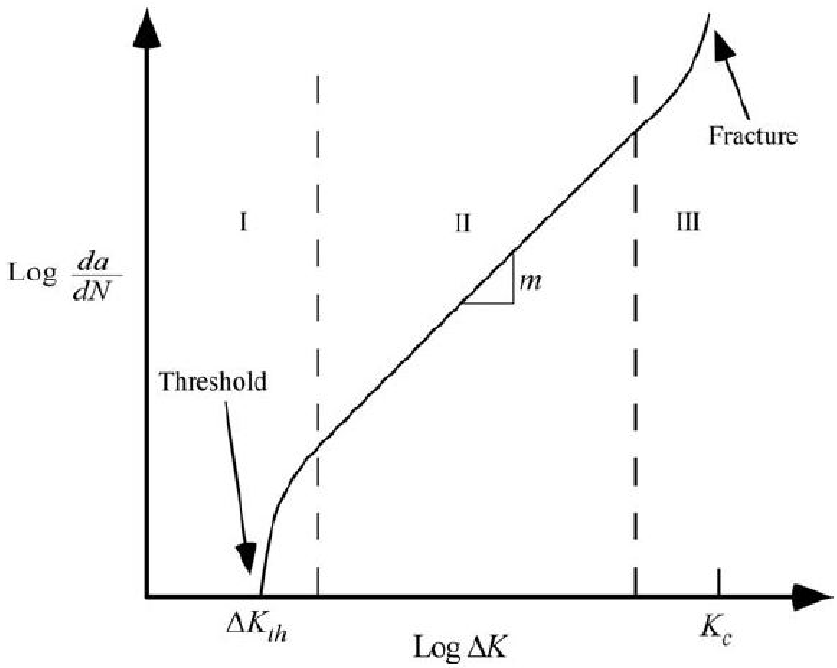

FIGURE A.1 – Paris curve showing the sigmoidal behavior of the delamination growth rate [Anderson 1995]

To capture the crack growth in other regions of the crack growth, as well as region 2, different variations of the Paris law were developed. An extensive overview of the different Paris law based models available can be found in a review by Pascoe et al. (2013). For the sake of this subsection it is sufficient to note that there is currently no consensus on which version of the Paris law is most suitable for disbond growth, as well as what the function of G (f(G) in equation A.10) represents exactly. Pascoe et al. (2013) state that $\triangle G$, and G_{max} are both frequently used without one having an obvious edge over the other. They also point out that the difference is often marginally small, as $\frac{G_{min}}{G_{max}}$ is proportional to the square of the load ratio (R^2) and for R=0.1 the difference would thus only be 1%.

Additionally, the right definition of G_{min} is a point of discussion. Instinctively the lowest SERR in the loading cycle comes to mind. However, as Jablonski (1980) pointed out G_{th} might be more appropriate in some scenarios. With the threshold being the value at which crack opening takes place. Both G_{min} and G_{th} have been applied successfully in literature and the argument to choose either one seems to be case dependent [Pascoe *et al.* 2013].

Fracture mechanics based models have received more attention in research than stress strain based methods to predict disbond growth. This well established nature is a clear advantage. Another positive point is that the SERR is already known for many test set-ups, or can be determined experimentally. Based on cyclic crack growth experiments a form of the Paris law can be fitted and subsequently used for the prediction of crack growth in real life applications.

A.2.2 Virtual crack closure technique

The virtual crack closure technique is the most widely used numerical method for obtaining the SERR in laminated composite materials [Krueger 2004]. Other methods to obtain the SERR, such as the finite crack extension method, virtual crack extension method and the equivalent domain integral method, have also been applied in literature with various success [Krueger 2004, Banks-Sills 2010]. However, due to their limited use they will not be covered here.

The virtual crack closure technique is based on the work performed by Irwin (1958) on the crack closure integral. He stated that the energy released ($\triangle U$) when a crack is extended by a certain amount ($\triangle a$) is the same as the energy required to close the crack over that length. With $\triangle U$, for the 2D situation as depicted in figure A.2, equal to [Moura 2008, Krueger 2004]:

$$\triangle U = \frac{1}{2}\left(X_i \triangle u_l + Y_i \triangle v_l\right) \tag{A.11}$$

Where X_i and Y_i represent the loads at the closed node i and $\triangle u_l$ and $\triangle v_l$ the difference in displacement between nodes l_1 and l_2. The VCCT assumes that extension of the crack with $\triangle a$ does not alter the crack tip significantly [Krueger 2004]. This allows the assumption that, upon crack extension from $a + \triangle a$ to $a + 2\triangle a$, the amount of crack opening at node i will be equal to what it was at node l for a crack length $a + \triangle a$.

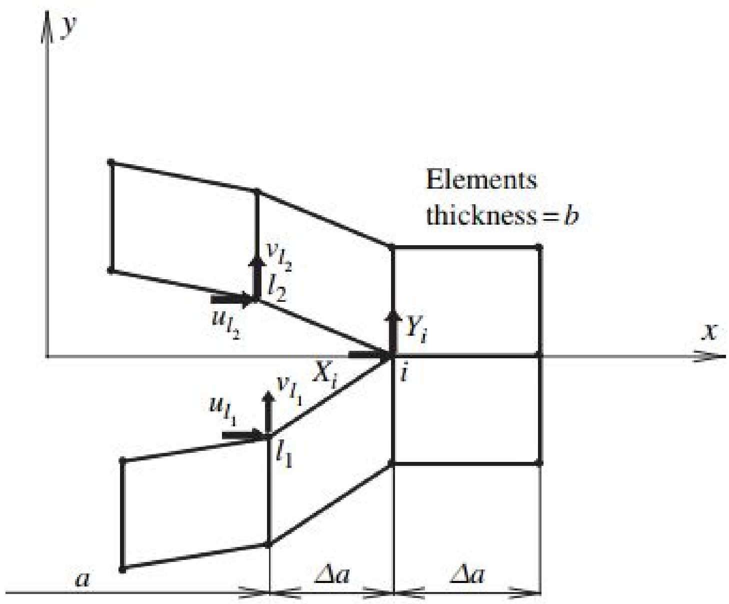

FIGURE A.2 – 2D representation of crack growth in the virtual crack closure technique [Moura 2008]

The equations to calculate the strain energy release rate using the VCCT are element dependent. Generally, using more nodes results in more extensive equations. For illustrative purposes below the equations to calculate the SERR at the corner nodes of a four noded rectangular plate element, as displayed in figure A.3, are given [Krueger 2004]:

$$
\begin{aligned}
G_I &= -\frac{1}{2\triangle A} Z_{Li}(\triangle w_l) \\
G_{II} &= -\frac{1}{2\triangle A} X_{Li}(\triangle u_l) \\
G_{III} &= -\frac{1}{2\triangle A} Y_{Li}(\triangle v_l)
\end{aligned}
\tag{A.12}
$$

Where $\triangle A$ is the area of the damaged front as shown in figure A.3: $\triangle A = \frac{\triangle a(b_1+b_2)}{2}$. Z_{Li} is the additional force and $\triangle w_l$ the additional displacement difference arising from the transformation to 3D with respect to equation A.11.

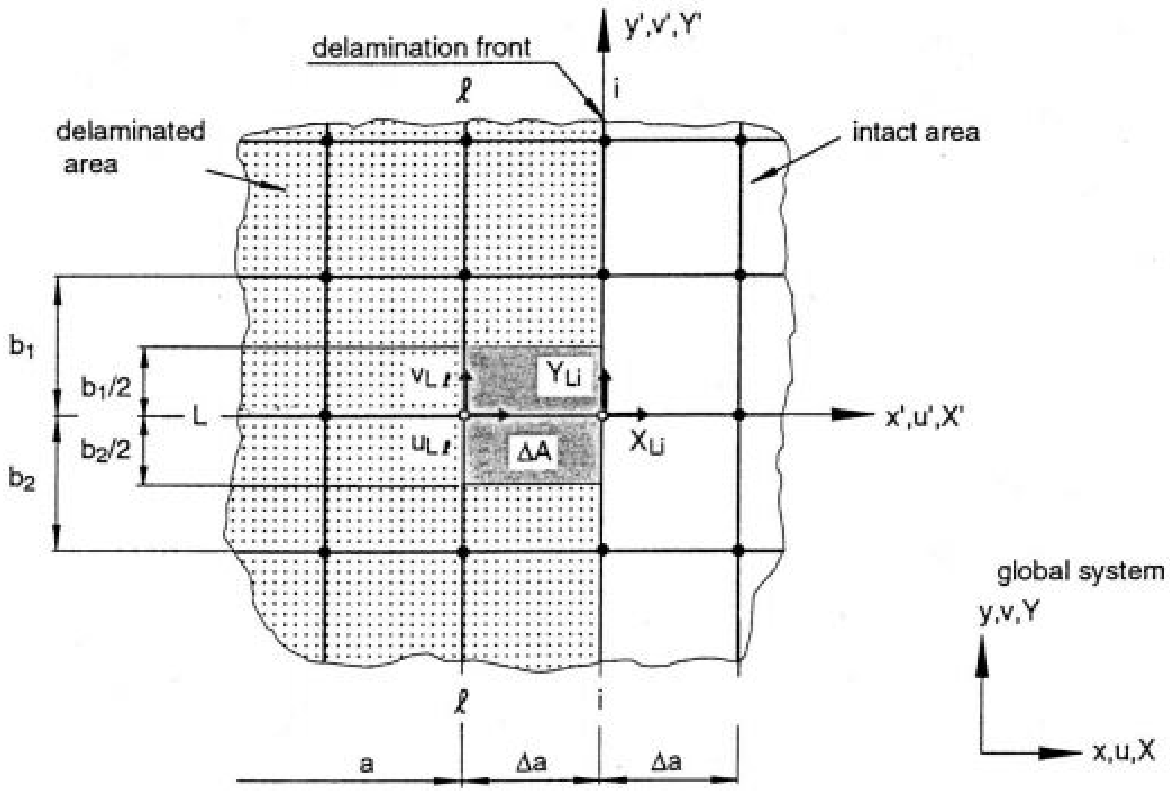

FIGURE A.3 – 2D view of the upper surface of cracking for 4 node plates [Krueger 2004]

VCCT is a straightforward method to obtain the SERR. It has already been successfully applied to predict quasi-static delamination due to buckling in composites [Rinderknecht e Kroplin 1997, Klug *et al.* 1996]. One of the disadvantages associated with the VCCT is that the mixed-mode ratio is undefined when the virtual crack length $\triangle a$ at a bimaterial interface goes to zero [Krueger 2004]. This causes stress oscillations near the crack tip and can result in incorrect values for G_I, G_{II} and G_{III}. Furthermore, VCCT is not capable of crack initiation and requires re-meshing after crack advancement in progressive damage modelling [Pascoe *et al.* 2013]. This makes VCCT models inefficient for the prediction of delamination growth [Yu e Pandolfi 2008].

A.3 Cohesive zone modeling

Cohesive zone models (CZM) are based on the early work by Barenblatt (1959, 1962) towards the formation of cracks in brittle materials and Dugdale (1960) towards the yielding of steel plates with slits. Cohesive elements are used at the interfaces where delamination is expected to occur [Pascoe *et al.* 2013, Budhe *et al.* 2017]. A damage parameter D is then used to progressively reduce the stiffness of these elements to zero [Pascoe *et al.* 2013, Silva e Campilho 2012].

The way the stiffness is being reduced depends on the traction-separation law. Different variations of the traction-separation law exist and the selection of one should be based on the material/interface behavior [Silva e Campilho 2012]. Bilinear laws, such as the on given in figure A.4, typically work well for brittle materials [Silva e Campilho 2012, Moura 2008]. Whereas trapezoidal laws are more suitable for ductile materials [Silva e Campilho 2012, Moura 2008].

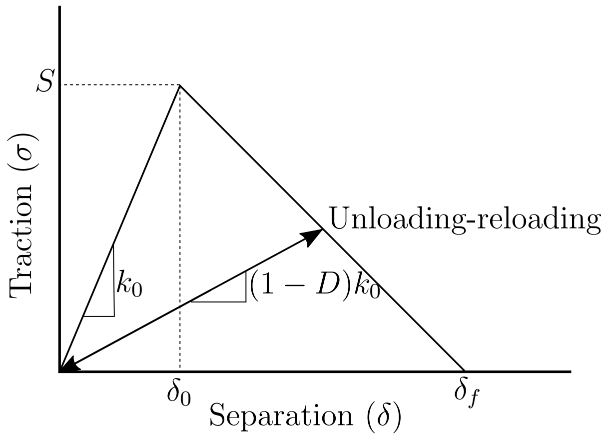

FIGURE A.4 – Bilinear traction–separation law

The constitutive behavior belonging to such a traction separation law can be written as [Pascoe *et al.* 2013]:

$$\begin{aligned} \sigma_i &= k_i\delta_i && \text{if} \quad 0 \le \kappa_i \le \delta_{i,0} \\ \sigma_i &= (1-D_i)k_i\delta_i && \text{if} \quad \delta_{i,0} \le \kappa_i \le \delta_{i,f} \\ \sigma_i &= 0 && \text{if} \quad \delta_{i,f} \le \kappa_i \end{aligned} \tag{A.13}$$

Where:
σ_i : Stress in direction i
k : Stiffness of the element
$\delta(t)$: Relative displacement of the faces of the element at pseudo time t
$\kappa(t)$: Maximum relative displacement of the faces of the element at any time ($max_{0\le t}\delta_i(t)$)
δ_0 : Relative displacement of the faces of the element at the onset of softening
δ_f : Relative displacement of the faces of the element at failure

An important advantage of CZM is the fact that re-meshing is not necessary upon crack propagation. Furthermore, it is not necessary to have an initial crack present in the model [Moura 2008, Budhe *et al.* 2017]. Although this is not particularly relevant for this research, as a pre-crack is already present. Moreover, CZM is currently the most widespread method for predicting static and fatigue damage in structures [Silva e Campilho 2012]. Resulting in a well researched and relatively mature technique. A disadvantage is the fact that it is required to know the crack path a priori, as cohesive elements have to be placed along this path.

A.4 The extended finite element method

The extended finite element method is able to overcome one of the most important disadvantages of cohesive zone models and the VCCT: the requirement to pre-define a crack path. In XFEM virtual nodes complement the regular nodes of the elements. The displacement between the virtual nodes and regular nodes is then prescribed by enrichment functions, allowing internal discontinuity within elements and thus crack growth anywhere in an object [Budhe *et al.* 2017, Li e Chen 2016, Pascoe *et al.* 2013].

XFEM can be used in combination with damage parameter based models, such as CZM, to gradually model damage within elements. An example of such an approach is the extended cohesive damage model (ECDM) developed by Li and Chen (2017). They used a principle stress based criterion for crack initiation and propagation. It was shown that this approach showed good correlation with experimental results for different quasi-static crack growth problems.

Although XFEM is seen as a promising technique [Campilho *et al.* 2011, Li e Chen 2017], it is not considered a viable option for the fatigue disbond modelling for this research. Mainly because, even though XFEM is currently an active field of work, the performed research towards fatigue related delamination is limited. Additionally, problems exist in the potential mesh dependency of XFEMs. Campilho et al. (2011) showed that a very fine mesh was required to obtain similar results for crack propagation in single lap joints using XFEM, as opposed to CZM. Thus resulting in significantly higher computational costs.

Appendix B - Explanation of the VUMAT

It is advised to have a certain level of knowledge on cohesive zone models before reading this chapter. The recommended prior knowledge can be obtained from section A.3. The VUMAT developed by Oliveira (2018) will be explained in three parts. First the kinematics of the elements will be explained in section B.1. Subsequently, section B.2 will touch briefly upon the constitutive law. Finally, the damage evolution is explained in section B.3.

B.1 Kinematics

The VUMAT uses 8 node brick elements with reduced integration as interface elements. These elements are placed along the expected crack path to allow local damage growth. The kinematics are defined in terms of relative displacement between the upper and lower surfaces of the elements. The relative displacement vector $\{\delta\}$ is composed of one normal (w) and two tangent (u, v) displacements, which can be seen in figure B.1a.

The relative displacement vector can be obtained using [Bürger *et al.* 2012]:

$$\begin{aligned}\{\delta\}^T = \{u \quad v \quad w\}^T &= \{h\gamma_{xz} \quad h\gamma_{yz} \quad h\epsilon_{zz}\}^T \\ &\rightarrow u = u_t - u_b \\ &\rightarrow v = v_t - v_b \\ &\rightarrow w = w_t - w_b\end{aligned} \tag{B.1}$$

Where the subscripts t and b are the top and bottom as defined in figure B.1a and h is the element thickness. γ is the shear strain. The subroutine uses an equivalent relative displacement $\bar{\delta}$ which can be defined under mixed mode loading as in figure B.1b [Bürger *et al.* 2012]:

$$\bar{\delta} = \sqrt{w^2 + u^2 + v^2} \tag{B.2}$$

Or the other way around using the definitions of figure B.1b:

$$\begin{aligned}u &= \bar{\delta}\sin(\beta)\cos(\alpha) \\ v &= \bar{\delta}\sin(\beta)\sin(\alpha) \\ w &= \bar{\delta}\cos(\beta)\end{aligned} \tag{B.3}$$

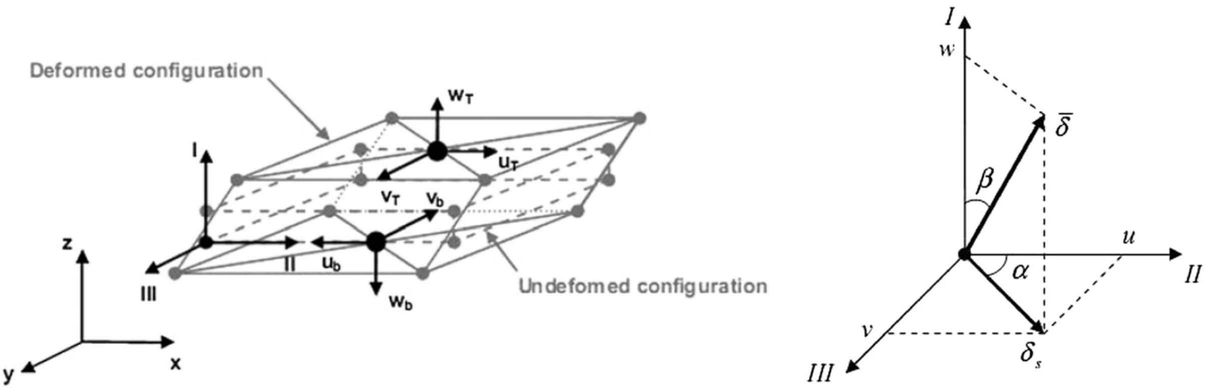

(a) Overview of the 8 node brick elements [Bürger *et al.* 2012] (b) Relative displacement definition [Bürger *et al.* 2012]

FIGURE B.1 – Kinematics of the 8 node brick element used to model the cohesive interface

B.2 Constitutive law

The constitutive law describing the traction-separation relation between the cohesive interface and the adjacent layers uses a single damage variable (D) to describe the stiffness degradation in all three fracture modes. A diagonal stiffness matrix is used to uncouple the stresses in all three directions. The constitutive behavior is then given by [Bürger *et al.* 2012]:

$$\begin{Bmatrix} \sigma_I \\ \sigma_{II} \\ \sigma_{III} \end{Bmatrix} = \begin{bmatrix} k_I\left(1 - D(\bar{\delta})\right) & 0 & 0 \\ 0 & k_{II}\left(1 - D(\bar{\delta})\right) & 0 \\ 0 & 0 & k_{III}\left(1 - D(\bar{\delta})\right) \end{bmatrix} \begin{Bmatrix} w \\ u \\ v \end{Bmatrix} \tag{B.4}$$

In which the stiffness terms k are given by:

$$\begin{aligned} k_I &= \frac{E_{zz}}{h} \\ k_{II} &= \frac{G_{xz}}{h} \\ k_{III} &= \frac{G_{yz}}{h} \end{aligned} \tag{B.5}$$

B.3 Damage evolution

The damage variable D for a given element consists of static (D^s) and fatigue damage (D^f) [Oliveira 2018]:

$$D = D^s + D^f \tag{B.6}$$

Both will be treated separately in subsections B.3.1 and B.3.2.

B.3.1 Static damage

The static damage evolution is based on the work by Bürger et al. (2012) and is represented by a bilinear traction-separation law, as was presented in figure A.4. For a mixed mode fracture situation the bilinear traction-separation is in terms of equivalent displacement and equivalent stress ($\bar{\sigma}$), as displayed in figure B.2. Before the damage for a given equivalent displacement can be calculated, the equivalent damage onset displacement and equivalent displacement at failure have to be known.

Relative displacement at damage onset

Oliveira (2018) uses the quadratic stress based criterion proposed by Ye (1988) to determine the equivalent relative displacement at damage onset:

$$\left(\frac{\langle\sigma_I\rangle}{S_I}\right)^2 + \left(\frac{\sigma_{II}}{S_{II}}\right)^2 + \left(\frac{\sigma_{III}}{S_{III}}\right)^2 = 1 \tag{B.7}$$

Where the Macaulay brackets indicate that for mode I damage only occurs in the tensile stress state. This is not relevant for shear stresses. Combining the constitutive law of equation B.4 and the relative displacement definitions of equation B.3, equation B.7 can be rewritten to an equivalent relative displacement after which damage starts to accumulate [Bürger *et al.* 2012]:

$$\bar{\delta}_0 = \left[\left(\frac{\langle k_I\cos(\beta)\rangle}{S_I}\right)^2 + \left(\frac{k_{II}\sin(\beta)\cos(\alpha)}{S_{II}}\right)^2 + \left(\frac{k_{III}\sin(\beta)\sin(\alpha)}{S_{III}}\right)^2\right]^{-\frac{1}{2}} \tag{B.8}$$

Relative displacement at failure

The relative displacement at failure for a given mixed mode ratio is calculated using a strain energy release rate based criterion developed by Benzeggagh and Kenane (1996). They state that the equivalent fracture toughness for a given mixed mode ratio is equal to:

$$\bar{G}_c = G_{Ic} + (G_{IIc} - G_{Ic})\phi^\eta \tag{B.9}$$

Where η is the B-K interpolation parameter based on fitting after mixed mode testing and ϕ is given by:

$$\phi = \frac{G_{II} + G_{III}}{G_I + G_{II} + G_{III}} \tag{B.10}$$

This criterion is often referred to as the B-K criterion. It has to be noted that the mode III fracture toughness is assumed to be the same as mode II. To be able get the equivalent displacement at fracture from this criterion the fracture toughness has to be written as a combination of strength and relative displacement at failure [Bürger *et al.* 2012]:

$$G_{Ic} = \int_0^{w_f} \sigma_I \; dw = \frac{S_I w_f}{2} = \frac{k_I\bar{\delta}_0\cos^2(\beta)\bar{\delta}_f}{2} \tag{B.11}$$

$$G_{IIc} = \int_0^{u_f} \sigma_{II}\ du = \frac{S_{II} u_f}{2} = \frac{k_{II}\bar{\delta}_0 \sin^2(\beta)\cos^2(\alpha)\bar{\delta}_f}{2} \tag{B.12}$$

$$G_{IIIc} = \int_0^{v_f} \sigma_{III}\ dv = \frac{S_{III} v_f}{2} = \frac{k_{III}\bar{\delta}_0 \sin^2(\beta)\sin^2(\alpha)\bar{\delta}_f}{2} \tag{B.13}$$

Similarly the equivalent fracture toughness is given by [Oliveira 2018]:

$$\bar{G}_c = \int_0^{\bar{\delta}_f} \bar{\sigma}\ d\bar{\delta} = \frac{\bar{S}\bar{\delta}_f}{2} = \frac{\bar{k}\bar{\delta}_0\bar{\delta}_f}{2} \tag{B.14}$$

Where the equivalent strength and stiffness are:

$$\begin{aligned} \bar{S} &= k_S \cos^2(\beta) + S_{II}\sin^2(\beta)\cos^2(\alpha) + S_{III}\sin^2(\beta)\sin^2(\alpha) \\ \bar{k} &= k_I \cos^2(\beta) + k_{II}\sin^2(\beta)\cos^2(\alpha) + k_{III}\sin^2(\beta)\sin^2(\alpha) \end{aligned} \tag{B.15}$$

Incorporating equation B.14 in the definition of the B-K criterion (equation B.9) and isolating the equivalent displacement at failure results in [Oliveira 2018]:

$$\bar{\delta}_f = \frac{2\left[G_{Ic} + (G_{IIc} - (G_{Ic})\phi^{\eta}\right]}{\bar{k}\bar{\delta}_0} \tag{B.16}$$

$*$ = Exemplatory case of a mixed mode ratio
$_s$ = Shearing mode (II or III)

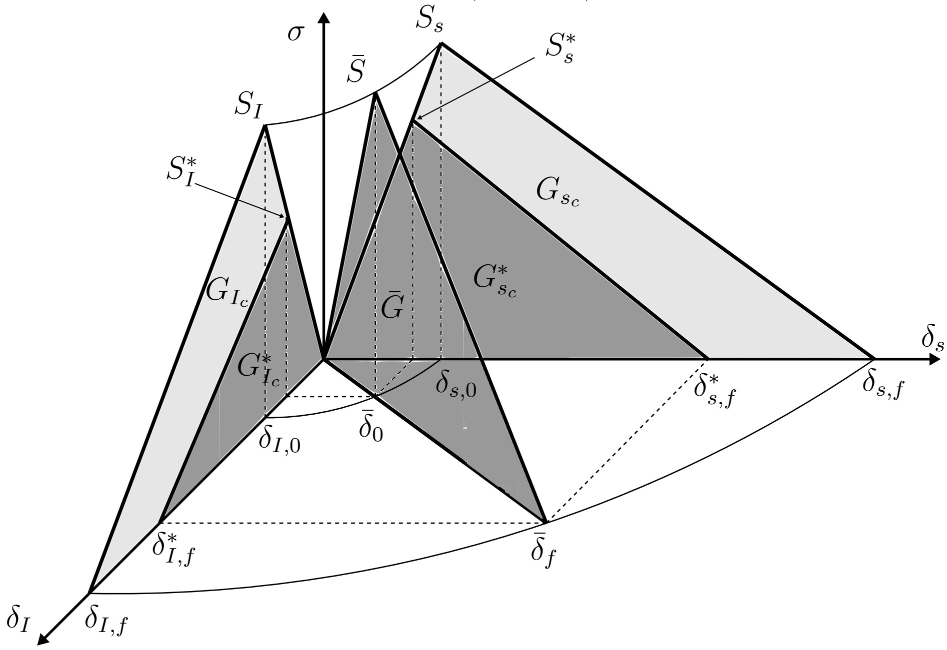

FIGURE B.2 – Mixed mode bilinear traction–separation law

Static damage evolution

To calculate the static damage parameter, it makes sense to first elaborate on the relationship between the equivalent displacement and the static damage. For the case of no fatigue damage this is given by [Oliveira 2018]:

$$\bar{\delta} = \bar{\delta}_0 + D^s(\bar{\delta}_f - \bar{\delta}_0) \tag{B.17}$$

If the equivalent displacement is larger than the displacement at damage onset, but smaller than the displacement at failure, the static damage parameter is then given by:

$$D^s = \frac{\bar{\delta}_f}{\bar{\delta}} \left(\frac{\bar{\delta} - \bar{\delta}_0}{\bar{\delta}_f - \bar{\delta}_0} \right) \qquad \text{if} \qquad \bar{\delta}_0 < \bar{\delta} < \bar{\delta}_f \tag{B.18}$$

B.3.2 Fatigue damage

The fatigue damage in the VUMAT is based on the Paris law. As was described in section A.2, many versions of the Paris law exist. The one used by Oliveira (2018) uses the strain energy release rate ratio in combination with the fracture toughness of the material:

$$\frac{da}{dN} = C \left(\frac{\triangle G}{G_c} \right)^n \tag{B.19}$$

Where C and n are experimentally determined fitting parameters using tests on coupon level. The cyclic variation of the SERR ($\triangle G$) is given by:

$$\triangle G = G_{max} - G_{min} \tag{B.20}$$

Which can be rewritten to:

$$\triangle G = G_{max}(1 - R^2) \tag{B.21}$$

Given that:

$$R^2 = \left(\frac{P_{min}}{P_{max}} \right)^2 = \frac{G_{min}}{G_{max}} \tag{B.22}$$

Equation B.19 is for a single mode situation. As the loading in real life applications is generally mixed mode, $\triangle G$ and G_c have to be written in terms of their equivalent counterparts $\triangle \bar{G}$ and $\bar{G}_c$. Using the B-K interpolation criterion for G_c (equation B.9) and equation B.21 to rewrite $\triangle G$, Paris' law for mixed mode applications can be written as:

$$\frac{da}{dN} = \bar{C} \left(\frac{\bar{G}_{max}(1 - R^2)}{G_{Ic} + (G_{IIc} - G_{Ic})\phi^{\eta}} \right)^{\bar{n}} \tag{B.23}$$

Where one has to be careful of the fact that the fitting parameters $\bar{C}$ and $\bar{n}$ are dependent on the mixed mode ratio and thus not equal to the fitting parameters given in equation B.19. Blanco et al. (2004) suggested the following two equations to interpolate these fitting parameters based on coupon testing:

$$\log(\bar{C}) = \log(C_I) + \log(C_b)\phi + \log\left(\frac{C_{II}}{C_I C_b} \right) \phi^2 \tag{B.24}$$

$$\bar{n} = n_I + n_b\phi + (n_{II} - n_I - n_b)\phi^2 \tag{B.25}$$

Where n_b and C_b are parameters that have to be fitted based on mixed mode coupon level experiments. In these equations mode III was left out of the scope as mode III is assumed equal to mode II in this thesis.

Finally, an addition was made to equation B.23 by including a threshold value. As explained in section A.2, a threshold value determines below which value of G no fatigue growth occurs. This was implemented as:

$$\frac{da}{dN} = \begin{cases} \bar{C}\left(\frac{\bar{G}_{max}(1-R^2)}{G_{Ic}+(G_{IIc}-G_{Ic})\phi^\eta}\right)^{\bar{n}} & \text{if} \quad \bar{G}_{th} < \bar{G}_{max} \\ 0 & \text{if} \quad \text{Otherwise} \end{cases} \tag{B.26}$$

Where an equation equal to B.9 was used to interpolate the equivalent threshold values from the single mode ones obtained from coupon tests.

Fatigue damage evolution

During the fatigue phase only the elements at the crack tip are degraded. The crack tip consists of all elements neighbouring one fully failed element. Thus, at least one fully failed element is required as input for the fatigue degradation to start. The amount of damage in an element obtained per fatigue cycle ($\frac{dD_f}{dN}$) can be rewritten using Paris' law:

$$\frac{dD^f}{dN} = \frac{dD^f}{da}\frac{da}{dN} \tag{B.27}$$

However, one more thing has to be taken into account: static damage during the fatigue loading. As a consequence of an element obtaining fatigue damage, it loses stiffness. When an element loses stiffness its upper and lower surface move. This movement gets interpreted by the static part of the model, explained in subsection B.3.1, as relative displacement and it will thus induce additional damage. However, the way Paris' law is fitted, it already incorporates all damage that occurs during the fatigue loading. Therefore this static damage occurring during the fatigue loading has to be omitted:

$$\triangle D^f = \int_n^{n+\triangle n} \frac{dD^f}{da}\frac{da}{dN} dN - \triangle D^s \tag{B.28}$$

The remaining term $\frac{dD_f}{da}$ can be found by expressing the damage as a function of the crack length inside the element and the element length l_e:

$$D = \frac{a}{l_e} \tag{B.29}$$

Resulting in:

$$\frac{dD^f}{da} = \frac{1 - D^s}{l_e} \tag{B.30}$$

Now the fatigue damage accumulated per cycle can be rewritten to:

$$\frac{dD^f}{dN} = \frac{1 - D^s}{l_e}\frac{da}{dN} \tag{B.31}$$

Where $\frac{da}{dN}$ is given by equation B.26.

Numerical application of the cyclic loading

From a computational point of view it is nearly impossible to simulate all load cycles of a high cycle fatigue simulation separately. Peerlings et al. (2000) proposed an approach based on load and displacement envelopes to mitigate this problem. Robinson et al. (2005) were the first to report about successfully applying this approach in the context of cohesive zone modelling.

In this approach a constant static load, equal to P_{max}, is used throughout the fatigue simulation, as is illustrated in figure B.3. The cycles are then applied through a numerical frequency. For each cycle $\bar{G}_{max}$ is calculated based on the relevant SERR of mode I, II and III. As R is known a priori, the fatigue damage rate can then be calculated through a numerical time integration scheme. The pseudo-time of the simulation is not related to any physical time, making properties such as kinetic energy or strain rate irrelevant.

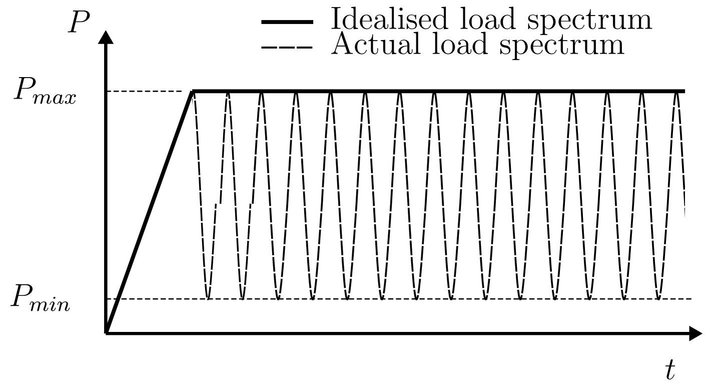

FIGURE B.3 – Idealised numerical load as used in the VUMAT

Appendix C - Experimental set-up

The aim of this chapter is to give a more thorough explanation of several aspects of the experimental phase of the research. As such, section C.1 explains the pre-cracking procedure. Section C.2 gives a clear overview of how the boundary conditions are fulfilled and what the locations of the strain gauges are during the quasi-static compression experiments. Finally section C.3 explains the procedure behind the measurement of the disbond length and area using the c-scan.

C.1 Pre-cracking

The goal of the pre-cracking procedure was to make sure that the Teflon area was fully disbonded. Additionally, the pre-cracking aided in creating a more naturally shaped sharp crack, as the original crack front was likely more blunt. The pre-cracking procedure was done using a 7 point bending test, as designed by [Van Rijn e Wiggenraad 2000]. They state that in composite bonded panels this test generates failure at the skin-stiffener interface before anywhere else. An Instron 5500R was used to load the panel using displacement control, while the load displacement curves were monitored constantly. Per side one operator observed the crack size throughout the experiment and stopped the experiment right before the observable crack size reached 100 mm. An overview of the 7 point bending rig can be seen in figure C.1.

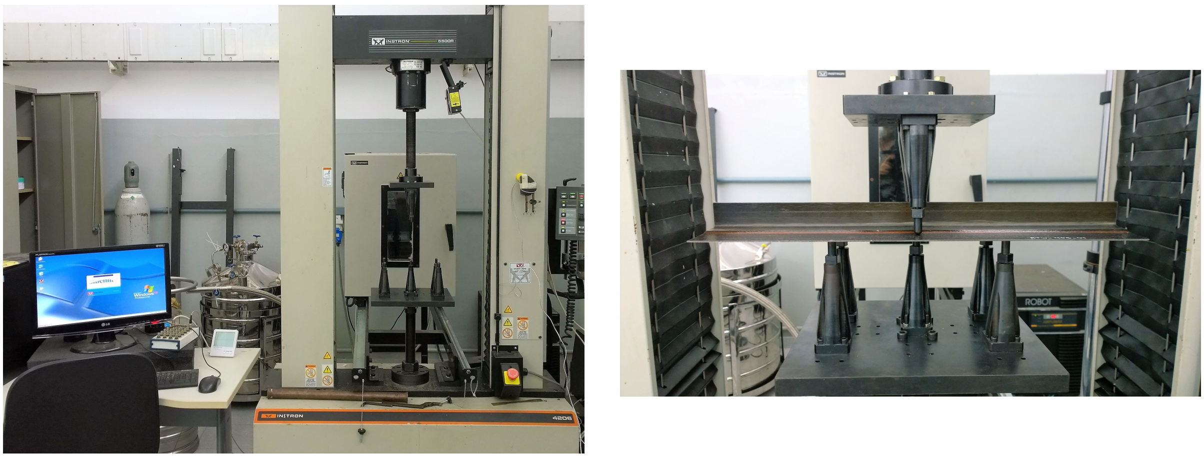

(a) General overview (b) Close-up

FIGURE C.1 – 7 point bending test

All RTW panels were pre-cracked after the hygrothermal aging, right before they were tested. This procedure was followed to be able to study the influence of hygrothermal aging on the crack propagation, rather than the crack initiation. It was explained in subsection 2.2.3 that these are not expected to be the same after hygrothermal aging.

C.2 Quasi-static testing

In this section the experimental set-up as used during the quasi-static compression tests is shown more thoroughly through the use of several pictures. Figure C.2 shows the clamping device that is used to clamp the ends of the panels. Figure C.3 shows the blades providing the anti-buckling support. The testing rig in which the panel is placed is displayed in figure C.4. Finally, the locations of the strain gauges that are used during the quasi-static tests are given in figures C.5 and C.6.

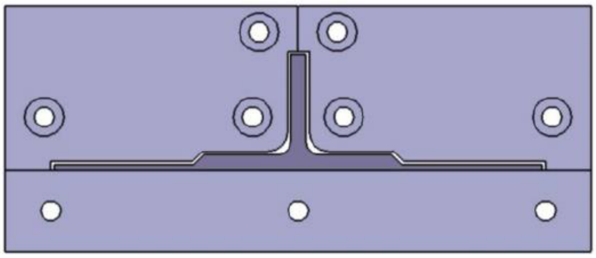

FIGURE C.2 – Clamping device at panels ends

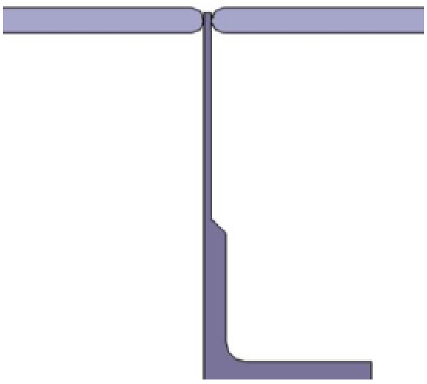

FIGURE C.3 – Anti buckling support at the edges of the panels

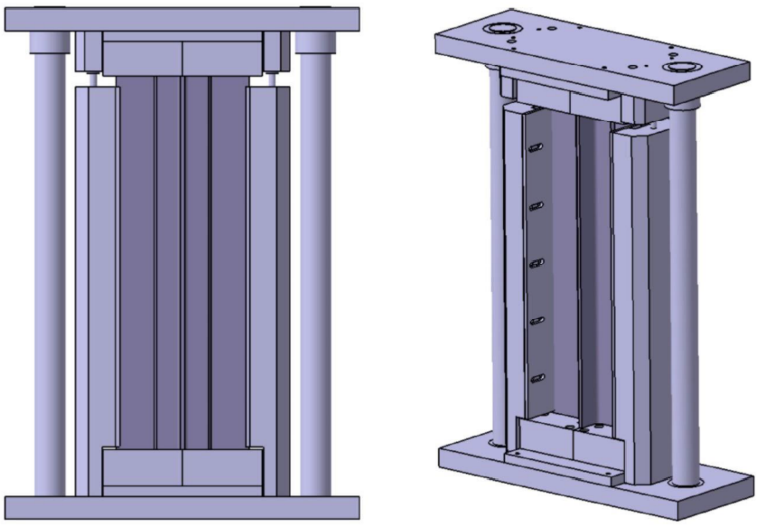

FIGURE C.4 – Schematic drawing of the testing rig

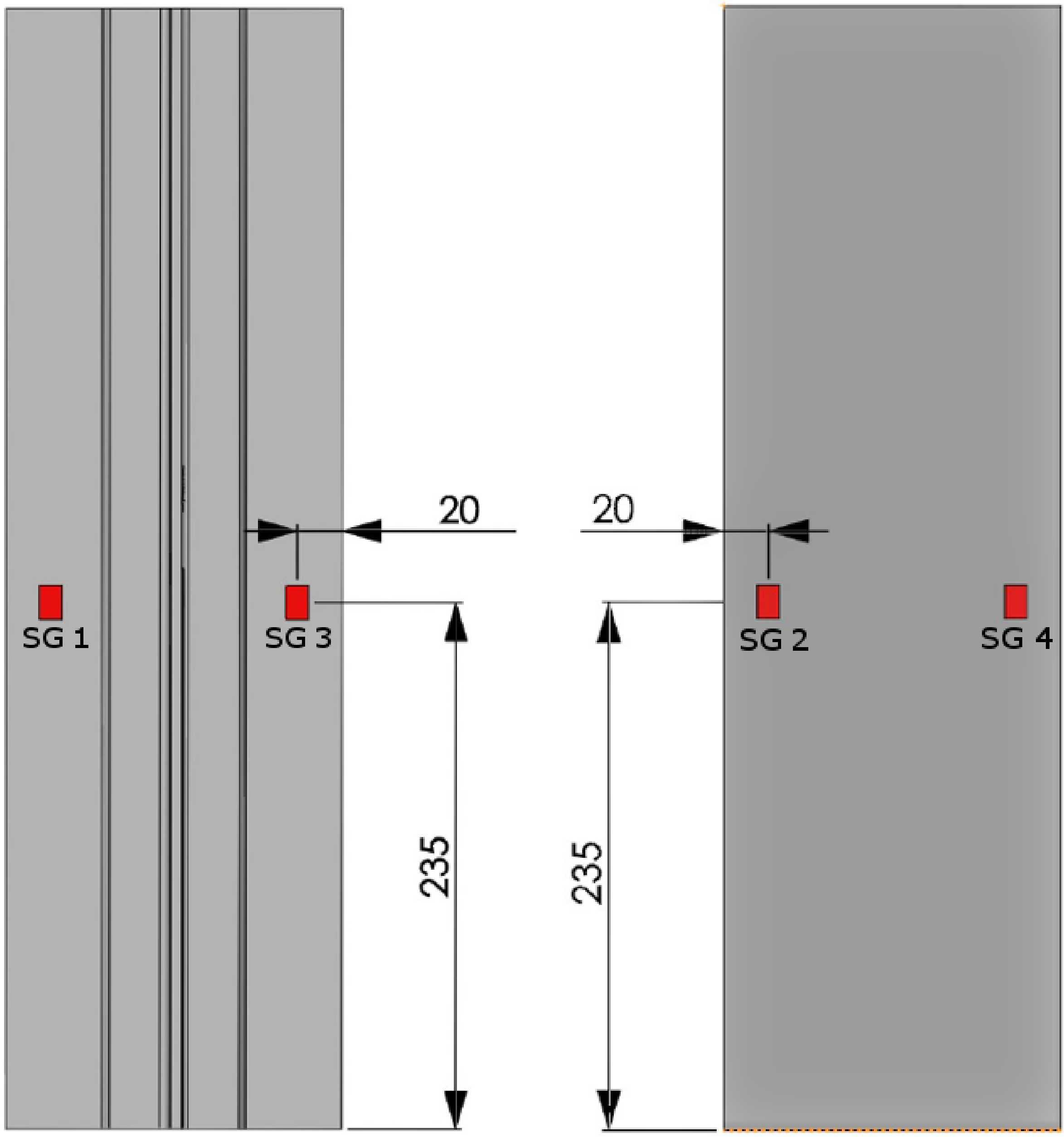

(a) Top view (b) Bottom view

FIGURE C.5 – Locations of the strain gages from the top and bottom view

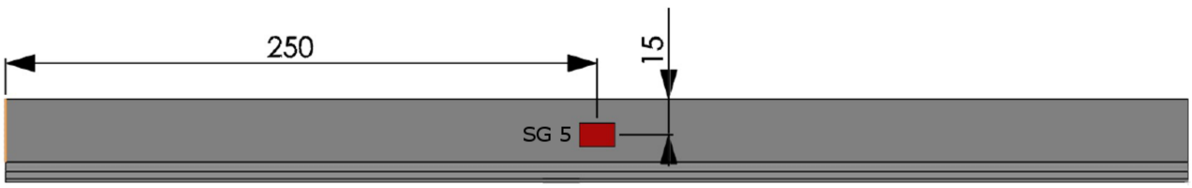

FIGURE C.6 – Location of the strain gages from the side view

C.3 Disbond length and area procedure

The disbond length was measured by taking the difference between the two outer edges of the disbond, assuming a smoothly changing crack front. This approach mitigated the effects of the shifting probe location a bit, as the shifting resulted in a jagged crack front. An example of a length measurement can be seen in figure C.7.

The area was measured using a Matlab tool developed by Hottentot Cederløff (2018). This tool first converts the presented image to a binary image in which all disbonded area is 1 and all non-disbonded area a 0. Subsequently a maximum distance of 64 mm is applied to take out the disbond outside the stiffener. Then the outer edges of the disbonded area are registered and everything in between these edges is assumed to be fully disbonded. Finally, the total disbonded area is measured. These steps are all displayed in figure C.8.

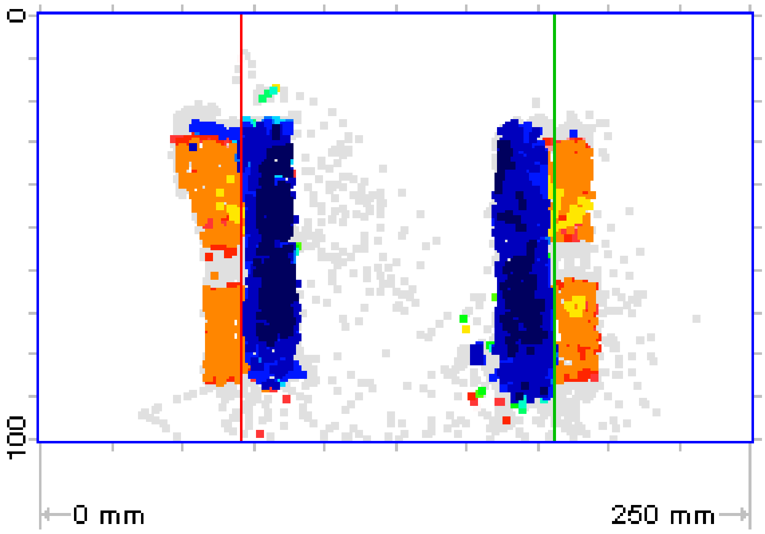

FIGURE C.7 – Length post-processing of the c-scan of 405-03 RTA after 100,000 cycles. Blue indicates disbonded area, red/orange/yeallow indicates an intact cohesion.

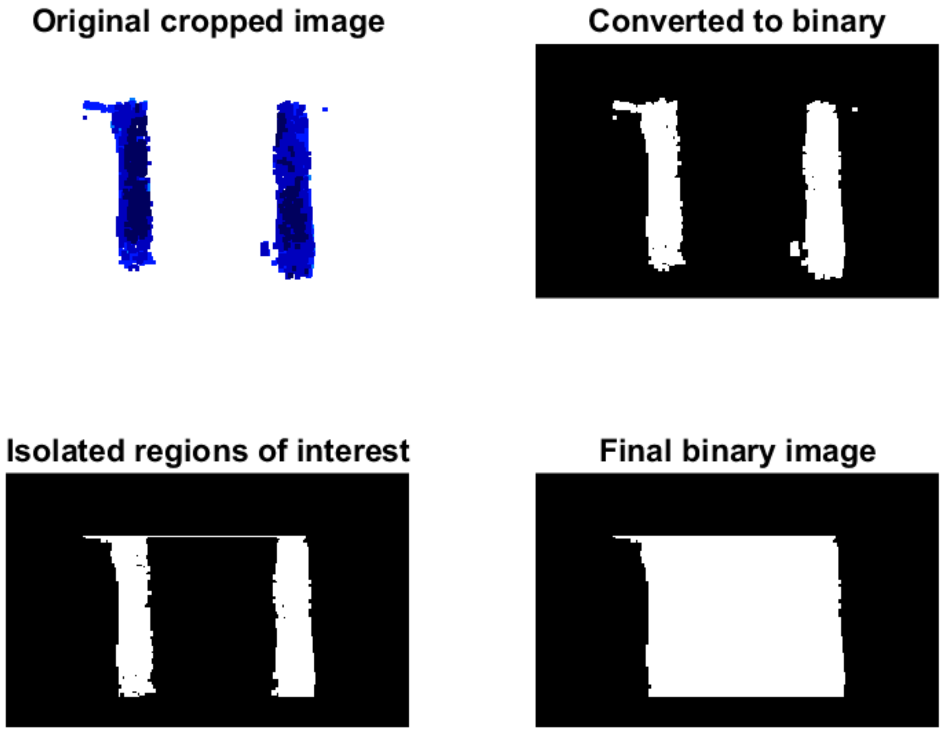

FIGURE C.8 – Area post-processing of the c-scan of 405-03 RTA after 100.000 cycles

Appendix D - Hashin's damage model

Hashin's damage model in Abaqus is based on Hashin's damage as reported by Hashin and Rotem (1973) and Hashin (1980). It uses three damage parameters to gradually decrease the stiffness of the elements until final failure occurs [ABAQUS Inc. 2014]. The model requires three input parameters:

- A linear elastic undamaged response of the material.
- A damage initiation criterion.
- A damage evolution law, including element removal.

D.1 Constitutive law

The constitutive law uses a separate damage variable for the fiber damage (D_{fi}) and the matrix damage (D_m).

$$\begin{Bmatrix} \sigma_{11} \\ \sigma_{22} \\ \tau_{12} \end{Bmatrix} = \frac{1}{Q} \begin{bmatrix} (1-D_{fi})E_1 & (1-D_{fi})(1-D_m)\nu_{21}E_1 & 0 \\ (1-D_{fi})(1-D_m)\nu_{12}E_2 & (1-D_m)E_2 & 0 \\ 0 & 0 & (1-D_s)\mu Q \end{bmatrix} \begin{Bmatrix} \epsilon_{11} \\ \epsilon_{22} \\ \epsilon_{12} \end{Bmatrix}$$
$$\Rightarrow Q = 1-(1-D_{fi})(1-D_m)\nu_{12}\nu_{21} \tag{D.1}$$

Where separate damage modes exist for compression D^C and tensile D^T stress states of both the fiber and matrix damage. Therefore, the damage variables can be further split into:

$$\begin{aligned} D_{fi} &= \begin{cases} D_{fi}^T & \text{if } \hat{\sigma}_{11} \geq 0 \\ D_{fi}^C & \text{if } \hat{\sigma}_{11} < 0 \end{cases} \\ D_m &= \begin{cases} D_m^T & \text{if } \hat{\sigma}_{22} \geq 0 \\ D_m^C & \text{if } \hat{\sigma}_{22} < 0 \end{cases} \\ D_s &= 1-(1-D_{fi}^T)(1-D_{fi}^C)(1-D_m^T)(1-D_m^C) \end{aligned} \tag{D.2}$$

Where $\hat{\sigma}_{11}$ and $\hat{\sigma}_{22}$ are components of the effective stress tensor. Which is given by:

$$\begin{Bmatrix} \hat{\sigma}_{11} \\ \hat{\sigma}_{22} \\ \hat{\tau}_{12} \end{Bmatrix} = \begin{bmatrix} \frac{1}{1-D_{fi}} & 0 & 0 \\ 0 & \frac{1}{1-D_m} & 0 \\ 0 & 0 & \frac{1}{1-D_s} \end{bmatrix} \begin{Bmatrix} \sigma_{11} \\ \sigma_{22} \\ \tau_{12} \end{Bmatrix} \tag{D.3}$$

D.2 Damage initiation

Damage initiation of the model is based on Hashin's theory [Hashin e Rotem 1973, Hashin 1980]. Damage initiates once the equivalent displacement ($\bar{s}$) of one of the damage modes is larger than the equivalent displacement at damage onset ($\bar{s}_0$) of that mode ($\bar{s} \geq \bar{s}_0$). The criteria are implemented in Abaqus as follows [ABAQUS Inc. 2014]:

$$\begin{array}{lll}
\text{Fiber tension } (\hat{\sigma}_{11} \geq 0) & \Rightarrow & \left(\dfrac{\hat{\sigma}_{11}}{S_1^T}\right)^2 + \alpha\left(\dfrac{\hat{\tau}_{12}}{S_{12}}\right)^2 = 1 \\
\text{Fiber compression } (\hat{\sigma}_{11} < 0) & \Rightarrow & \left(\dfrac{\hat{\sigma}_{11}}{S_1^C}\right)^2 = 1 \\
\text{Matrix tension } (\hat{\sigma}_{22} \geq 0) & \Rightarrow & \left(\dfrac{\hat{\sigma}_{22}}{S_2^T}\right)^2 + \left(\dfrac{\hat{\tau}_{12}}{S_{12}}\right)^2 = 1 \\
\text{Matrix compression } (\hat{\sigma}_{22} < 0) & \Rightarrow & \left(\dfrac{\hat{\sigma}_{22}}{2S_{13}}\right)^2 + \left[\left(\dfrac{S_2^C}{2S_{13}}\right)^2 - 1\right]\dfrac{\hat{\sigma}_{22}}{S_2^C} + \left(\dfrac{\hat{\tau}_{12}}{S_{12}}\right)^2 = 1
\end{array} \tag{D.4}$$

Where α is the contribution of the shear stress to the fiber tensile initiation criterion

D.3 Damage evolution

A bilinear law, as depicted in figure D.1, is used to describe the damage evolution.

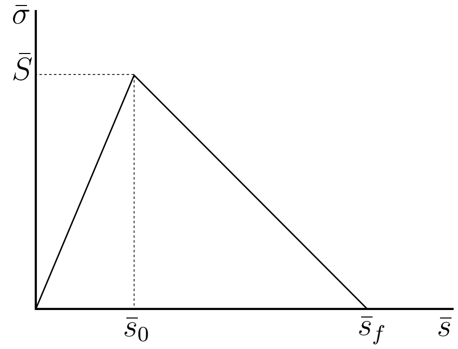

FIGURE D.1 – Bilinear damage evolution law Abaqus

Where $\bar{s}$ is the equivalent displacement. The equivalent displacement and equivalent stress for each failure mode are given by [ABAQUS Inc. 2014]:

$$
\begin{aligned}
\bar{s}_{fi} &= \begin{cases} L_{char}\sqrt{\langle \epsilon_{11} \rangle^2 + \alpha \epsilon_{12}^2} & \text{if } \hat{\sigma}_{11} \geq 0 \\ L_{char}\langle -\epsilon_{11} \rangle & \text{if } \hat{\sigma}_{11} < 0 \end{cases} \\
\bar{s}_{m} &= \begin{cases} L_{char}\sqrt{\langle \epsilon_{22} \rangle^2 + \epsilon_{12}^2} & \text{if } \hat{\sigma}_{22} \geq 0 \\ L_{char}\sqrt{\langle -\epsilon_{22} \rangle^2 + \epsilon_{12}^2} & \text{if } \hat{\sigma}_{22} < 0 \end{cases} \\
\bar{\sigma}_{fi} &= \begin{cases} \dfrac{\langle \sigma_{11} \rangle \langle \epsilon_{11} \rangle + \alpha \tau_{12}\epsilon_{12}}{\bar{s}_{fi}/L_{char}} & \text{if } \hat{\sigma}_{11} \geq 0 \\ \dfrac{\langle -\sigma_{11} \rangle \langle -\epsilon_{11} \rangle}{\bar{s}_{fi}/L_{char}} & \text{if } \hat{\sigma}_{11} < 0 \end{cases} \\
\bar{\sigma}_{m} &= \begin{cases} \dfrac{\langle \sigma_{22} \rangle \langle \epsilon_{22} \rangle + \tau_{12}\epsilon_{12}}{\bar{s}_{m}/L_{char}} & \text{if } \hat{\sigma}_{22} \geq 0 \\ \dfrac{\langle \sigma_{-22} \rangle \langle \epsilon_{-22} \rangle + \tau_{12}\epsilon_{12}}{\bar{s}_{m}/L_{char}} & \text{if } \hat{\sigma}_{22} < 0 \end{cases}
\end{aligned}
\tag{D.5}
$$

Where the characteristic length L_{char} of shell elements is equal to the square root of the element's total area. The damage variable in the bilinear evolution law is given by:

$$
D = \frac{\bar{s}_f(\bar{s} - \bar{s}_0)}{\bar{s}(\bar{s}_f - \bar{s}_0)} \qquad \text{if } \bar{s} \geq \bar{s}_0 \tag{D.6}
$$

Once an element is fully deteriorated the element is deleted and will no longer offer resistance to deformation. For Abaqus/Explicit this occurs when either the compression or tensile fiber failure mode is 1 [ABAQUS Inc. 2014].

Appendix E - Abaqus verification models

To verify the VUMAT model of Oliveira (2018) in combination with the material combination used in this work numerical simulations of DCB, 4-ENF and 50% MMB tests were carried out. These experiments had previously been carried out by Brito (2017). In the sections below the numerical models will be explained and compared to the experimental results.

E.1 Double cantilever beam

The quasi-static double cantilever beam experiments performed by Brito (2017) followed ASTM D5528-13 (2013). For more background information on this procedure the reader is referred to this standard. Two, 13 ply counting, co-bonded uni-directional laminates of the dimensions shown in figure E.1 were used to execute the experimental procedure.

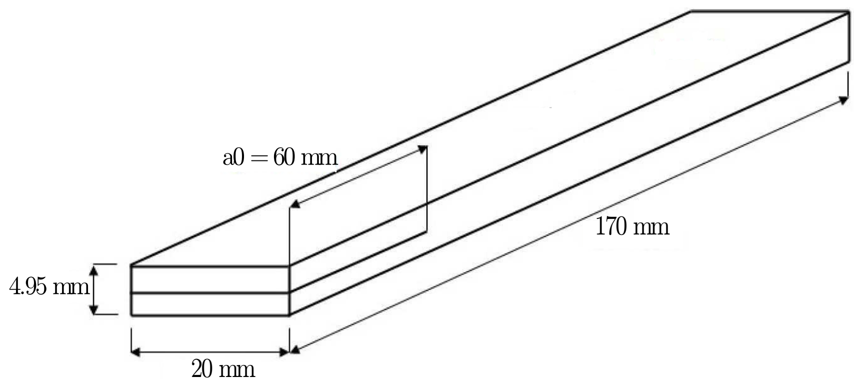

FIGURE E.1 – Dimensions of the DCB specimens as used by Brito (2017)

The material properties used in the numerical simulation were largely the same as those mentioned in section 3.1.1. One difference being the strength of the adhesives. Simulations quickly showed that these were too low and resulted in a very low damage onset. To counter this the interface strength of a co-cured T800/3900-2B was used with the properties as displayed in table E.1.

TABLE E.1 – Strength properties of the adhesive

S_1 [MPa]	S_2 [MPa]	S_3 [MPa]
50	180	180

The laminates were modeled using four node shell elements with reduced integration (S4R). The adhesive was represented by solid eight node elements with reduced integration (C3D8R) of 0.0192 mm thickness. Which is equal to 10% of the ply-thickness. This thickness was originally chosen by Oliveira (2018) for co-cured laminates, as it roughly represents the thickness of the co-cured area [Hojo *et al.* 2006]. Since the precise thickness of the adhesive in these co-bonded specimens is unknown the same thickness was chosen here. Tie constrains were used to connect the upper surface of the cohesive to the top laminate and the lower surface of the cohesive to the bottom laminate, as depicted in figure E.2. The Abaqus user manual [ABAQUS Inc. 2014] suggests to use the stiffest surface as master in the tie-constraint and the more compliant one as a slave. Therefore both surfaces of the cohesive act as a slave to the stiffer laminate.

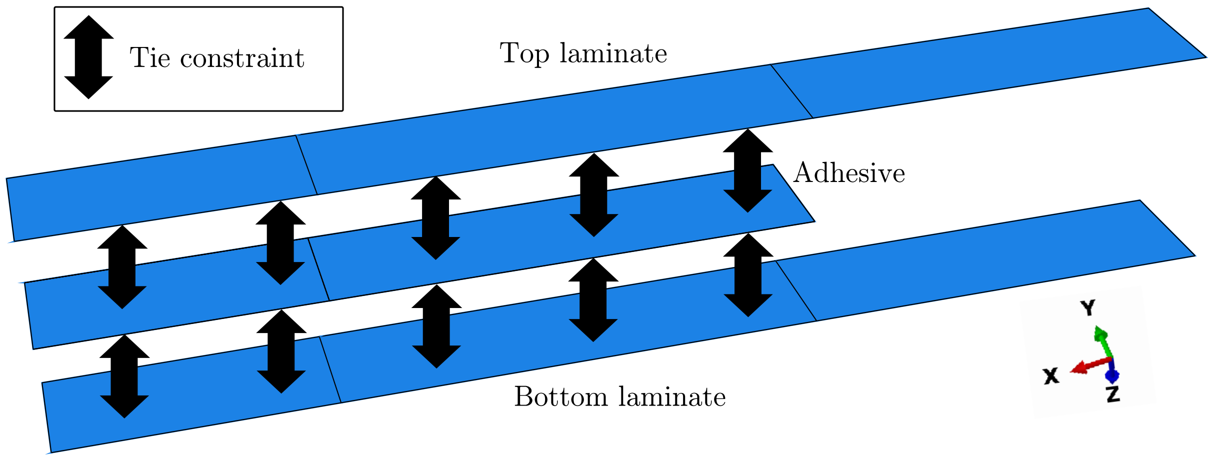

FIGURE E.2 – Tie restrictions imposed on the DCB model

In the experiments the displacement of the ends was applied using loading blocks. This was represented in the simulation by applying a displacement of 10 mm upwards on the edge of the top laminate and 10 mm downwards on the edge of the bottom laminate in 1 second. These edges can be seen in figure E.3. Additionally, these edges were constrained in the X-direction and four corners were constrained in the y-direction to limit rigid body motions.

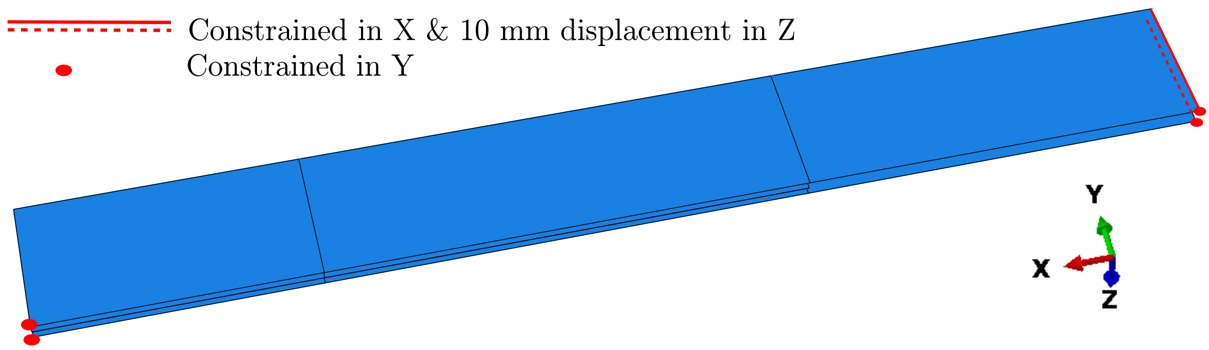

FIGURE E.3 – Boundary conditions imposed on the DCB model

After a mesh-convergence study an element size of 0.1 mm at the interface was chosen. Near the edge where the load was applied bigger elements were used because here no crack growth occurs and stress representations don't have to be ass precise. Similarly, at the other end of the specimen a larger mesh size could be used as the crack is not required to grow all the way to the end. Thus, to speed up the simulation, a single bias mesh seed was used at these locations to gradually increase the mesh size. Resulting in the mesh displayed in figure E.4.

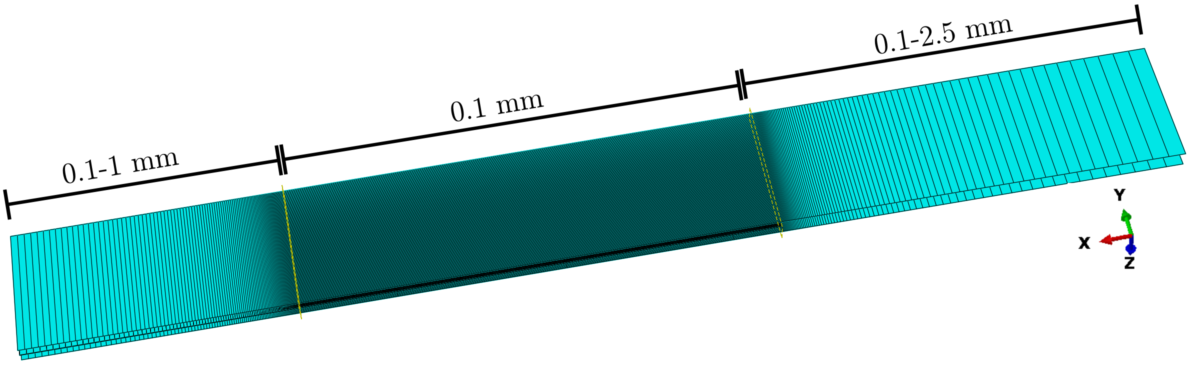

FIGURE E.4 – Mesh of the DCB model

The simulation was performed using the dynamic explicit time-step with geometrical non-linearities activated. To speed up the simulation mass scaling was used on the entire assembly. This option changes the density of elements with high wave speeds to increase their stable time increment [ABAQUS Inc. 2014]. A target stable time increment of 1E-06 seconds resulted in high computational speed while keeping the kinetic energy low compared to the total energy (less than 10%).

Figure E.5 shows the final experimental, theoretical and numerical results. The theoretical results are based on the work of Donadon and Faria (2016). As the graph shows the numerical model is not capable of simulating the stick-slip behavior occurring in the experimental procedure. This is because the stick-slip behavior is caused by local material properties, whereas the model assumes homogeneous material. Therefore, one should compare the numerical result with the theoretical result. Which show great resemblance. The instability at the end of the simulation is caused by the increased mesh size used at this point. The total amount of damage accumulated over the simulation is shown in figure E.6

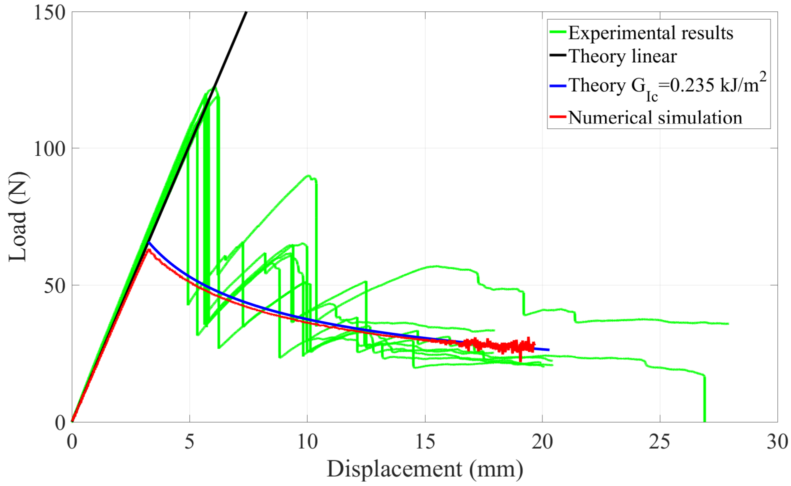

FIGURE E.5 – Experimental and numerical load displacement curves DCB test

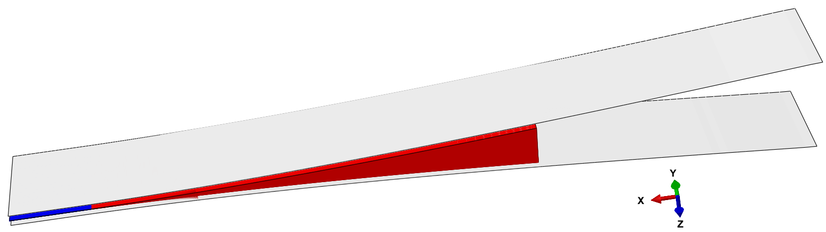

FIGURE E.6 – Total amount of damage in the cohesive (red) at the end of simulation

E.2 4 End notch flexure

The 4-ENF test performed by Brito (2017) was according to the design proposed by Martin and Davidson (1999). A schematic overview of the set-up can be seen in figure E.7 and the dimensions of the uni-directional specimens can be seen in figure E.8. Experimentally, the load was applied using two connected rollers, this was modeled with a rigid body connected with equations to the opposite corners, as displayed in figure E.9. Furthermore, similar tie constraints were used as in the DCB simulation.

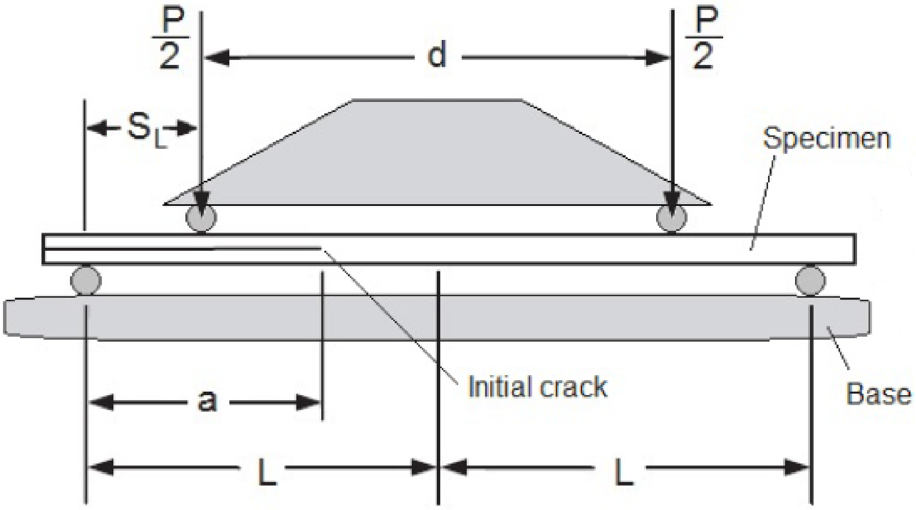

FIGURE E.7 – Schematic drawing of the ENF test set-up [Brito 2017]

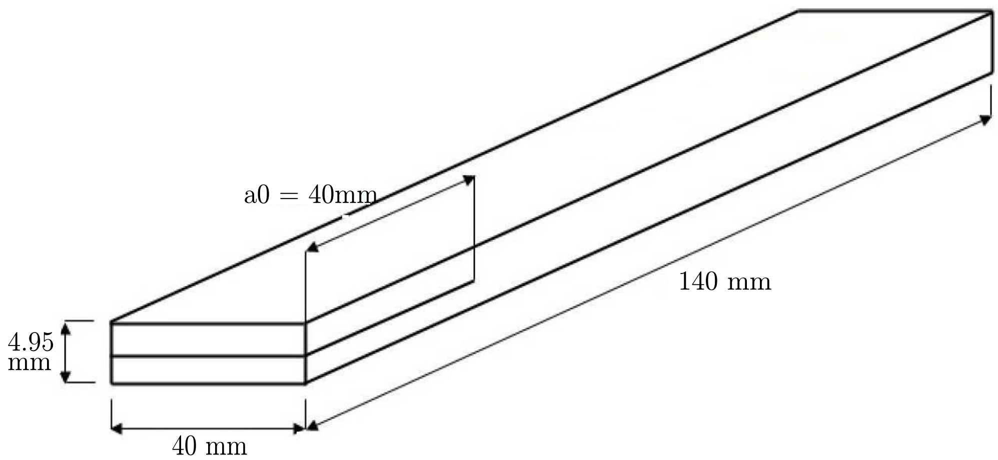

FIGURE E.8 – Dimensions of the ENF specimens as tested by Brito (2017)

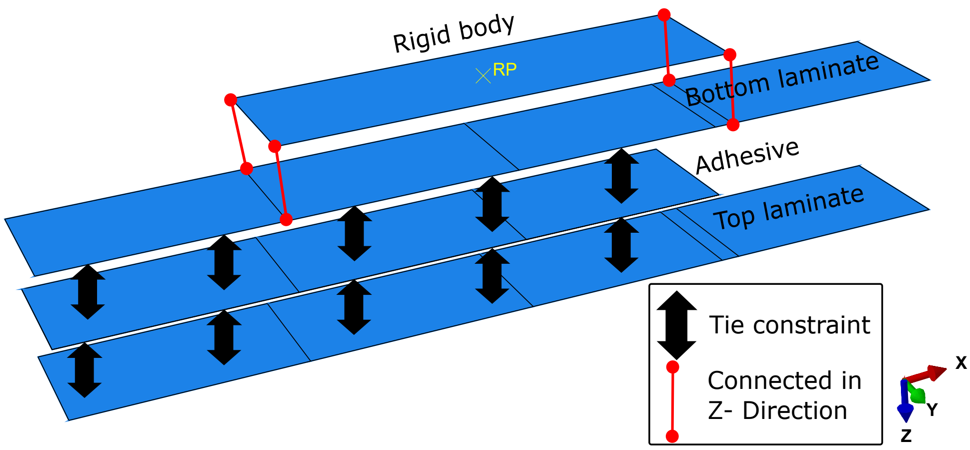

FIGURE E.9 – Constraints imposed on the ENF model

A problem arising during the simulation of the 4-ENF test was the stability of the cohesive elements. Similar as with the DCB simulation, reduced integration 8-node brick elements were used. These elements tend to suffer from hourglassing, which can be countered using hourglass control in the elements. However, enabling this feature imposes additional stiffness on the elements and therefore changed the damage propagation. To circumvent this problem additional boundary conditions were applied on the laminates to prevent unwanted motions.. These boundary conditions restricted all laminate edges from moving in y-direction and rotating around the x- and z-axes. These edges are highlighted in figure E.10. Additionally, the reference point of the rigid body was only allowed to rotate around the y-axis. Finally, the outer edges of the top laminate were used to apply a 4 mm displacement each. The force this caused on the reference point was then used to extract the total exerted load.

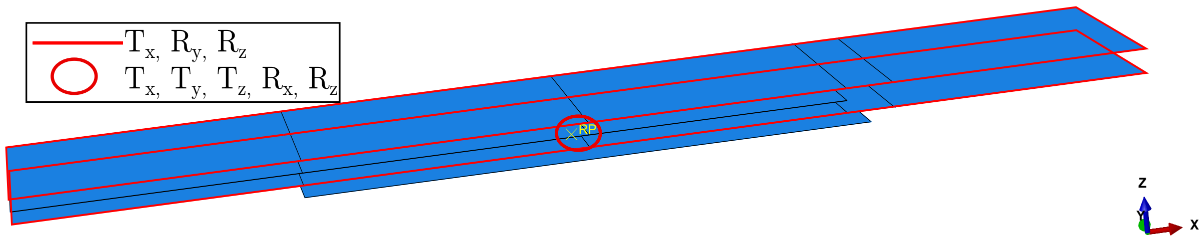

FIGURE E.10 – Boundary conditions imposed on the ENF model

To check the validity of the VUMAT the most important parameters to check are the damage initiation point and the damage propagation during the period where the damage is in between the top rollers of figure E.7. To capture this correctly a relative coarse mesh can be used at either ends of the laminate, whereas the part underneath the rigid body needs a fine mesh to capture the crack propagation correctly. This was captured using the mesh distribution depicted in figure E.11.

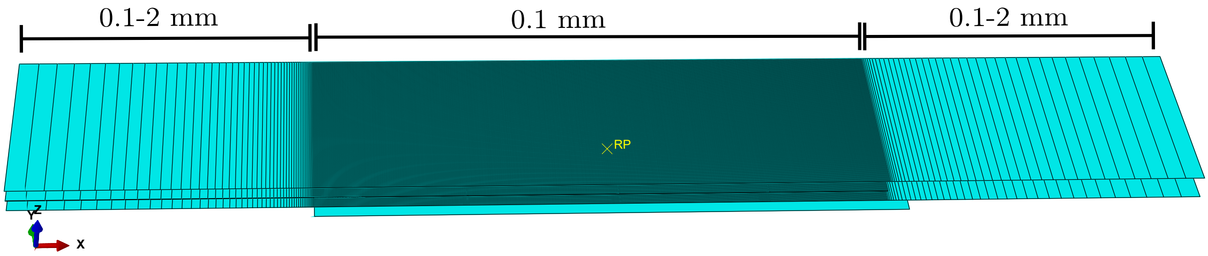

FIGURE E.11 – Mesh of the ENF model

The final results of the numerical simulation are shown in figure E.12. The stiffness of the specimens in the numerical simulation matches the theoretical stiffness, based on the work of Martin and Davidson (1999), well. The delamination starts when the load remains constant while the displacement increases. Until the delamination reaches the second roller the load should remain constant. Both the experimental and numerical results show this phenomenon.

The load at which damage onset takes place is roughly 15% lower in the numerical simulation than in the experimental results. This could potentially lead to an overestimation of the disboneded area during the quasi-static simulations. The difference could also be caused by the formulation of the boundary conditions. In the experiments the edges of the laminates were free to move, whereas in the numerical simulation they were restricted in several directions. Unfortunately this was required to have a stable simulation. This stability problem also meant that all failed elements had to deleted and a plot similar to figure E.6 could not be made.

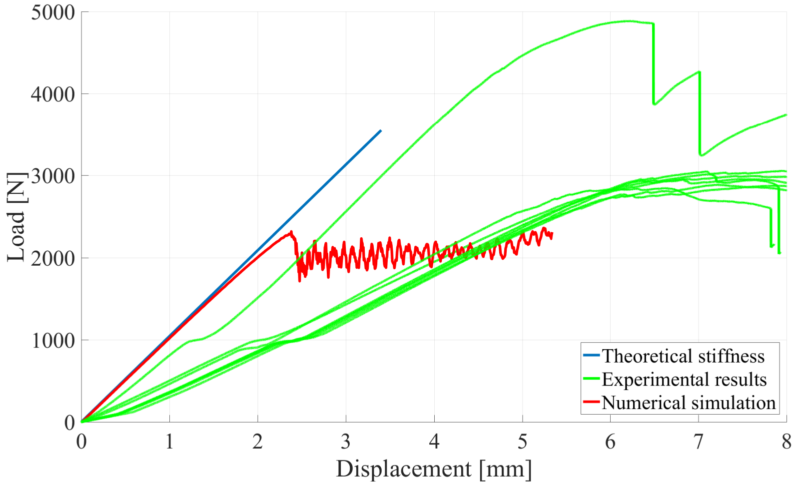

FIGURE E.12 – Experimental and numerical load displacement curves ENF test

E.3 Mixed mode bending

Brito (2017) performed 3 quasi-static mixed mode bending (MMB) tests to obtain the B-K parameter required for mixed mode interpolation. To validate this input and the mixed mode behavior of the VUMAT the simulation of the 50% mixed mode I and II situation was modelled. The experiments were performed according to ASTM D6671/D6671M-06 (2013). A schematic overview of the used set-up is given in figure E.13. Where L= 80 mm and c = 69.95 mm for a 50% MMB configuration. The dimensions of the specimens with uni-directional lay-up are given in figure E.14.

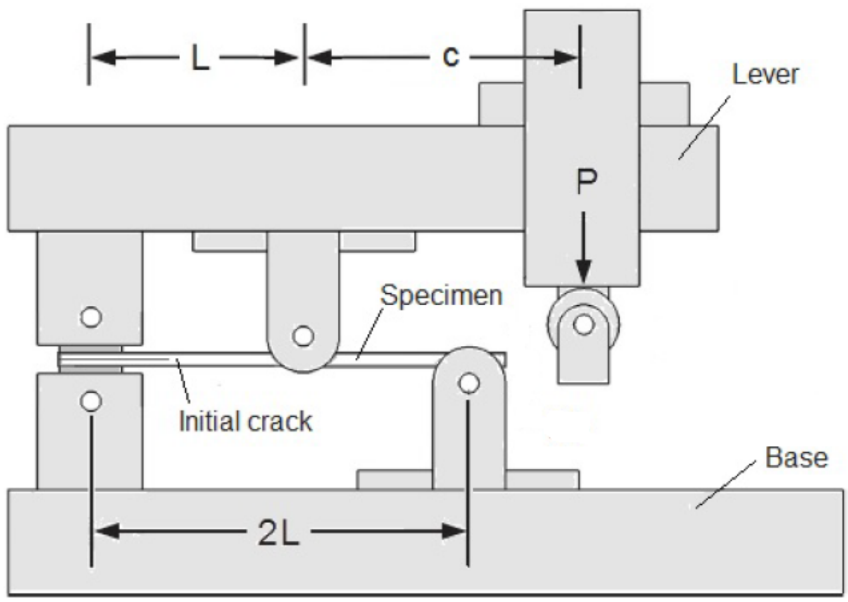

FIGURE E.13 – Schematic drawing of the MMB test set-up [Brito 2017]

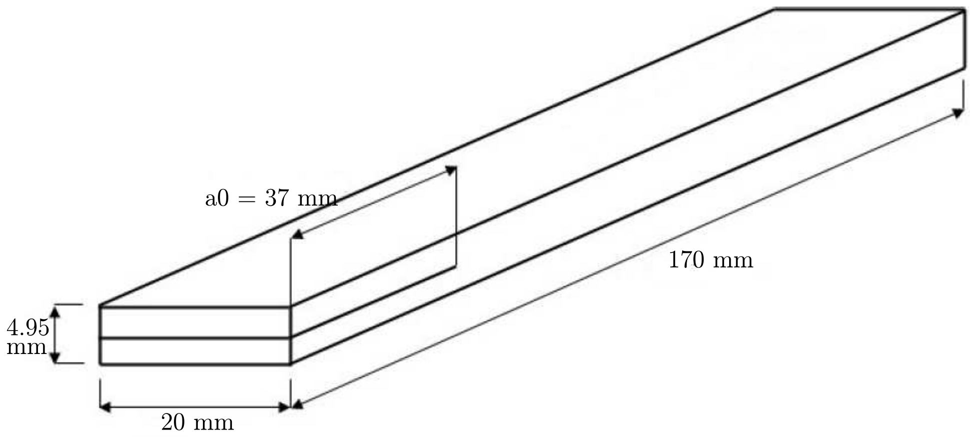

FIGURE E.14 – Dimensions of the MMB specimens as tested by Brito (2017)

To represent the loading configuration with a lever, a plate of the same length was used in the numerical simulation. For stability reasons this plate was modeled as a steel plate instead of a rigid plate, as was the case for the ENF simulation. This steel body was connected to the top laminate. In a similar way as the experimental set-up of figure E.13. Additionally, tie-constraints were used as was done for the ENF and DCB cases. Both types of constraints can be seen in figure E.15.

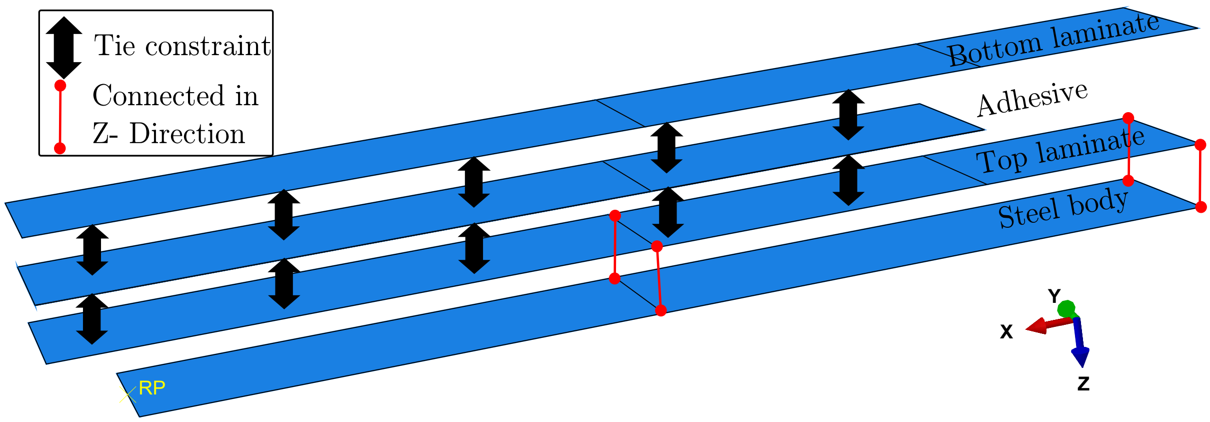

FIGURE E.15 – Constraints imposed on the MMB model

The boundary conditions imposed on the mixed mode bending model were similar as to those of the DCB. Translation in y-direction was prohibited along one side of the laminate to limit rigid body motions. Additionally, instead of applying a force on the lever it was chosen to apply a displacement in the positive z-direction on the edges of the bottom laminate. The force did get extracted from the location of the lever. To represent the lever's experimental boundary conditions it was only allowed to rotate around the y-axis. Additionally, it was required to apply several constraints on the rest of the stainless steel plate to improve the stability of the cohesive elements. For clarity all boundary conditions are displayed in figure E.16.

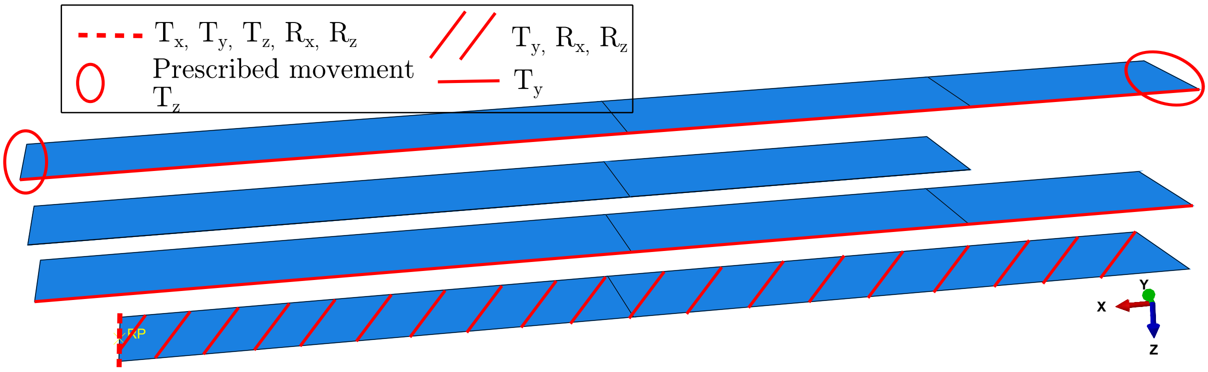

FIGURE E.16 – Boundary conditions imposed on the MMB model

A mesh size of 0.05 mm along the crack front was required to achieve mesh convergence. This small mesh size, in combination with the use of a flexible plate for the application of the load, significantly increased the total computation time of the simulation. The part of the model where the initial disbond was present contained a single bias mesh size from 0.1-2 mm.

The final results of the simulations are displayed in figures E.17 and E.18. The theoretical outcome is based on the work of Donadon and Faria [Donadon e Faria 2016]. As becomes clear from the load-displacement curves the onset point of damage is well simulated by the numerical simulation. Whereas the initial damage evolution is not captured perfectly. The experimental results show large discrepancies among each other, this potentially can influence the quality of the B-K parameter used in this report.

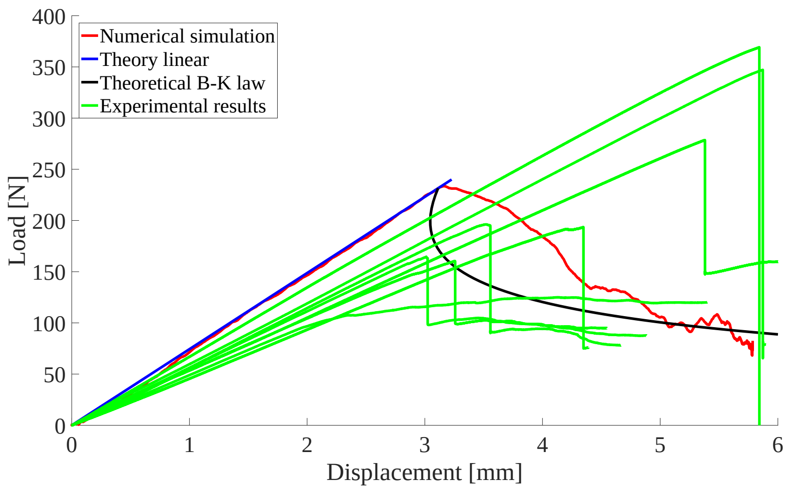

FIGURE E.17 – Experimental and numerical load displacement curves MMB test

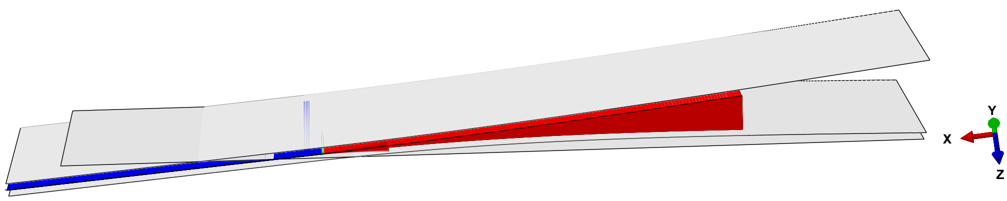

FIGURE E.18 – Total amount of damage in the cohesive (red) at the end of simulation